Hamburg University of Applied Sciences
Faculty of Life Sciences

Model Predictive Controller Tuning in Electrical Distribution Grids by Multiobjective Optimization

Master of Engineering Thesis

in

Renewable Energy Systems - Environmental and Process Engineering

submitted by

Jörg Michael Dietrich Richter
Matriculation Number: [redacted]

Hamburg, on

19. September 2018

1. Examiner:	Prof. Dr.-Ing. habil.	Gerwald Lichtenberg	HAW Hamburg
2. Examiner:	Dr.-Ing.	Georg Pangalos	Fraunhofer ISIT

Model Predictive Controller Tuning in Electrical Distribution Grids by Multiobjective Optimization

Master of Engineering Thesis

Jörg Michael Dietrich Richter

September 21, 2018

The work in this thesis was supported by Fraunhofer Institute for Silicon Technology, Application Center Power Electronics for Renewable Energy Systems. Their cooperation is hereby gratefully acknowledged.

I hereby declare that I produced the present work myself, only using the help of the indicated aids and sources.

Hamburg, September 21, 2018 Jörg Michael Dietrich Richter

Abstract

In this thesis a multiobjective tuning of a linear state signal shaping model predictive control (LSSSMPC) controller is implemented in an electrical distribution grid to provide power quality services. The tuning is done using the evolutionary algorithm Multiobjective Differential Evolution with Spherical Pruning X (spMODEx). Two research questions are addressed. In the first stage the reproducibility of the spMODEx algorithm, when approximating the Pareto Front, as the solution to the multiobjective problem statement, is addressed. The assessment is realized by means of singular value decomposition, and additionally by a novel approach the activated volume method, first reported herein. In the second stage a decision making strategy is developed to find the best controller parameters in a reasonable amount of time. Controller and plant are operated in a mismatch. The controller operates on a conventional linear state space model, while the plant simulation is done by a four mode switched system to adequately model the behavior of non–linear loads. The thesis concludes with the outcomes on the reproducibility of spMODEx algorithm, the activated volume method, and recommendations for a successful multiobjective optimization and decision making process to ensure tuning parameters that allow the LSSSMPC controller to provide optimal power quality services.

Table of Contents

List of Figures

List of Tables

Acknowledgments

I didn't expect that writing my master thesis would become such a wonderful joy ride, full of excitement, challenges, growth in knowledge, enjoyable moments, and hard effort, sprinkled with the occasional frustration. What also surprised me is that it is possible to work very long hours for a prolonged period of time, and come out at the other end relatively unharmed. All of this would however not have been possible without the help and encouragement of many people.

First I'd like to thank Prof. Dr.-Ing. habil. Gerwald Lichtenberg for supervising my thesis, and sharing his knowledge and insight about the correct style of working scientifically. As my second supervisor I'd like to thank Dr.-Ing. Georg Pangalos for guiding me in my effort to conquer the jungle of simulation, control and optimization. Beyond that especially for the meaningful conversations and honest opinions about different aspects of life. I appreciated these conversations a lot. As my supervisor on set, so to speak, I'd like thank Carlos Cateriano Yáñes for supporting me in focusing my effort on the important aspects, and for enjoying the sometimes endless discussions about small details and overarching topics to nail down their precise meaning, just as much as I did. If you should ever be in need of a random fact, let me know! I'd also like to thank Kathrin Weihe for the shared journey to a master degree, the mutual desire to understand, discuss and share epiphanies in related and unrelated topics. I'd also like to thank her for helping me battle the LaTeX monster.

As the head of Application Center Power Electronics for Renewable Energy System of the Fraunhofer ISIT, I'd like to thank Prof. Dr. Frerk Haase for letting me conduct my master thesis here. I'd like to thank Prof. Dr.-Ing. Hans Schäfers for providing me the idea on the activated volume method, which thus contributed to be a major part of this thesis.

The experience would not have been half as enjoyable without every single one of my colleagues here at the application center. I am grateful to Ali Aneissi, Anna Meißner, Anton Gorodnichev, Eivind Langnes, Felix Manthey, Henri Zeller, Ilhami Özen, Julian

Franz, Malte Päsler, and Marlene Nötzold for their time, support and conversations shared at work, lunch, and outside in the real world.

Lastly, I thank my loving parents Irmingard and Detlev Richter, who always support me in the minute and grand things of life. And my brother Nickolas Richter, who was foolish enough to offer me to read the first draft of the second chapter. To put it in the words of the unrevised document. “One might wonder, what would have been the outcome off this thesis”. Your comments on it, and conversations apart from the thesis are greatly appreciated.

Hamburg,
September 21, 2018

Jörg Michael Dietrich Richter

Chapter 1

Introduction

1-1 Motivation

This thesis was written in the framework of the project Norddeutsche EnergieWende 4.0. The projects goal is to develop strategies to supply the two northern German states Hamburg and Schleswig-Holstein with 100 % reliable, renewable energy by the end of 2035. A twin strategy is to be employed, which consists of increasing power exports to other regions, and increasing the energy self–consumption ratio. The existing power grid is innovated into a sustainable energy system, by exploring novel concepts for system control and smart links between generation, distribution, storage and consumption. Transforming the network into a flexible and stable power system to adequately deal with the challenges of fluctuating demand and production of renewable energies, [3]. The work of this thesis deals with advancing the research into novel control methods for battery energy storage systems (BESSs) that ensure power system stability.

1-2 Scientific Problem

The system stability of electrical power systems is assessed by the electrical power quality (PQ). Several aspects such as voltage level, system frequency, power factor, and distortion content of voltages and currents are monitored constantly and have to be kept within acceptable limits, [4]. Guidelines and regulations exist, that restrict the presence of disturbances. This is for example implemented in Germany by the DIN EN 50160, which limits voltage level, frequency deviation, and total harmonic distortion (THD) content of voltages and currents among others. Strong deviations from the optimal parameters don't only lead to undersupply of customers and power losses in the power distribution, but can also have graver effects such as maloperation of supply, transmission, or demand equipment connected to the grid. It is therefor vital to ensure that power systems stay within these system limits, [4].

The pollution of the power system consists of two sources, natural and system related. Natural causes included disturbance due to equipment failure, faults, lightning, flashover, etc. The system related pollution mainly derives from devices connected to to the grid, and are strongest on the utilization level. The major source being solid–state controllers that transform alternating current (AC) into direct current (DC). Their share in power system has increased over the recent years. Solid–state controllers are necessary for feed controlled power devices such as computers, printers, furnaces, and adjustable speed drives, to name a few. Additionally, renewable energies heavily rely on solid–state controllers to transfer generated power to the gird. This allows to decoupled the generation from the grid, and its requirements to for example the same rotational frequency. The decoupling thus allows a higher performance and an overall

increase in power production. Despite their negative effects, solid–state controllers are indispensable due to the stark increase in energy–efficiency that they provide, [4].

To mitigate the negative effects two main strategies are used. Passive mitigation strategies rely on passive electrical components to compensate undesired behavior. They consist of L-C filters that are capable of canceling out the effects of THDs and are also used for power factor correction at a low cost. Due to their fixed compensation, large size, and danger of resonance they are not always ideal. Active strategies rely on solid–state compensators that are capable of actively negateing the negative effects of the disturbances. These devices are generally known as active power filter (APF) and provide the power systems with dynamic voltage and current support. They usually draw the power needed directly from the grid, and reinject it in a controlled way to stabilize the power system. Classical control strategies of APFs are instantaneous reactive power theory, synchronous frame d-q theory, and synchronous detection method, [4].

At the Fraunhofer Institute for Silicon Technology new control strategies are being explored for providing PQ services to the grid. A BESS is developed to support the power system with energy, solving two problems at the same time. Fluctuating renewable energy needs to be stored to bridge the gap between supply and demand, which do not always coincides. Additionally, compensating the distortion caused by the increasing renewable energy share and stabilizing the PQ. Opposed to the conventional control strategies mentioned above, the BESS is to be operated by a model predictive control (MPC) controller. MPC is an advanced control method that is designed to incorporate predictions about the system into the solution of the optimization problem in order to control it, [5]. The advantage is that in later stages forecasts about power supply, demand, and electricity prices are balanced with the current PQ demand of the system to operate the BESS in an economical way that additionally provides system stability.

Presently, the controller is at a stage where it achieves the compensation of THD, as a negative effect on the PQ, to some degree. The control strategy employed is based on linear state signal shaping model predictive control (LSSSMPC), that was recently reported as a new method to ensure the sinusoidal shape of a voltage or current signal. The potential applications of LSSSMPC go beyond power system, as any shape class that can be expressed by difference equations can be used, [6]. The focus of the present effort to improve the controller is two fold. The first effort is to apply constraints, to always ensure a stable behavior of the controller. The second effort is to tune the parameters of the controller to ensure a desired compensation mode, which is at the center of this thesis.

1-3 Methods of Solution

The manner in which a controller compensates any system is highly dependent on the adjustable parameters of the controller. The wrong choice of parameters leads to negative behavior, that can ultimately be detrimental to the system which is to be controlled. The field that is concerned with finding the right parameters for a controller is generally known as controller tuning. There exist multiple ways how the right set of parameters can be defined, and ultimately depends on what the decision maker (DM) defines them to be. Different criteria such as responds time, control error, and control quality of one signal opposed to an other signal can be regarded. Depending on the control case preferences may vary. The challenge of finding the optimal tuning parameters or set points (SPs) of a controller can be stated as a minimization, in the form of a multiobjective problem (MOP). The individual cost functions of the MOP representing different design criteria of the controller, [2].

The solution of a MOP can generally be achieved in two ways. The first is the aggregate objective function (AOF) approach. Each cost function of the MOP is decreased to attain one solution that has the smallest overall cost. The outcome of this optimization is highly depended on the way in which each sub cost function is weighted in the process. It is therefore highly depended on the preference of the DM. The second approach is known as the generate first choose later (GFCL) approach. This approach is designed generate solutions which solely reflect the best capabilities of the controller to compensate the system. Only Pareto optimal solutions are of interest, and the solution set is generally referred to as the Pareto Front (PF) of the controller. These are solutions which are non–dominated in their sub cost function values. It is impossible to state which individual solution is better without an additional weighting criteria. One or several potential SPs are chosen in a second step known as the decision making process, according to the preferences of the DM. This has the additional advantage that the DM attains knowledge about all capabilities of the controller, to come to a well informed conclusion, [2].

Up until this point, a multiobjective controller tuning has not been applied to the LSSSMPC, and the range of the controllers capabilities to provide PQ services is unexplored. A multiobjective controller tuning will be applied to the LSSSMPC to find its PF. The implementation of the tuning process is done using an evolutionary algorithm (EA). A purely analytical investigation is discarded, because the solution of the LSSSMPC cost function is of a non–linear nature. Combined with non–linear measurements of the system outputs, it is assumed that connection between the tuning parameters and the system behavior is non–linear itself. The algorithm used is the Multiobjective Differential Evolution with Spherical Pruning X (spMODEx) algorithm. It applies the EA Differential Evolution (DE) in conjunction with an archive. The archive is reduced by spherical pruning, which is an algorithm that aims to ensure a

good spread over the whole PF during the solution of the MOP.

As the spMODEx algorithm has never been applied to a LSSSMPC controller, the first research question that needs to be addressed is how reproducible the EA approximates the PF in repeated runs. In the first experiment presented here, this question is explored. A linear state space model of an electrical distribution grid with non–linear loads is used as a simulation basis, where the THD of the currents on the transmission lines is to be reduced. The assessment of the reproducibility is done by comparing individual PF solutions with an overall solution, by existing methods, and by a novel analyzation method called the activated volume method (AVM).

The second research question is concerned with the application of the decision making process itself, in a simulation scenario that is closer to reality than the first experiment. A decision making strategy is developed that is grounded in the application of regulation, system efficiency, and the application of a visualization method known as level diagrams. The electrical distribution grid will be simulated using a four mode switched system that employs linear state space models to simulate the non–linear circuit components. The LSSSMPC operates with a model mismatch, only having access to the same model as in experiment one. This will contribute the additional strain of a more life like system, where controller and plant operate in mismatch.

1-4 Structure of the Thesis

The structure of the thesis is as follows. The theoretical framework of the thesis will pointed out in chapter 2. It introduces the necessary knowledge about power system, predictive control theory and multiobjective optimization. Chapter 3 covers the general control and simulation strategy, the integration of the MPC controller into the multiobjective algorithm, and its cost functions. Additionally the design of experiment one and two, and the electrical circuits that were used as grid models are covered. The results and analysis about the assessment of the reproducibility of spMODEx are given in chapter 4. The second experiment which concerns itself with the actual application of the controller tuning and the decision making process is presented in chapter 5. Chapter 6 concludes the thesis consisting of a summary on the reproducibility of spMODEx algorithm, the activated volume method, and recommendations for a successful multiobjective optimization and decision making process to ensure tuning parameters that allow the LSSSMPC controller to provide optimal power quality services. New directions for future research are pointed.

Chapter 2

Theoretical Framework

This chapter provides the theoretical framework of the thesis. On the next page a note on the usage of variables is given and should be read to avoid confusion. In the first section of this chapter the necessary overview of power systems is given. Next, predictive control theory is covered, followed by the necessary topics about multiobjective optimization. The chapter closes with the section that covers the spMODEx algorithm, that was used in this thesis for the controller tuning.

The following chapter will provide the theoretical framework necessary for this thesis. Because a wide number of topics is covered a lot of different variables and accompanying subscripts and superscripts are used. To prevent confusion, a consistent notation is necessary. At the same time, exceptions needed to be made, to preserve the commonly accepted notation used in the field that is covered. The following description introduces a set of rules, that were tried to be followed when ever possible. But, as with every rule, exceptions needed to be made at times.

Variables are represented by a none bold lower or upper case letter as v or V. They can have multi–letter indices, also separated by commas. For example $V_{A,max}$ represents the maximum voltage in line A.

Matrices are written as a bold upper case letter such as $\mathbf{X}$. Vectors are generally written as a bold lower case letter such as $\mathbf{x}$, but can also be written as an bold upper case letter such as $\mathbf{J}$, representing a matrix with one row and multiple columns or vice versa. For matrices and vectors, a subscript or superscript that is written as a bold upper or lower case letter, is an addition to the name. So $\mathbf{p}$ in the matrix $\mathbf{X_p}$ does not indicate an element.

Indices or counters, that refer to elements of a matrix, are written in plain and are separated by a comma from the variable name, if an index already exists in form of a bold case letter. Otherwise the first comma is omitted. A matrix $\mathbf{X}_{\mathbf{p},p,o}$, is the matrix $\mathbf{X_p}$, of which the entries p and o are specified. Same is true for the matrix $\mathbf{X}_{p,o}$. Using the same letter twice is tried to be avoided, and should just serve as an overly clear example.

Indices that specify the size of a matrix or vector carry an inverted hat. Their use is not limited to the sections in which they are specified. They can be lower or upper case. Matrix $\mathbf{X_p} \in \mathbb{R}^{\check{p}\times\check{o}}$ can have its entries specified by $\mathbf{X}_{\mathbf{p},p,o}$. The indices specifying an element range from $p \in \{1, 2, \ldots, \check{p}\}$ and $o \in \{1, 2, \ldots, \check{o}\}$. The same matrix could also be counted by $\mathbf{X}_{\mathbf{p},i,j}$, where $i \in \{1, 2, \ldots, \check{p}\}$ and $j \in \{1, 2, \ldots, \check{o}\}$. So while the counters are interchangeable, the sizes of matrices are not. Counters are tried to be used consistently whenever possible.

Greek lower case letters are never written bold, as in θ, and can still specify a vector when having indices, but also a variable when not. Greek letters upper case however are written as bold letters such as $\mathbf{\Theta}$, specifying a matrix.

Especially in the sections on multiobjective optimization superscripts are introduced, as they are used in literature. A set of $\check{i}$ vectors ζ, with $\check{j}$ entries each, is specified in its dimensions by $\zeta \in \mathbb{R}^{\check{i}\times\check{j}}$. Its jth entry of the ith individual is specified by ζ^i_j. Furhter, an additional index $|_G$, that specifies the generation counter is used. The maximum generation is thus specified by $|_{\check{G}}$.

2-1 Power Systems

2-1-1 Fundamentals of Electrical Power Systems

This section introduces the fundamental concepts of electrical power systems. The relationship between power, voltage and current is introduced. Next the connection with resistive, inductive and capacitve loads is covererd, and their behavior in electrical circuits is examined briefly. The importance of reactive and active power are and their connection to the phase-shift are laid out. The equations, graphs and explanations are taken from, [7].

In electrical systems, the behavior of the instantaneous power $p(t)$ at the time t is described in it's physical relationship to the voltage $v(t)$ and the current flow $i(t)$ by the mathematical equation

$$p(t) = v(t)i(t)\,, \tag{2-1}$$

where t is measured in s, $p(t)$ is measured in watt (W), $v(t)$ is measured in volt (V), and $i(t)$ is measured in ampere(A). The power is usually provided by a generator, which transforms mechanical energy into electrical. The behavior of voltage and current over time follows a mathematical sine wave, because the generator are rotating machines. Voltage and current are thus described by

$$v(t) = V_{max}\sin(\omega t + \varphi)\,, \tag{2-2}$$
$$i(t) = I_{max}\sin(\omega t + \varphi)\,, \tag{2-3}$$

where $\omega = 2\pi f$ is the angular velocity of the generator, f is the frequency measured in Hertz (Hz), and φ is the phase shift between $v(t)$ and $i(t)$, measured in radian(rad) or degree (°). The maximum amplitudes of voltage and current are given by V_{max} and I_{max}, respectively. The voltage output of the generator changes it's sign over time, and is therefor of alternating current. These systems are named alternating current (AC) systems, as opposed to systems with a steady voltage or direct current (DC) systems. To transfer power, current has to flow over a resistor, where the voltage experiences a drop in its magnitude. This is behavior is captured by the Ohm's law as

$$v(t) = R\,i(t)\,, \tag{2-4}$$

where R is the resistance measured in Ohm (Ω). The behavior of voltages and currents in electrical networks is captured by the Kirchhoff law of voltage and current. The Kirchhoff's voltage law states, that the sum of all voltages around an electronic circuit loop has to add up to zero. The Kirchhoff's current law states, that the sum of all currents at a node has to add up to zero. The graphical depiction of these laws can be seen in figure 2-1.

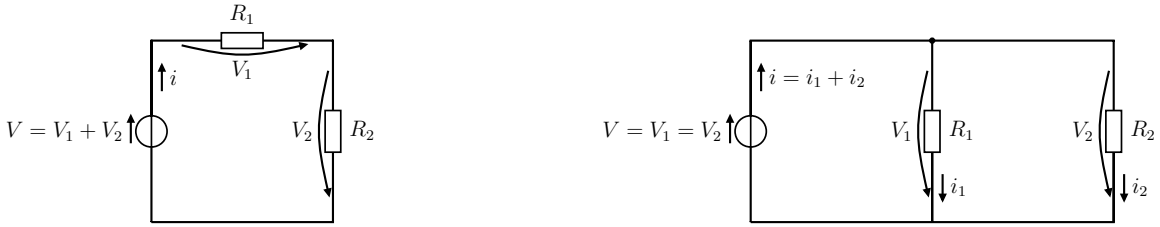

a) Kirchhoff's voltage law. **b)** Kirchhoff's current law.

Figure 2-1: Graphical representation of Kirchhoff's voltage and current law.

There are two other fundamental components with which voltages and currents can interact. These are electro–magnetic coils, and capacitors. Every current flowing in a wire induces a magnetic field around the wire. A coil as a wound up piece of wire amplifies this electro–magnetic effect. However, the changing magnetic field induces a voltage around the coil, which is opposite to the current flow that induced the magnetic field in the first place. It is for this reason, that the time behavior of the voltage around a coil is a function of the change of current flowing through the coil. This is described by

$$v(t) = L \frac{\mathrm{d}i(t)}{\mathrm{d}t}\,, \tag{2-5}$$

where L is the inductance of the coil measured in Henry (H).

A capacitor is a device that can temporarily hold a small charge in itself. It consist of two conducting surfaces, which are separated by an insulator. This can be achieved by two metal surfaces which are separated by an air gap. When the surfaces are charged with an electric current of opposite sign, the charges in each plate will be attracted to one another. In an electrical circuit, this device leads to a behavior which is described by

$$i(t) = C \frac{\mathrm{d}v(t)}{\mathrm{d}t}\,, \tag{2-6}$$

where C is the capacitance measured in Farad (F). The two effects described above each lead to a time delay between voltage and current. This time shift is given by the phase angle and was already introduced in equations (2-2) and (2-3). A purely inductive load, or purely capacitive load will lead to a phase shift of exactly 90°/-90°or $\frac{\pi}{2}/-\frac{\pi}{2}$, respectively, for a sinusoidal signal. An example for an inductive load is given below

$$\begin{aligned} v(t) =& LI_{max} \frac{\mathrm{d}}{\mathrm{d}t} \sin(\omega t + \varphi)\,, & (2\text{-}7)\\ =& \omega L I_{max} \cos(\omega t + \varphi)\,. & (2\text{-}8) \end{aligned}$$

The additional term ω appeared through derivation. It shows, that the voltage induced by a alternating current actually depends on the frequency, with which the current alternates. The voltage signal can be seen to develop with the cosine, while the current develops with the sine. This effect on voltage and current is said to be of reactive nature, which is why these circuit elements are called reactances. They react to changes in the system.

When the power is calculated by equation (2-1), a phase shift of exactly $\varphi = \pm\frac{\pi}{2}$ will result in a power which is positive for half the time and negative for the other half. The meaning is, that on average no power is transferred into the coil. Yet additional current flows on the transmission line through the coil. As all transmission lines have a real resistance, this will lead to a power losses, even though no net power is transferred into the coil or capacitor. This is the reason, why a phase shift between voltage and current should be avoided as much as possible.

The behavior of the power flow in relationship to the phase shift between voltage and current can be accurately described using complex numbers. Given, that the voltage and current are perfect sine waves, the system can be described in phasor form. The complex apparent power $\mathbf{S}$ is given by

$$\mathbf{S} = \mathbf{V}\mathbf{I}^* \,, \tag{2-9}$$

where $\mathbf{V}$ is the complex voltage, and the current is described by its complex conjugate $\mathbf{I}^*$.[1] Voltage and current are connected via the reformulation of Ohm's law

$$\mathbf{V} = \mathbf{Z}\mathbf{I} \,, \tag{2-10}$$

where $\mathbf{Z}$ is the impedance, which is given by

$$\mathbf{Z} = R + jX \,, \tag{2-11}$$

where R is the resistance as in equation (2-4), and X is the reactance which is generated by a coil or a capacitor and j as the imaginary unit.[2] The reactance of a coil is calculated by

$$X_L = \omega L \,, \tag{2-12}$$

and calculated for a capacitor as,

$$X_C = -\frac{1}{\omega C} \,. \tag{2-13}$$

[1] In this chapter, the boldface font indicates that the variable is a complex number. This typesetting is reserved for vectors and matrices in the other chapters.

[2] Only in this subsection does j stand for the imaginary unit. It will be used as a counter in later subsections

The subscript indicates the nature of the reactance (inductive for a coil, capacitive for a capacitor), L and C are component-specific magnitudes of coil or capacitor used in the circuit.

The average magnitude of voltage and current in an AC circuit are calculated as the root mean square (rms) value of the sinusoidal signal. The rms is calculated by squaring the signal, integrating it, and then taking the square root. An example for the voltage is

$$V_{rms} = \sqrt{\frac{1}{T}\int_{t_0}^{t_0+T} v(t)^2 \mathrm{d}t}\,, \tag{2-14}$$

$$V_{rms} = \sqrt{\frac{1}{T}\int_{t_0}^{t_0+T} V_{max}^2 \sin(\omega t)^2 \mathrm{d}t}\,, \tag{2-15}$$

where T is the time for one period, and t_0 is the starting time usually set to $t_0 = 0$. Without going into further detail of the calculation the solution for a sine wave is

$$V_{rms} = \frac{1}{\sqrt{2}} V_{max}\,, \tag{2-16}$$

where V_{rms} is the magnitude of the complex voltage $\mathbf{V}$. The same can be done for the current. To describing the phase shift between voltage $\mathbf{V}$ and current $\mathbf{I}$, one of them needs to act as a reference, which is usually done with the voltage.

A complex number can be expressed as the sum of a real and an imaginary number, or by expressing it in phasor form, such as

$$a + jb = r\mathrm{e}^{j\varphi}\,, \tag{2-17}$$

where

$$r = \sqrt{a^2 + b^2}\,, \tag{2-18}$$

$$\varphi = \tan\left(\frac{b}{a}\right)\,, \tag{2-19}$$

where j is the imaginary number. An even shorter notation in power systems is to exchange the $r\mathrm{e}^{j\varphi}$ by $r\angle\varphi$. Then Ohm's law becomes

$$V\angle 0^\circ = I\angle(-\varphi)\, Z\angle(\varphi)\,. \tag{2-20}$$

The complex power $\mathbf{S}$ can be decomposed into its real power P and the reactive power Q by

$$\mathbf{S} = P + jQ = S\angle\varphi\,, \tag{2-21}$$

where

$$S = \quad I_{rms}V_{rms}\,, \tag{2-22}$$
$$P = I_{rms}V_{rms}\cos(\varphi)\,, \tag{2-23}$$
$$Q = I_{rms}V_{rms}\sin(\varphi)\,. \tag{2-24}$$

The real power P is an accurate description of the actual power that is transferred in the power system. The reactive power Q is the part, which oscillates between the power supply and the impedance. The term $\cos(\varphi)$ is named the power factor, because it is the factor with which the magnitude of the apparent power $\mathbf{S}$ is multiplied by, to result in the actual transferred power, [7].

2-1-2 Total Harmonic Distortions

In an ideal power system, voltage and current oscillate with perfect sine/cosine waves, as a direct result from the way electricity is produced by rotating generators. Apart from transient disturbances like none repeating voltage spikes, periodic disturbances can occur due to imperfect loads and generators. Manifestations in the voltage usually indicate generators as the source, while current–distortions typically originate from the loads. These distortions lead to a deviation from the pure sinusoidal waveform. Purely resistive loads are generally unaffected by these disturbance. Inductive or capacitave components are effected stronger, because the magnitude of the impedance depends on the frequency of the signal. As coils and capacitors are major componets of motors and transformers, distortions can potentially lead to overheating and a decrease in lifespan, [7]. Main sources of harmonic distrotion from the load side are arc furnaces, static power converters, electrochemical power supplies, adjustable speed drivers, AC-DC converters (also known as rectifiers), and others, [8].

Mathematically, any periodic signal can be expressed by an infinite sum of sinusoids of varying frequency and amplitude. For periodic distortions to be observable in the voltage/current signal it must be multiples of the base-frequency used by the power system (in Europe 50 Hz). These multiples are referred to as the harmonics of the base-frequency. The harmonic content of a signal is measured in percent and is known as the total harmonic distortion (THD) of the system. The decomposition of the time signal into its harmonic components is done via the Fourier analysis, [7].

An additional negative effect of the THD on electrical power systems is owed to the symmetric nature of three phase systems, which leads to power loss and excess current on the neutral conductor. Common ways to connect voltage lines in three phases are the delta conncetion and the wye connection, [7]. These can be seen in figure 2-2. With three different phases A, B, and C the relationship between their voltage-supply

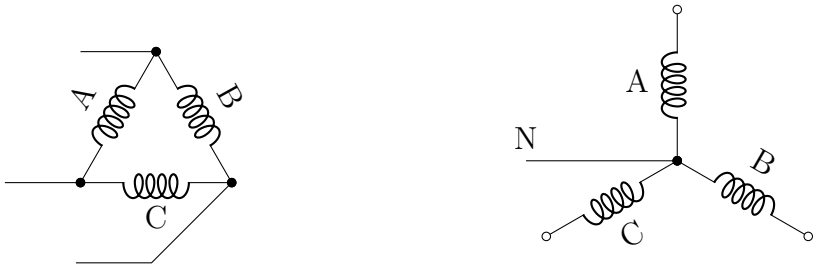

a) Delta connection. **b)** Wye connection.

Figure 2-2: Delta and Wye connection of a three phase system.

is described by a 120° phase/time shift between them as, [7]

$$V_A(t) = V_{A,max} \sin(\omega t + 0°)\,, \tag{2-25}$$
$$V_B(t) = V_{B,max} \sin(\omega t + 120°)\,, \tag{2-26}$$
$$V_C(t) = V_{C,max} \sin(\omega t + 240°)\,. \tag{2-27}$$

With $V_x(t)$ being the voltage at a given time t in the referenced phases. The amplitude $V_{x,max}$ being the maximum value of the voltage, and $\omega = 2\pi f$ as the angular velocity, where f is the fundamental frequency of the power system measured in Hz. These equations describe the ideal case in a power system. Considering a description of any periodic signal by the Fourier-decomposition, the equations become

$$V_A(t) = \sum_{h=1}^{\check{h}} V_{A,max,h} \sin(h\omega t + 0°)\,, \tag{2-28}$$
$$V_B(t) = \sum_{h=1}^{\check{h}} V_{B,max,h} \sin(h\omega t + 120°)\,, \tag{2-29}$$
$$V_C(t) = \sum_{h=1}^{\check{h}} V_{C,max,h} \sin(h\omega t + 240°)\,. \tag{2-30}$$

With $h \in \{1, 2, \ldots \check{h}\}$ and $\check{h}$ as the integer of the last harmonics included, $V_{x,max,h}$ as the amplitude of the harmonics. The description of the currents follows as

$$I_A(t) = \sum_{h=1}^{\check{h}} I_{A,max,h} \sin(h\omega t + 0° + \varphi_A)\,, \tag{2-31}$$
$$I_B(t) = \sum_{h=1}^{\check{h}} I_{B,max,h} \sin(h\omega t + 120° + \varphi_B)\,, \tag{2-32}$$
$$I_C(t) = \sum_{h=1}^{\check{h}} I_{C,max,h} \sin(h\omega t + 240° + \varphi_C)\,. \tag{2-33}$$

With $I_x(t)$ as time devolpment in the phase x, and $I_{x,max,h}$ as the amplidude of the harmonic. The phase shift between voltages and currents is given by φ_x. In a wye-connection the currents on the neutral line are described by $I_N(t) = I_A(t)+I_B(t)+I_C(t)$, with $I_N(t)$ as the ground current. While almost all currents cancel out, harmonics being a multiples of 3 (triplets) add up, resulting in an unwanted power transfer to ground, [9]. A similar effect happens in delta-connected transformers, where the power of the $3rd$ harmonic can't be transferred. Since every third integer is a multiple of 3, a third of the power contained in the harmonics is lost, [7].

The total harmonic distortion of a signal can be measured in two ways. Either, the harmonic content is compared to the fundamental frequency of the signal, or it is related to the rms value of the waveform analyzed. Equations (2-34) and (2-35) show their calculation, [10]

$$THD_F = \frac{\sqrt{\sum_{h=2}^{\check{h}} A_h^2}}{A_1}\,, \tag{2-34}$$

$$THD_R = \sqrt{\frac{\sum_{h=2}^{\check{h}} A_h^2}{\sum_{h=1}^{\inf} A_h^2}}\,. \tag{2-35}$$

Where THD_F is the total harmonic distortion referred to the fundamental, THD_R the total harmonic distortion referred to the rms. Index h stands for the total number of harmonics analyzed, $h \in \{1, 2, \ldots, \check{h}\}$, with $\check{h}$ as the last considered harmonic. The maximum amplitudes A_h of the harmonics from $h = 2, \ldots, \check{h}$. The fundamental frequency of the signal is at $h = 1$. While THD_F can technically range between 0 and ∞ (when $A_1 \to 0$), THD_R can only range between 0 and 1, [10].

A comparison of the two ways of measuring has shown, that the THD_F is the better measure to analyze the THD content of a sinusoidal waveform. This is because it is more sensitive to changes in the amplitudes. As measurements are always afflicted by measurement-error, it is advised to always use THD_F, [10]. In this work only equation (2-34) is used for THD assessment.

2-1-3 Compensation of Total Harmonic Distortions

To prevent the negative effects that result from THD several compensation strategies have been developed. The simplest strategy is the combination of coils and inductances to create passive filters. These so called L-C filters are capable of reducing harmonic content and also of improving the power factor of the system. Major drawbacks however include their large size, fixed compensation capacity, and the threat of imposing resonance oscillation. More recently developed advanced compensation strategies are

capable of actively influencing a wider range of power quality factors. These devices are generally known as active power filters (APFs) an can positively influence harmonic content, power factor, load balancing, voltage balancing at the point of common coupling (PCC), and compensation of currents on the neutral conductor. The PCC is a point where various loads are connected [4].

They can be designed in series or in shunt connection to the grid. APFs are connected in series into circuit via an inductance. The series APF injects voltage into the system, by providing a second inductance with current, which elector magnetically induces a voltage into the transmission line. Shunt APFs are connected in parallel to the PCC via an inductance. To positively influence the power quality currents are directly injected to the PCC. To calculate the required compensation signal different approaches are used, such as instantaneous reactive power theory, synchronous frame d–q theory and synchronous detection method. The power required for compensation is directly drawn from the grid, and is stored in an intermediate storage in the form of capacitors or inductances. They further require systems specific measurement equipment in the form of filters, and have to be designed in their rating of up to 80 % of the of the application that needs to be compensated. This makes them very costly in comparison to passive strategies.

At the Fraunhofer Institute for Silicone Technologies, new compensation methods are explored to provide power quality services, such as harmonics compensation, to the grid. The envisioned compensation design consists of a battery energy storage system (BESS) and a compensation source, that is connected in shunt to the grid. The BESS acts as a reservoir to store excess power that is provided by renewable energies. If energy production from renewables is low, or power quality correction is required, the suggested system will support the power grid by reinjecting the renewable energy with the appropriate signal shape.

Instead of employing the classical theory mentioned above, an advanced control strategy will be used. This strategy is known as model predictive control (MPC) and is the focus of the next section. The method relies on describing the compensation problem by ordinary differential equations, and calculates the optimal compensation sequence by solving a least square problem. Controllers of this design have a wide range of application but have not yet been implemented on a broader scale for THD compensation and other power quality services.

Some advantages are expected to be acquired in the long term. The design is less dependent on system specific components at the location where it is employed. The power rating of the compensation source (CS) has to be designed in accordance with the power rating of the battery storage, and the desired compensation capacity, but the MPC controller only needs the time sequence of voltages and currents in the system. Once these signals are measured and transferred to the controller, the signal processing

can be done on a digital processor. Changes in the power system components on site can be easily implemented in the controller by updating the control model. One of the most important features however is that MPC allows the integration of further aspects, such as operational cost, electricity prices, demand forecast, etc. into the solution of the optimization problem. This will allow the controller to always operate in an economically optimal way in later stages of the project.

The next section will detail the necessary control theory.

2-2 Predictive Control Theory

This section covers the necessary control theory of the thesis. In the first subsection linear state space models are introduces, followed by a short introduction into the controller plant idea. MPC theory will by the focus of the next three subsections thereafter, concerning the problem statement, stable solution, and linear state signal shaping model predictive control.

2-2-1 Linear State Space Models

This subsection covers the basics of state space models and how they can be used to describe physical systems. State space models are systems of equations that can describe the mathematical relationship between mass, momentum and energy of physical systems. Many physical system can either be described by differential or by difference equations. The systems can be split into states of the system, inputs and outputs to the system, and the systems dynamics. The general form of a state space model to reflects this is, [11]

$$\frac{\mathrm{d}\mathbf{x}}{\mathrm{d}t} = f(\mathbf{x}, \mathbf{u})\,, \tag{2-36}$$

$$\mathbf{y} = h(\mathbf{x}, \mathbf{u})\,. \tag{2-37}$$

The states are given by the vector $\mathbf{x} \in \mathbb{R}^{\check{n}}$, where $\check{n}$ is the number of states. The controllable inputs are given by the vector $\mathbf{u} \in \mathbb{R}^{\check{p}}$, where $\check{p}$ is the number of inputs. The outputs are given by the vector $\mathbf{y} \in \mathbb{R}^{\check{q}}$, where $\check{q}$ is the number of outputs. The functions map for $f : \mathbb{R}^{\check{n}} \times \mathbb{R}^{\check{p}} \to \mathbb{R}^{\check{n}}$, and for $h : \mathbb{R}^{\check{n}} \times \mathbb{R}^{\check{q}} \to \mathbb{R}^{\check{q}}$. Because functions f and h don't explicitly depend on time, these systems are called *time-invariant*. The total number of states is referred to as the *order* of the system. As long as functions f and h are linear combinations of $\mathbf{x}$ and $\mathbf{u}$ the system is a linear state space model and can be written as, [11]

$$\frac{\mathrm{d}\mathbf{x}}{\mathrm{d}t} = \mathbf{A_c}\mathbf{x} + \mathbf{B_c}\mathbf{u}\,, \tag{2-38}$$

$$\mathbf{y} = \mathbf{C_c}\mathbf{x} + \mathbf{D_c}\mathbf{u}\,. \tag{2-39}$$

With $\mathbf{A_c}$ being the *system matrix*, $\mathbf{B_c}$ being *input matrix*, $\mathbf{C_c}$ the *output matrix*, and $\mathbf{D_c}$ the *direct feedthrough matrix* of the system. These matrices are system specific. The subscript indicates a continuous time model. A system of this form is also known as a linear time-invariant system (LTI). Many systems don't have a direct feedthrough from the input $\mathbf{u}$ to the output $\mathbf{y}$, and their direct feedthrough matrix $\mathbf{D_c}$ contains only

zeros, [11]. The dimensions of these matrices are descriped by, [12]

$$\left(\begin{array}{c|c} \mathbf{A_c} & \mathbf{B_c} \\ \hline \mathbf{C_c} & \mathbf{D_c} \end{array}\right) \in \left[\begin{array}{c|c} \mathbb{R}^{\check{n}\times\check{n}} & \mathbb{R}^{\check{n}\times\check{p}} \\ \hline \mathbb{R}^{\check{q}\times\check{n}} & \mathbb{R}^{\check{q}\times\check{p}} \end{array}\right] \equiv \mathbb{R}^{(\check{q}+\check{n})\times(\check{n}+\check{p})} \,. \tag{2-40}$$

Difference equations in the form of an LTI can be described in a similar way. Instead of using a continuous time t, the time-steps follow the integers $k = 0, 1, \ldots \check{k}$, with $\check{k}$ as the final time step. These linear discrete–time systems follow essentially the same structure as the continuous ones. They are written in matrix form as, [11]

$$\mathbf{x}_{k+1} = \mathbf{A}\mathbf{x}_k + \mathbf{B}\mathbf{u}_k \,, \tag{2-41}$$
$$\mathbf{y}_k = \mathbf{C}\mathbf{x}_k + \mathbf{D}\mathbf{u}_k \,. \tag{2-42}$$

The dimensions of the matrices $\mathbf{A}, \mathbf{B}, \mathbf{C},$ and $\mathbf{D}$ are the same as in equation (2-40).

The transformation between continuous and discrete time can be done in several ways. In this work the *zero order hold* is used. The development of the states at time t, where $t_k \leq t \leq t_{k+1}$ is given by, [13]

$$\mathbf{x}(t) = \mathrm{e}^{\mathbf{A_c}(t-t_k)}\mathbf{x}(t_k) + \int_{t_k}^{t} \mathrm{e}^{\mathbf{A_c}(t-s')}\mathbf{B_c}\mathbf{u}(s')\mathrm{d}s' \,, \tag{2-43}$$
$$= \mathrm{e}^{\mathbf{A_c}(t-t_k)}\mathbf{x}(t_k) + \int_{t_k}^{t} \mathrm{e}^{\mathbf{A_c}(t-s')}\mathrm{d}s'\,\mathbf{B_c}\mathbf{u}(t_k) \,, \tag{2-44}$$
$$= \mathrm{e}^{\mathbf{A_c}(t-t_k)}\mathbf{x}(t_k) + \int_{0}^{t-t_k} \mathrm{e}^{\mathbf{A_c}s}\mathrm{d}s\,\mathbf{B_c}\mathbf{u}(t_k) \,, \tag{2-45}$$
$$= \mathbf{A}(t,t_k)\mathbf{x}(t_k) + \mathbf{B}(t,t_k)\mathbf{u}(t_k) \,. \tag{2-46}$$

For a zero order hold $\mathbf{u}$ is held constant in-between sampling times, thus from (2-43) follows (2-44). The system equation follows as

$$\mathbf{x}(t_{k+1}) = \mathbf{A}(t_s)\mathbf{x}(t_k) + \mathbf{B}(t_s)\mathbf{u}(t_k) \,, \tag{2-47}$$
$$\mathbf{x}(t_k) = \mathbf{C}\mathbf{x}(t_k) + \mathbf{D}\mathbf{u}(t_k) \,, \tag{2-48}$$

where $t_s = t_{k+1} - t_k$ and with, [13]

$$\mathbf{A}(t_s) = \mathrm{e}^{\mathbf{A_c}(t_s)} \,, \tag{2-49}$$
$$\mathbf{B}(t_s) = \int_{0}^{t_s} \mathrm{e}^{\mathbf{A_c}s}\mathrm{d}s\,\mathbf{B_c} \,, \tag{2-50}$$
$$\mathbf{C} = \mathbf{C_c} \,, \tag{2-51}$$
$$\mathbf{D} = \mathbf{D_c} \,. \tag{2-52}$$

Having described a physical system in this way allows to control the system. The fundamental control idea is the content of the next subsections.

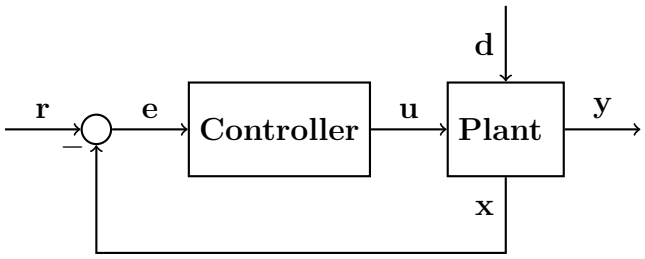

Figure 2-3: Controller plant model.

2-2-2 Controller Plant Systems

This subsection gives a brief overview of the central ideas in control systems. For a more detailed introduction see, [11].

Dynamic systems, usually respond to internal and external forces onto the system. External forces onto the system are referred to as inputs and disturbances, while internal forces are feedback from the system onto itself. The outward projected response of the system is referred to as the output. Remembering the state space model as in (2-41) and (2-42) the inputs to the system are given by $\mathbf{u}$, and the outputs are given by $\mathbf{y}$. The internal feedback mentioned above is given by the matrix $\mathbf{A}$. The matrix describes with which weights each state $\mathbf{x}$ influences itself and the other states in next time step, [11].

Physical systems usually don't exist on their own. Their might be two systems, *System 1* and *System 2*. *System 2* receives some outputs from *System 1* as inputs, creating its own outputs. Some of its output are fed back the first system. The challenge of the control engineer is, to design the second system in a way, that the first system produces a desired output. This is the basic idea of control systems, where a controller (*System 2*) controlls a plant (*System 1*), by utilizing information from the plants states or outputs, [11].

Figure 2-3 shows a graphical representation of a controller plant system as described above. The controller gives an input vector $\mathbf{u}$ to a plant. The plant is further influenced by a disturbance $\mathbf{d}$, and generates an output $\mathbf{y}$. The state vector $\mathbf{x}$ of the plant is subtracted from a reference vector $\mathbf{r}$, to form the tracking error $\mathbf{e}$. The tracking error is fed back to the controller. In this case, the controller doesn't receive the outputs but the states. This is known as state feedback. It is important to note, that in many cases the states of the plant are not readily accessible. In such a case the output of the plant is fed back, or an estimation of the states is done via an observer.

The goal of the controller is to minimize the tracking error $\mathbf{e}$. This can be achieved by multiplying $\mathbf{e}$ with a matrix to produce a linear combination of the tracking error vector. The linear combination is then fed back to the plant as $\mathbf{u}$. For successful control

the model of the plant needs to be known or at least approximated. This substitution model is then used, to design the feedback matrix of the controller in such a way that the desired plant behavior is achieved. While fairly simple to realize, this method has a major drawback. It merely responds to what has already happened. It does not allow to respond ahead of time to anticipated disturbances, which influence the plant in the future. To be able to do that a more advanced control method is necessary, which will be covered in the next subsection.

2-2-3 Model Predictive Control

An advanced system control method is model predictive control. It is a model based state feedback approach for controlling linear and non–linear systems. In this thesis, a linear MPC is used. In model predictive control the controller needs a model of the plant and its states While it does matter performance wise, whether the controller has access to the real model and states, MPC can even work when a model mismatch exist. Meaning, the model and states measured by the controller don't have to perfectly match the real model and states of the plant. The goal of the model predictive controller is to calculate the perfect input sequence, so that the plant behaves in the desired way, but doing so ahead of time. The controller can react to anticipated system changes by the use of predictions, allowing a faster and more precise control than conventional systems, [5].

The calculation of the perfect input sequence is done in-between two time steps of k. If the current discrete time step is $k-1$, the solution is to be found at time k. This means the whole optimization process takes place during the time $k-1 \leq t < k$. As the controller knows the current inputs and states of the plant, it can simulate ahead of time how the system will behave. The time frame until which a prediction for the system is made is known as the prediction Horizon $\check{H}_p$, where $\check{H}_p$ is the last time step until which the system is simulated. The models behavior is predicted for the integer time steps $k \in \left\langle 1, \ldots, \check{H}_p \right\rangle$. Since the last inputs to the system $\mathbf{u}_{k-1}$ and the last states $\mathbf{x}_{k-1}$ are known, the first future states $\mathbf{x}_k$ is accurately predicted (compare equations (2-41) and (2-41)), [5].

However for the following time step $k+1$ the controller input $\mathbf{u}_k$ is not yet determined. It is additionally possible to not apply inputs for the whole duration of the prediction horizon. Thus the control horizon $\check{H}_u$, is introduced. It specifies the last time step until which an input is made to the system. Therefor the prediction horizon can range from $k \leq \check{H}_u \leq \check{H}_p$, [5].

To calculate the optimal input sequence the problem is reformulated into a least squares problem The input sequence will therefor have the smallest quadratic difference, according to the design specifications which are made during the problem formulation. A

linear state space system $\mathbf{A}, \mathbf{B}, \mathbf{C}$, and $\mathbf{D}$ with inputs $\mathbf{u}$ is used. The input-vector $\mathbf{u}$ is reformulated into a difference sequence, [5], [12]

$$\mathbf{\Delta U}(k) = \begin{bmatrix} \Delta \mathbf{u}_k \\ \Delta \mathbf{u}_{k+1} \\ \vdots \\ \Delta \mathbf{u}_{k+\check{H}_u} \end{bmatrix} = \begin{bmatrix} \mathbf{u}_k & - & \mathbf{u}_{k-1} \\ \mathbf{u}_{k+1} & - & \mathbf{u}_k \\ \vdots & & \\ \mathbf{u}_{k+\check{H}_u} & - & \mathbf{u}_{k+\check{H}_u-1} \end{bmatrix}. \tag{2-53}$$

The prediction of the state sequence is thus described by, , [5]

$$\mathbf{X}(k) = \begin{bmatrix} \mathbf{x}_{k+1} \\ \vdots \\ \mathbf{x}_{k+\check{H}_p} \end{bmatrix} = \mathbf{\Psi} x_k + \mathbf{\Upsilon} u_{k-1} + \mathbf{\Theta \Delta U}(k)\,, \tag{2-54}$$

with

$$\mathbf{\Psi} = \begin{bmatrix} \mathbf{A} \\ \vdots \\ \mathbf{A}^{\check{H}_p} \end{bmatrix}, \tag{2-55}$$

$$\mathbf{\Upsilon} = \begin{bmatrix} \mathbf{B} \\ \vdots \\ \sum_{w=0}^{\check{H}_{p-1}} \mathbf{A}^w \mathbf{B} \end{bmatrix}, \tag{2-56}$$

$$\mathbf{\Theta} = \begin{bmatrix} \mathbf{B} & 0 & 0 & \dots & 0 \\ \mathbf{AB}+\mathbf{B} & \mathbf{B} & 0 & \dots & 0 \\ \mathbf{A}^2\mathbf{B}+\mathbf{AB}+\mathbf{B} & \mathbf{AB}+\mathbf{B} & \mathbf{B} & \dots & 0 \\ \vdots & \vdots & \vdots & \ddots & \vdots \\ \sum_{w=0}^{\check{H}_{p-1}} \mathbf{A}^w \mathbf{B} & \sum_{w=0}^{\check{H}_{p-2}} \mathbf{A}^w \mathbf{B} & \dots & \dots & \sum_{w=0}^{\check{H}_p-\check{H}_u} \mathbf{A}^w \mathbf{B} \end{bmatrix}. \tag{2-57}$$

The matrices $\mathbf{\Psi}$, $\mathbf{\Upsilon}$ and $\mathbf{\Theta}$ perform the successive application of the difference equation of the state space model described in (2-41). Each progressive forward step in time is compounded by each step that came before, [5].

For the calculation of the optimal input sequence the quadratic MPC cost function is created.[3] It calculates the weighted quadratic difference from the state to the reference, an the weighted square of each input difference. For each specific instant it is described by equation, , [5]

$$J(k) = \sum_{w=1}^{\check{H}_p} \parallel \mathbf{x}_{k+w} - \mathbf{r}_{k+w} \parallel^2_{\tilde{\mathbf{Q}}(w)} + \sum_{w=0}^{\check{H}_u} \parallel \Delta \mathbf{u}_{k+w} \parallel^2_{\tilde{\mathbf{R}}(w)}, \tag{2-58}$$

[3] In this chapter, cost function refers to the MPC cost-function. In the other chapters the word cost function refers to the cost-functions of the multiobjective algorithm if not stated otherwise.

where

$$\| \mathbf{e} \|^2_{\mathbf{M}} = \mathbf{e}'\mathbf{M}\mathbf{e}\,. \tag{2-59}$$

The prediction horizon is given by $\check{H}_p \in \mathbb{N}$, and the control horizon is given by $\check{H}_u \in \mathbb{N}$ and $\check{H}_u \leq \check{H}_p$. The vectors $\mathbf{r}_{k+w}$ are the state references, the states $\mathbf{x}_{k+w}$ and the input differences $\mathbf{u_{k+w}}$ in time step $k+w$. Matrix $\tilde{\mathbf{Q}}(w)$ describes the weights which are associated to each state reference difference. The matrix $\tilde{\mathbf{R}}(w)$ describing the weights for each change of input for time steps $k+w$. The cost $J(k)$ is to be minimized for the time-step k, [5] .

The two weighting matrices allow to influence the solution process by varying the their magnitude. In standard MPC these matrices have entries on the diagonal only, thus applying one weight to each state reference difference, and one to each input difference. Weights are usually not varied for every time step, but potentially for some. Low values in $J(k)$ correspond with low differences between states and references, while high values correspond with big differences. The key word is correspond, as lower values can also be achieved by few changes in the inputs, [5].

Changing the weights leads to a different solution and thus to different controller–plant behavior. The choice of the correct values for $\tilde{\mathbf{Q}}(w)$ and $\tilde{\mathbf{R}}(w)$ is important. However, only the ratio between the weights is important and not the magnitude, [5]. Finding a satisfying ratio for these weighting matrices, as they are defined below in (2-68) and (2-69) is at the core of this thesis. The variation of the weights is reformulated into a multiobjective problem which is solved by an evolutionary algorithm (EA). The exact implementation of which is covered in the next chapter.

To find the optimal input sequence, that leads to the minimal $J(k)$ additional steps need to be made. Let the reference trajectory be defined as

$$\mathbf{\Xi}(k) = \begin{bmatrix} \mathbf{r}_{k+1} \\ \vdots \\ \mathbf{r}_{k+\check{H}_p} \end{bmatrix}\,. \tag{2-60}$$

The tracking error $\mathbf{E}$, as the difference between reference trajectory and future states is written for $\mathbf{\Delta U}(k) = \mathbf{0}$ as

$$\mathbf{E}(k) = \mathbf{\Xi}(k) - \mathbf{\Psi} x_k - \mathbf{\Upsilon} u_{k-1}\,. \tag{2-61}$$

In the following the (k) will be disregarded due to readability. The MPC cost function is rewritten as

$$\begin{aligned} J(k) = & \quad \| \mathbf{\Theta\Delta U} - \mathbf{E} \|^2_Q + \| \mathbf{\Delta U} \|^2_R\,, && \text{(2-62)}\\ = & \quad [\mathbf{\Delta U}'\mathbf{\Theta}' - \mathbf{E}']\mathbf{Q}[\mathbf{\Theta\Delta U} - \mathbf{E}] + \mathbf{\Delta U}'\mathbf{R}\mathbf{\Delta U}\,, && \text{(2-63)}\\ = & \, \mathbf{E}'\mathbf{Q}\mathbf{E} - 2\mathbf{\Delta U}'\mathbf{\Theta}'\mathbf{Q}\mathbf{E} + \mathbf{\Delta U}'[\mathbf{\Theta}'\mathbf{Q}\mathbf{\Theta} + \mathbf{R}]\mathbf{\Delta U}\,, && \text{(2-64)}\\ = & \quad const. - \mathbf{\Delta U}'\mathbf{G} + \mathbf{\Delta U}'\mathbf{H}\mathbf{\Delta U}\,, && \text{(2-65)} \end{aligned}$$

where

$$\mathbf{G} = 2\boldsymbol{\Theta}'\mathbf{Q}\mathbf{E}\,, \tag{2-66}$$

$$\mathbf{H} = \boldsymbol{\Theta}'\mathbf{Q}\boldsymbol{\Theta} + \mathbf{R}\,, \tag{2-67}$$

$$\mathbf{Q} = \begin{bmatrix} \tilde{\mathbf{Q}}_1 & \dots & 0 \\ \vdots & \ddots & \vdots \\ 0 & \dots & \tilde{\mathbf{Q}}_{\check{H}_p} \end{bmatrix} \in \mathbb{R}^{\check{n}\check{H}_p \times \check{n}\check{H}_p}\,, \tag{2-68}$$

$$\mathbf{R} = \begin{bmatrix} \tilde{\mathbf{R}}_1 & \dots & 0 \\ \vdots & \ddots & \vdots \\ 0 & \dots & \tilde{\mathbf{R}}_{\check{H}_u} \end{bmatrix} \in \mathbb{R}^{\check{n}\check{H}_u \times \check{n}\check{H}_u}\,. \tag{2-69}$$

Since $J(k)$ is a quadratic function, the minimum is reached when its partial derivative with respect to $\boldsymbol{\Delta}\mathbf{U}$ equals zero

$$\frac{\partial J}{\partial \boldsymbol{\Delta}\mathbf{U}} = -\mathbf{G} + 2\mathbf{H}\boldsymbol{\Delta}\mathbf{U} = \mathbf{0}\,. \tag{2-70}$$

Thus the optimal input sequence $\boldsymbol{\Delta}\mathbf{U}_{\mathbf{opt}}$, that minimizes $J(k)$, can be calculated by the Moore-Penrose pseudo inverse to reach the least square solution, [5]

$$\boldsymbol{\Delta}\mathbf{U}_{\mathbf{opt}} = \frac{1}{2}\left(\mathbf{H}'\mathbf{H}\right)^{-1}\mathbf{H}'\mathbf{G}\,. \tag{2-71}$$

Some models have additional measured disturbances $\mathbf{d}$ to the plant. The prediction for the measured disturbances can be included into the problem formulation, making them part of the least square solution. The controller is therefore capable of compensating the disturbances ahead of time, as opposed to just responding to them. For this case, the discrete state space model is described by, [5]

$$\mathbf{x}_{k+1} = \mathbf{A}\mathbf{x}_k + \mathbf{B}\mathbf{u}_k + \mathbf{B}_\mathbf{d}\mathbf{d}_k\,. \tag{2-72}$$

With $\mathbf{d} \in \mathbb{R}^{\check{l}}$ as the disturbance vector with $\check{l}$ disturbances, and $\mathbf{B}_\mathbf{d} \in \mathbb{R}^{\check{n}\times\check{l}}$ being the gain matrix of the disturbances onto the model. The matrices $\mathbf{B}$ and $\mathbf{B}_\mathbf{d}$ and the input vectors $\mathbf{u}$ and $\mathbf{d}$ are summarized to

$$\mathbf{B}_\mathbf{t} = \begin{bmatrix} \mathbf{B} & \mathbf{B}_\mathbf{d} \end{bmatrix} \qquad \mathbf{B}_\mathbf{t} \in \mathbb{R}^{\check{n}\times(\check{p}+\check{l})}\,, \tag{2-73}$$

$$\mathbf{u}_\mathbf{t} = \begin{bmatrix} \mathbf{u} & \mathbf{d} \end{bmatrix} \qquad \mathbf{u}_\mathbf{t} \in \mathbb{R}^{\check{p}+\check{l}}\,. \tag{2-74}$$

To merge this new description with the MPC cost function the state sequence is redefined as

$$\mathbf{X}(k) = \boldsymbol{\Psi}x_k + \boldsymbol{\Upsilon}u_{k-1} + \boldsymbol{\Theta}\boldsymbol{\Delta}\mathbf{U}(k) + \boldsymbol{\Gamma}\mathbf{D}(k)\,, \tag{2-75}$$

with

$$\mathbf{D}(k) = \begin{bmatrix} \mathbf{d}_k \\ \mathbf{d}_{k+1} \\ \vdots \\ \mathbf{d}_{k+\check{H}_p-1)} \end{bmatrix}, \tag{2-76}$$

$$\mathbf{\Gamma} = \begin{bmatrix} \mathbf{B_d} & 0 & 0 & \dots & 0 \\ \mathbf{AB_d} & \mathbf{B_d} & 0 & \dots & 0 \\ \mathbf{A^2B_d} & \mathbf{AB_d} & \mathbf{B_d} & \dots & 0 \\ \vdots & \vdots & \vdots & \ddots & \vdots \\ \mathbf{A}^{\check{H}_p-1}\mathbf{B_d} & \mathbf{A}^{\check{H}_p-2}\mathbf{B_d} & \mathbf{A}^{\check{H}_p-3}\mathbf{B_d} & \dots & \mathbf{B_d} \end{bmatrix}. \tag{2-77}$$

The tracking error then is given by

$$\mathbf{E}(k) = \mathbf{\Xi}(k) - \mathbf{\Psi}x_k - \mathbf{\Upsilon}u_{k-1} - \mathbf{\Gamma D}(k)\,. \tag{2-78}$$

Now as before, equations (2-62) to (2-71) apply and the system of linear equations can be solved to find the optimal input sequence, [5].

2-2-4 Numerical Stable Least Square Solution of the Model Predictive Control Problem

According to [5], equation (2-62) is not the best way of calculating the optimal input-sequence, because $\mathbf{\Theta}$ is most likely to be ill-conditioned. Let there be the two matrices $\mathbf{S_Q}$ and $\mathbf{S_R}$ such that

$$\mathbf{S'_Q S_Q} = \mathbf{Q}\,, \quad \text{and} \quad \mathbf{S'_R S_R} = \mathbf{R}\,. \tag{2-79}$$

The matrices $\mathbf{S_Q}$ and $\mathbf{S_R}$ are straight forward to calculate for a diagonal matrix, by taking the square-root of each entry on the diagonal. For non diagonal matrices the Cholesky algorithm can be applied. The cost function is reformulated as, [5]

$$J(k) = \left\| \begin{bmatrix} \mathbf{S_Q X} - \mathbf{\Xi} \\ \mathbf{S_R \Delta U} \end{bmatrix} \right\|^2. \tag{2-80}$$

The least squares formulation of the minimization problem becomes, [5]

$$\begin{bmatrix} \mathbf{S_Q \Theta} \\ \mathbf{S_R} \end{bmatrix} \mathbf{\Delta U} = \begin{bmatrix} \mathbf{S_Q E} \\ \mathbf{0} \end{bmatrix}. \tag{2-81}$$

Its least square solution becomes, using MATLAB-notation

$$\mathbf{\Delta U_{opt}} = \begin{bmatrix} \mathbf{S_Q \Theta} \\ \mathbf{S_R} \end{bmatrix} \backslash \begin{bmatrix} \mathbf{S_Q E} \\ \mathbf{0} \end{bmatrix}. \tag{2-82}$$

Since the MPC is a linear time-invariant system the solution of (2-82) can be calculated in advance if the tracking-error $\mathbf{E}$ is set to 1 for all times as, [5]

$$\mathbf{K_{MPC}} = \begin{bmatrix} \mathbf{S_Q\Theta} \\ \mathbf{S_R} \end{bmatrix} \setminus \begin{bmatrix} \mathbf{S_Q E} \\ \mathbf{0} \end{bmatrix} . \tag{2-83}$$

The optimal input can thus be calculated with the matrix $\mathbf{K_{MPC}}$ by a simple matrix multiplication with the actual tracking error $\mathbf{E}$, once $\mathbf{K_{MPC}}$ is pre-calculated. This is done by, [5]

$$\mathbf{\Delta U_{opt}} = \mathbf{K_{MPC}E} . \tag{2-84}$$

2-2-5 Linear State Signal Shaping Model Predictive Control

In some control cases, it can be less important that the states of the system exactly follow a given reference, but that the states follow the shape of a certain function, [6]. In an electrical system with THD, voltage and current signal don't follow an exact sine wave in their shape. The controller goal is to find an input sequence to the system that transforms the distorted signal into a smooth sine function.

A method to achieve this goal was conceived by, [14], and subsequently pubilished in, [6].[4] State deviations from the signal shape class of sinus are punished by the MPC cost function. This is achieved by modification of the weighting matrix $\mathbf{Q}$. The minimum of the cost function $J(k)$ is reached only, when the states agrees with the signal shape defined in the weighting matrix. The rest of this subsection will cover the theory of formulating the shape class of a sinusoid into the weighting matrix $\mathbf{Q}$.

The shape of a function can be described by differential, or difference equations. The homogeneous ordinary second order differential equation described by

$$\frac{\mathrm{d}x(t)}{\mathrm{d}t^2} + \omega^2 x(t) = 0 , \tag{2-85}$$

where $\omega = 2\pi f$ is solved by the sine function shown by

$$\frac{\mathrm{d}\sin(\omega t)}{\mathrm{d}t^2} + \omega^2 \sin(\omega t) , \tag{2-86}$$

$$= -\omega^2 \sin(\omega t) + \omega^2 \sin(\omega t) . \tag{2-87}$$

In discrete time, the difference equation has a similar structure

$$\ddot{x}_k + \omega^2 x_k = 0 , \tag{2-88}$$

[4] Paper was accepted, but is presently unpublished.

where $\ddot{x}_k$ is the second derivative in discrete time. The second derivative can be approximated by forward differentiation as

$$\ddot{x}_k \approx \frac{2x_k - 5x_{k+1} + 4x_{k+2} - x_{+3}}{t_s^2}\,. \tag{2-89}$$

The difference equation (2-88) can thus be expressed as

$$\frac{1}{t_s^2}\left[\left(2 + \omega^2 t_s^2\right) x_k - 5x_{k+1} + 4x_{k+2} - 1x_{k+3}\right] = 0\,. \tag{2-90}$$

This equation is divided into two parts. Its sinusoidal linear shape class vector $\mathbf{V_s}$, and its state sequence $\mathbf{X}(k)$, as

$$\mathbf{V_s} = \frac{1}{t_s^2}\begin{bmatrix} 2 + \omega^2 t_s^2 & -5 & 4 & -1 \end{bmatrix}, \tag{2-91}$$

$$\mathbf{X}(k) = \begin{bmatrix} x_k \\ x_{k+1} \\ x_{k+2} \\ x_{k+3} \end{bmatrix}, \tag{2-92}$$

$$\mathbf{V_s}\mathbf{X_s}(k) = 0\,. \tag{2-93}$$

The exact definition of a linear shape class of a discrete–time vector $\mathbf{V}$ is given below, [6].

Definition 2-2.1 (Linear Shape Class Matrix $\mathbf{V}$, [6])**.**
The set

$$\mathscr{X}_{\mathbf{V}} = \left\{ \mathbf{x}_1, \mathbf{x}_2, \ldots \,|\mathbf{V} \begin{pmatrix} \mathbf{x}_{k+1} \\ \vdots \\ \mathbf{x}_{k+\check{T}} \end{pmatrix} = \mathbf{0} \qquad \forall k = 0, 1, \ldots \right\}, \tag{2-94}$$

is called a linear shape class of a discrete–time vector signal defined by the matrix $\mathbf{V} \in \mathbb{R}^{\check{z} \times \check{n}_u \check{T}}$.

The variable $\check{T}$ stands for the number of time steps applied to the shape class. The number of states is $\check{n}_u$, and $\check{z}$ is the number of shape class equations used.

In the above example, the vector $\mathbf{V_s}$ is of the nature $\check{T} = 4$, $\check{z} = 1$, and $\check{n}_u = 1$. Equation (2-92) equals zero, when the vector $\mathbf{X}(k)$ follows any sine wave that develops with ω. As the deviation from the sine wave increase, so does the difference from zero. The multiplication serves as numerical assessment on how sinusoidal a given signal $\mathbf{X}(k)$ is, with respect to the frequency f .

The same shape class $\mathbf{V_s}$ can be used to evaluate a state sequence of more than four time step. Every individual time step is tested separately. If the state vector ranges

from k to the prediction horizon $\check{H}_p$, the first multiplication tests the state vector from k to $k+3$. The second multiplication tests the steps from $k+1$ to $k+5$. This is continued until the states $\check{H}_p - 3$ to $\check{H}_p$ are reached.

The same result is achieved by a single matrix–vector multiplication $\mathbf{P_V X}(k)$, when $\mathbf{V}$ is used to create a matrix $\mathbf{P_V}$ according to the following definition.

Definition 2-2.2 (Band matrix $\mathbf{P_V}$, [6])**.**
For any integer $\check{H}_p \geq \check{T}$, let $\mathbf{V}_y = \mathbf{V}_{:,(y-1)\check{n}_u+1:y\check{n}_u}$, the band matrix

$$\mathbf{P_V} = \begin{bmatrix} \mathbf{V}_1 & \mathbf{V}_2 & \dots & \mathbf{V}_{\check{T}} & \mathbf{0} & \dots & \mathbf{0} \\ \mathbf{0} & \mathbf{V}_1 & \mathbf{V}_2 & \dots & \mathbf{V}_{\check{T}} & \ddots & \vdots \\ \vdots & \ddots & \ddots & \ddots & \ddots & \ddots & \mathbf{0} \\ \mathbf{0} & \dots & \mathbf{0} & \mathbf{V}_1 & \mathbf{V}_2 & \dots & \mathbf{V}_{\check{T}} \end{bmatrix} \in \mathbb{R}^{\check{p}_1 \times \check{p}_2}, \tag{2-95}$$

with $\check{p}_1 = \check{z}(\check{H}_p - \check{T} + 1)$ and $\check{p}_2 = \check{n}_u \check{H}_p$, can be computed by shifting the shape class matrix $\mathbf{V}$ for integer multiples of $\check{n}_u$ columns with the help of matrices of zeros $\mathbf{0} = \{0\}^{\check{z} \times \check{n}_u}$.

The evaluation of the state sequence by $\mathbf{P_V}$, can result in positive and negative deviations from zero. The sign of the deviation is less important then the magnitude. Squaring the result eliminates the sign. The same is achieved by computing the multiplication $\mathbf{P_V X}(k)$ twice. This can be written as $\mathbf{X}'(k)\mathbf{P}'_\mathbf{V}\mathbf{P_V X}(k)$. Using equation (2-59) it can be transformed into $\| \mathbf{X}(k) \|^2_{\mathbf{P}'_\mathbf{V}\mathbf{P_V}}$. With a reference trajectory, in the MPC cost function of $\mathbf{\Xi} = \mathbf{0}$, the same structure is observed,

$$J(k) = \| \mathbf{X}(k) - \mathbf{\Xi}(k) \|^2_\mathbf{Q} + \| \Delta\mathbf{U}(k) \|^2_\mathbf{R}, \tag{2-96}$$

$$= \| \mathbf{X}(k) \|^2_{\mathbf{P}'_\mathbf{V}\mathbf{P_V}} + \| \Delta\mathbf{U}(k) \|^2_\mathbf{R} . \tag{2-97}$$

The band matrix has the property $\mathbf{P}'_\mathbf{V}\mathbf{P_V} = \mathbf{Q}$. It can thus be used to calculate the matrix $\mathbf{S_Q}$ from equation (2-79) for a shape class. The reference trajectory has to equal zero in that case, [6]. As a note, linear shape class MPC and the classical reference MPC can be implemented in the same cost function $J(k)$.

The example above uses one state system. A second state is introduced thus ($\check{n}_u = 2$). If only the first is to be controlled by the shape class, the shape class vector has to be

altered accordingly.

$$\mathbf{V_s} = \frac{1}{t_s^2}\begin{bmatrix} 2+\omega^2 t_s^2 & 0 & -5 & 0 & 4 & 0 & -1 & 0 \end{bmatrix}, \tag{2-98}$$

$$\mathbf{X}(k) = \begin{bmatrix} x_{1,k} \\ x_{2,k} \\ x_{1,k+1} \\ x_{2,k+1} \\ x_{1,k+2} \\ x_{2,k+2} \\ x_{1,k+3} \\ x_{2,k+3} \end{bmatrix}. \tag{2-99}$$

If both states should be assessed by the shape class, then $\mathbf{V_s}$ needs to be adjusted with a second equation ($\check{z} = 2$) to

$$\mathbf{V_s} = \frac{1}{t_s^2}\begin{bmatrix} 2+\omega^2 t_s^2 & 0 & -5 & 0 & 4 & 0 & -1 & 0 \\ 0 & 2+\omega^2 t_s^2 & 0 & -5 & 0 & 4 & 0 & -1 \end{bmatrix}. \tag{2-100}$$

For evaluating a longer state sequence, the band matrix is build according to definition 2-2.2. This way of calculating is however not ideal when the MPC controller should be tuned. As discussed in subsection 2-2-3, the tuning is done by altering the weighting in the matrices $\mathbf{S_Q}$ and $\mathbf{S_R}$. The computational implication is, that the matrix $\mathbf{V_s}$ has to be modified first to calculate the band matrix, for every different setting tested. Considering, that this weighted band matrix is created some thousand times during the multiobjective optimization, a method that allows precalculation is needed to be more time efficient.

For a system with $\check{n}$ states, a total number of band matrices should be created in such a way, that they can be multiplied with a factor, before they are added together, to form a matrix $\mathbf{S_Q}$. The matrix is then used in the MPC cost function. This can be achieved, by using the Kronecker product. First a sinusoidal band matrix for one state is created using $\mathbf{V_s}$ with $\check{T} = 4$, $\check{n}_u = 1$, and $\check{z} = 1$. The Kronecker product is applied with a matrix $\mathbf{H}_{n_c} \in \mathbb{R}^{(\check{n}_x \times \check{n})}$, as shown in

$$\mathbf{P_v} \otimes \mathbf{H}_{n_c} = \mathbf{S}_{\mathbf{Q},n_c} \in \mathbb{R}^{\check{p}_3 \times \check{p}_4}, \tag{2-101}$$

where $\check{p}_3 = \check{n}_x(\check{H}_p - \check{T} + 1)$ and $\check{p}_2 = \check{n}\check{H}_p$. The matrix $\mathbf{H}_{n_c}$ has all entries to zero, except for row n_c, column n_c. The variable $\check{n}$ referrers to the number of states in the system matrix $\mathbf{A}$ of a state space model. The variable $\check{n}_x$ is last state of the system, that is targeted by some form of weights independent of shape class or conventional reference control, and is counted from $n \in \{1, \ldots, \check{n}_x\}$. The index n_c specifies the current state, for which the weighting matrix $\mathbf{S}_{\mathbf{Q},n_c}$ is created, allowing an unambiguous nomenclature, to which state the weighting matrix belongs. The index n_c can range from $\{1, \ldots, \check{n}_x\}$.

Note, that the numbers of rows in $\mathbf{S_Q}_{,n_c}$ is actually dependent on $\check{n}_x$. During the construction of the system matrix $\mathbf{A}$, states which are not intended to be controlled should be located at the end of the system, because the computation time needed for the least square solution as in equation (2-83) is highly dependent on the size of $\mathbf{S_Q}$. To create the weighted matrix $\mathbf{S_Q}$, the sub matrices $\mathbf{S_Q}_{,n_c}$ are multiplied by a weighting factor and then added.

The following example is intended to clarify what is described above. Given a state space system with $\check{n} = 7$, where two states, state 2 and state 3 should be controlled. It follows that $\check{n}_x = 3$.[5] The prediction Horizon has a length of $\check{H}_p = 200$. Using the sinusoidal shape class vector from (2-91), the band matrix is of size $\mathbf{P_V} \in \mathbb{R}^{(197\times200)}$. The $\mathbf{H}_{n_c}$–matrices involved in the Kronecker product are $\mathbf{H}_2, \mathbf{H}_3 \in \mathbb{R}^{(3\times7)}$. The two sub weighting matrices $\mathbf{S_Q}_{,2}$ and $\mathbf{S_Q}_{,3}$ are calculated by

$$\mathbf{P_V} \otimes \mathbf{H}_2 = \mathbf{S_Q}_{,2} \in \mathbb{R}^{(591\times1400)}\,, \tag{2-102}$$

$$\mathbf{P_V} \otimes \mathbf{H}_3 = \mathbf{S_Q}_{,3} \in \mathbb{R}^{(591\times1400)}\,. \tag{2-103}$$

Then the overall matrix $\mathbf{S_Q}$ follows by multiplying the sub matrices by a weighting factor f_{n_c} and adding them together, shown in

$$f_2\,\mathbf{S_Q}_{,2} + f_3\,\mathbf{S_Q}_{,3} = \mathbf{S_Q} \in \mathbb{R}^{(591\times1400)}\,. \tag{2-104}$$

The indices of weighting factors f_2 and f_3 correspond with the state n_c that is controlled by a sub weighting matrix. Reorganization the states of the system matrix $\mathbf{A}$ leads to a smaller matrix $\mathbf{S_Q}$, because $\check{n}_x = 2$ is smaller than before. The calculation of $\mathbf{S_Q}$ is done by

$$\mathbf{P_V} \otimes \mathbf{H}_1 = \mathbf{S_Q}_{,1} \in \mathbb{R}^{(394\times1400)}\,, \tag{2-105}$$

$$\mathbf{P_V} \otimes \mathbf{H}_2 = \mathbf{S_Q}_{,2} \in \mathbb{R}^{(394\times1400)}\,, \tag{2-106}$$

$$f_1\,\mathbf{S_Q}_{,1} + f_2\,\mathbf{S_Q}_{,2} = \mathbf{S_Q} \in \mathbb{R}^{(394\times1400)}\,. \tag{2-107}$$

The weighting factors of the sub weighting matrices are the decision variables in the multiobjective controller tuning. This concludes section 2-2 about the control theory used in this thesis. In the next section the general aspects of multiobjective optimization are discussed.

[5] The recommendation above, on how to construct $\mathbf{A}$ is not followed on purpose.

2-3 Multiobjective Optimization

This section covers the background on multiobjective optimization that is required for this thesis. The first subsection covers the multiobjective problem (MOP) statement, and is followed by the subsection on the concept of Pareto optimality. Next the benefit solving a MOP by heuristic methods is discussed. The last two subsection introduce the visualization method level diagrams, and provide the information on the average direction vector (ADV) comparison method, which will be used to assess reproducibility of the spMODEx algorithm.

2-3-1 Multiobjective Problem Statement

Given a collection of cost functions $\mathbf{J}(\zeta)$ with a number of $m \in \{1, \ldots, \check{m}\}$ elements, a MOP can be stated, without loss of generality[6], as

$$\min_{\zeta} \mathbf{J}(\zeta) = \min_{\zeta} \left[J_1(\zeta), \ldots, J_{\check{m}}(\zeta) \right] , \tag{2-108}$$

subject to

$$\mathbf{g}(\zeta) \leq \mathbf{0} , \tag{2-109}$$
$$\mathbf{h}(\zeta) = \mathbf{0} , \tag{2-110}$$

with $\zeta \in \mathbf{O} \subseteq \mathbb{R}^{\check{j}}$ as the vector of decision variables from $j \in \{1, \ldots, \check{m}\}$, searching the space $\mathbf{O}$, the objective function vector as $\mathbf{J}(\zeta) \in \wedge \subseteq \mathbb{R}^{\check{m}}$, and $\mathbf{g}(\zeta)$, $\mathbf{h}(\zeta)$ as the inequality and equality constraints, [2].

There are two approaches how a MOP can be minimized. The first is know as an aggregate objective function (AOF). An overall cost function is created from the individual cost-functions and the aggregate is minimized. For example by summing the m sub cost function as

$$\min_{\zeta} \mathbf{J}(\zeta) = \min_{\zeta} \sum_{m=1}^{\check{m}} J_m(\zeta) . \tag{2-111}$$

This is the approach which is taken for the solution of the optimal input sequence of the MPC cost function given in equation (2-62). The first cost is $J_1(\boldsymbol{\Delta}\mathbf{U}) = \| \boldsymbol{\Theta}\boldsymbol{\Delta}\mathbf{U} - \mathbf{E} \|^2_{\mathbf{Q}}$ and the second is $J_2(\boldsymbol{\Delta}\mathbf{U}) = \| \boldsymbol{\Delta}\mathbf{U} \|^2_{\mathbf{R}}$. The aggregated function is minimized via the least square solution.

[6] A maximization problem can be reformulated into a minimization by the following relationship: $\max J_m(\zeta) = -\min(-J_m(\zeta))$, where index m stands for a specific cost function.

The second approach to minimize a MOP is known as generate first choose later (GFCL). Instead of minimizing an AOF multiple solutions are generated and the choice is postponed to a later point in time. The following thought experiment should serve as an example.

The journey from Hamburg, Germany, to Berlin is roughly 300km. Neglecting traffic jams, etc., a MOP can be formulated as

$$\min_{v_e, G_e} \mathbf{J}(v_e, G_e) = [J_{fuel}(v_e, G_e), J_{time}(v_e)] \ ,$$

with $J_{fuel}(v_e, G_e)$ as the fuel consumption cost of the car in L, $J_{time}(v_e)$ as the travel time in h. The velocity v_e is measured in $\frac{\text{km}}{\text{h}}$ and $G_e \in \{1, 2 \ldots, 6\}$ is the gear with which the car drives. Different combinations for G_e and v_e are tested. The result is shown in

$$\mathbf{J}(200, 6) = [75, 1.5] \ , \ \mathbf{J}(100, 6) = [8, 3] \ , \ \mathbf{J}(30, 1) = [150, 10] \ .$$

Analyzing the results there is no way in discerning which of the first two solution is the best. The decision maker (DM) could reformulate the problem in an overall cost by introducing a gasoline price and a salary to convert everything into €, but that is beside the point. What can be decide without additional information is, that driving slowly in the first gear is worse than the first solution, as fuel consumption and travel time are both higher than in comparison with the first two solutions. Therefor the third solution can be discarded. The idea that the first two solutions are equally valid is know as Pareto optimality. The set of all such very often infinite solutions is known as the Pareto Front (PF), and will be focus in the next subsection, [2].

2-3-2 Pareto Optimality

This subsection mathematically defines what Pareto optimality is, and lays out the associated ideas. An important note on indexing. In this chapter variables are introduced with an upper index, such as ζ^i. The index i is not to be understood as a power, but as a counter for the number of individuals in a population of vectors.

Recalling the minimization problem from (2-108), there is a set of solutions, the Pareto set $\mathbf{K_P}$ where each vector of the decision variable $\zeta \in \mathbf{K_P}$ defines an objective vector $\mathbf{J}(\zeta)$. The PF is the complete set of all possible solutions in the search space $\mathbf{O}$, which are Pareto optimal or non–dominated, [2].

Definition 2-3.1 (Pareto Dominance, [2])**.** A decision vector ζ^1 dominates another vector ζ^2, denoted as $\zeta^1 \preceq \zeta^2$, if $\mathbf{J}(\zeta^1)$ is not worse than $\mathbf{J}(\zeta^2)$ in all objectives, and is better in at least one objective.

$$\forall u \in A := [1, \ldots, \check{m}] \, , \mathbf{J}_u(\zeta^1) \leq \mathbf{J}_u(\zeta^2) \wedge \exists \, u \in A : \mathbf{J}_u(\zeta^1) < \mathbf{J}_u(\zeta^2) \, .$$

Definition 2-3.2 (Strict Dominance, [2])**.** A decision vector ζ^1 is strictly dominated by another vector ζ^2 if $\mathbf{J}(\zeta^1)$ is worse than $\mathbf{J}(\zeta^2)$ in all objectives.

Definition 2-3.3 (Weak Dominance, [2])**.** A decision vector ζ^1 weakly dominates another vector ζ^2 if $\mathbf{J}(\zeta^1)$ is **not** worse than $\mathbf{J}(\zeta^2)$ in all objectives.

Definition 2-3.4 (Pareto optimal, [2])**.** A solution vector ζ^* is Pareto optimal if

$$\nexists \zeta \in \mathbf{O} : \zeta \preceq \zeta^*.$$

Definition 2-3.5 (Pareto Set, [2])**.** In a MOP, the Pareto Set $\mathbf{K_P}$ is the set including all the Pareto optimal solutions:

$$\mathbf{K_P} := \{\zeta \in \mathbf{O} | \nexists \zeta' \in \mathbf{O} : \zeta' \preceq \zeta\} \ . \tag{2-112}$$

Definition 2-3.6 (Pareto Front, [2])**.** In a MOP, the Pareto Front $\mathbf{J_P}$ is the set including the objective vectors of all Pareto optimal solutions:

$$\mathbf{J_P} := \{\mathbf{J}(\zeta) : \zeta \in \mathbf{K_P}\} \ .$$

The solution to a MOP can thus be defined by the two matrices

$$\mathbf{K}_\mathbf{P}^* \in \mathbb{R}^{\check{g} \times \check{j}} \ , \tag{2-113}$$

$$\mathbf{J}_\mathbf{P}^* \in \mathbb{R}^{\check{g} \times \check{m}} \ . \tag{2-114}$$

The matrix $\mathbf{K}_\mathbf{P}^*$ contains the decision variables ζ_j, where $j \in \left\{1, \ldots, \check{j}\right\}$ are the individual decision variables, and $g \in \langle 1, \ldots, \check{g}\}$ is the number of individual solutions. The matrix $\mathbf{J}_\mathbf{P}^*$ contains the corresponding values of the cost functions, where $m \in \{1, \ldots, \check{m}\}$ are the number of sub cost functions that were used in the MOP statement from equation (2-108). The star * indicates, that the matrices are approximations of the real PF, as the real PF is unknown.

2-3-3 Heuristic Solution Methods

Singleobjective problems and MOPs can generally fall into two different classes. These are convex and non–convex optimization problems. In convex optimization problems only one minimum exists. The solution is found with numerical algorithms, which exploit continuously decreasing gradient of the problem. This is however not the same for non–convex problems, where the solution space is multimodal containing several local minima.

With the comparatively recent increase in computing power new methods for the solution of non–convex problems are applied. They are known as heuristic methods or

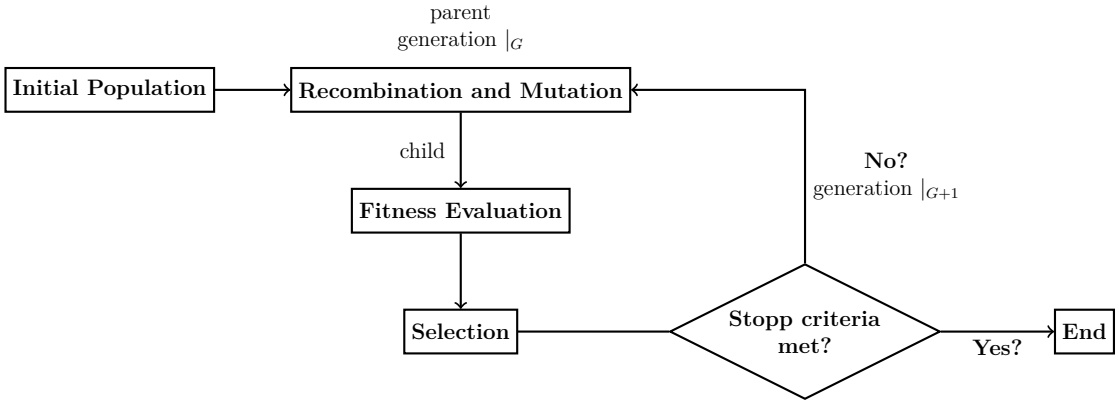

Figure 2-4: Generalized schematic of an evolutionary algorithm, [1].

evolutionary algorithm, and solve optimization problems by applying brute computing force with an underlying heuristic, to solve them in reasonable time. Heuristic methods are not superior in convex traditional approaches. However, due to there simplicity of approach, robust response to changing circumstances, easy parallelization, and flexibility EAs have gained a wide array of application in recent years, especially in non–convex optimizoation, [1].

The paradigm of EAs is grounded in the Theory of Evolution which was proposed by Charles Darwin and published in *On the Origin of Species* (1859). EAs generally follow four stages: Initialization of the Population, Recombination and Mutation, Fitness Evaluation, and Selection. A graphical display is given in figure 2-4, [1]. Given a optimization problem as shown in equations (2-108) to (2-110), an Initial Population of test vectors $\zeta_{\check{j}}^{\check{i}}$ is created, where the number of individuals is $\check{i}$ and the number of decision variables is $\check{j}$. The initialization can be done by assigning random numbers to the decision variables. In the same phase, the individuals are evaluated using the objective cost functions. These test vectors are also referred to as 'parents' in the 'parent generation', [1].

In the recombination and mutation phase, the population of $\check{i}$ individuals in generation $|_G$ is modified with a heuristic mechanism. The difference in modification is one of the major aspect by which EAs differ. As a simple example, some decision–variables of two individuals $\zeta_j^1|_G$ and $\zeta_j^2|_G$, can be exchanged, to create a new individual ζ_j^3. The total number of decision variables is given by $\check{j}$, and $j \in \left\{1, \ldots, \check{j}\right\}$. The decision variables are then mutated by a small amount ε_j to allow an exploration of the search space. A new test–vector $(\zeta_j^3 - \varepsilon_j)|_{G+1}$ is created for the new generation $|_{G+1}$. The illustrated process is a rudimentary form of a genetic algorithm.[7] Newly found individuals are also referred to as 'children' or 'child generation', [1].

[7]Named this way, because the recombination and mutation method work analogous to the recom-

In the fitness evaluation phase, individuals are assessed using the objective cost function function of the MOP. In the Selection phase the best individuals are chosen to carry over as parents into the next generation. Different Selection-mechanism exist. For example selecting the best 10 individuals from the child generation only. Or taking the best individuals from child and parent generation combined. Best means here as Pareto optimality. Some methods make additionally use of an external archive that stores all Pareto optimal solutions found. The population, which is fixed in size can develop in a different direction without loss of information, [1].

There is a multitude of different EA to solve different kinds of optimization problems. To name a few, these are: Simulated Annealing, Tabu Search, Ant Colony Algorithm, Particle Swarm Optimization and Differential Evolution (DE), [1]. Artificial Neural Networks can also be used to solve optimization problems. They work however in a different way as the algorithms mentioned above, making sense of complex data more analogues to how the brain processes data. Neural Networks have to be trained on massive data sets prior to use. A once trained network finds its solution to a MOP more or less instantaneous, [15].

An overview over heuristic solution methods for MOPs was given. The next subsections will introduce a method that is used to visualize multidimensional data.

2-3-4 Visualizing Multidimensional Data Sets with Level Diagrams

The solution of the multiobjective problem results in the PF approximation as the two matrices $\mathbf{K}_\mathbf{P}^*$ and $\mathbf{J}_\mathbf{P}^*$ [see (2-113),(2-114)]. Data sets where $\mathbf{J}_\mathbf{P}^*$ has dimensions $\check{m} \in \{1, 2, 3\}$ are easily visualized with standard methods. The tasks becomes more difficult with increasing dimension. Methods have been developed to visualize data sets of higher dimension. Scatter diagrams for example, create a plot for every possible combination of the sub cost functions, needing a total number of $\frac{\check{m}(\check{m}-1)}{2}$ graphs. A method that display the whole information in one graph is the parallel coordinate chart. The visualization is done by plotting $\check{m}$ vertical axis on a horizontal line, and connecting the specific values of each solution by a straight lines. This has the drawback, that with increasing number of solutions $\check{g}$, the diagrams become crowed and confusing, [16].

A different method was reported by [17] known as level diagrams. One plot for every cost function is created, where the individual solutions a plotted against their normalized distance with respect to an ideal point. The ideal point is defined as, [17]

$$\mathbf{J}^{\mathbf{ideal}} = \left[\min J_1(\zeta^i), \ldots, \min J_{\check{m}}(\zeta^i)\right] \forall \mathbf{J}(\zeta^i) \in \mathbf{J_P}^* \,. \tag{2-115}$$

bination of DNA in living organisms. Decision variable vectors are therefore also referred to as the genetic make–up of an individual.

It is the imaginary point that results from taking the minimal value of each sub cost function found in $\mathbf{J}^*_{\mathbf{P}}$. To do the comparison the individual solutions are first classified between zero and one. To apply the method the normalized distance with respect to the minimum and maximum values found in each cost functions of the PF approximation is calculated.

For a solution $\mathbf{J}^*_{\mathbf{P}} \in \mathbb{R}^{\check{g}\times\check{m}}$ the maximum values of each sub cost function are

$$\bar{\iota}_m^{max} = \max \mathbf{J}^*_{\mathbf{P},g,m}\,, \qquad \forall g\,, \forall m\,, \tag{2-116}$$

where $m \in \{1,\ldots,\check{m}\}$ and $g \in \{1,\ldots,\check{g}\}$. The minimum values of the sub cost functions are found by

$$\bar{\iota}_m^{min} = \min \mathbf{J}^*_{\mathbf{P},g,m}\,, \qquad \forall g\,, \forall m\,, \tag{2-117}$$

where $m \in \{1,\ldots,\check{m}\}$ and $g \in \{1,\ldots,\check{g}\}$. The individual solutions from $\mathbf{J}^*_{\mathbf{P},g,m}$ are normalized by applying

$$\bar{\mathbf{J}}^*_{\mathbf{P},g,m} = \frac{\mathbf{J}^*_{\mathbf{P},g,m} - \bar{\iota}_m^{min}}{\bar{\iota}_m^{max} - \bar{\iota}_m^{min}}\,, \qquad \forall g\,, \forall m\,. \tag{2-118}$$

The distance from the ideal point is calculated via applying a norm. In this thesis the Euclidean norm was used. The calculation is done by

$$\parallel \iota_g \parallel_2 = \sqrt{\sum_{m=1}^{\check{m}} (\bar{\mathbf{J}}^*_{\mathbf{P},g,m})^2} \qquad \forall g\,. \tag{2-119}$$

The normalized length of every individual solution g can vary between $0 \leq \parallel \iota_g \parallel_2 \leq \sqrt{\check{m}}$. A level diagram is plotted, with the sub cost function J_m on the x–axis, and the normalized distance $\parallel \iota_g \parallel_2$ on the y–axis. This can also be applied to the decision variables, but wasn't done in this thesis. Each individual solutio is found at the same height or level in all $\check{m}$ plots, [16]. The method is applied in the second experiment where the number of sub cost functions used is $\check{m} = 6$. For the PFs in experiment one where the number of sub cost functions was $\check{m} = 3$, traditional three dimensional plots are used. The next subsection will introduce a method to compare multidimensional point clouds.

2-3-5 Comparing Point Clouds by Average Direction Vectors

In this thesis reproducibility of the PF approximations found by the EA is assessed. A statistical proof of reproducibility is not made. This is beyond the scope of this thesis, because of the thorough statistical rigor that it requires. However an assessment of

the reproducibility is made to examine whether the EA's approximations of the PF are comparable each time.

The PF approximation is a point cloud, with the values in the cost functions as the coordinates. A method to compare point clouds was reported in, [18]. It is a three step process to compare multidimensional calibration data in chemistry. Two of the methods however require a normal distribution of the data set. As this cannot be guaranteed for the PF approximation, these methods are not applied. The remaining method compares the ADV of the point clouds. The ADV is attained via the help of singular value decomposition. In the following, the application of the method is explained.

Suppose there are two solutions as PF approximations to the MOP, where the objective function values are contained in the matrices

$$\mathbf{J}^*_{\mathbf{P},\mathbf{1}} \in \mathbb{R}^{\check{g}_1 \times \check{m}}\,, \tag{2-120}$$

$$\mathbf{J}^*_{\mathbf{P},\mathbf{2}} \in \mathbb{R}^{\check{g}_2 \times \check{m}}\,. \tag{2-121}$$

The number of cost functions used in the multiobjective optimization is given by $\check{m}$, and the number of solution points in each data set is given by $\check{g}_1$, and $\check{g}_2$. The matrices are column centered. This is done by subtracting the average of each column from that column, and results in the column–centered matrices $\mathbf{J}^*_{\mathbf{P},\mathbf{1c}}$ and $\mathbf{J}^*_{\mathbf{P},\mathbf{1c}}$. The singular value decomposition is applied each of the column–centered matrices as

$$\mathbf{J}^*_{\mathbf{P},\mathbf{1c}} = \mathbf{U_1}\mathbf{\Sigma_1}\mathbf{V_1}'\,, \tag{2-122}$$

$$\mathbf{J}^*_{\mathbf{P},\mathbf{2c}} = \mathbf{U_2}\mathbf{\Sigma_2}\mathbf{V_2}'\,. \tag{2-123}$$

The $\check{m}$ loading vectors $\mathbf{c}_{\mathbf{1c},m}$ are the eigenvectors of $\mathbf{J}^{*'}_{\mathbf{P},\mathbf{1c}}$ and contained in the columns of $\mathbf{V}_1$ (equivalent for $\mathbf{J}_{\mathbf{P},\mathbf{2c}}$). Their corresponding eigenvalues $\lambda_{\mathbf{1c},m}$ are the singular values $\sigma_{\mathbf{1c},m}$ in $\mathbf{\Sigma_1}$. The relationship between singular values and eigenvalues is given by $\lambda_{\mathbf{1c},m} = \sigma^2_{\mathbf{1c},m}$ for $m \in \{1,\ldots,\check{m}\}$. The sign in the matrices $\mathbf{V}$, and $\mathbf{U}$ is not well defined during singular value decomposition. It is possible, that the vectors $\mathbf{c}_{\mathbf{1c},m}$ and $\mathbf{c}_{\mathbf{1c},m}$ are collinear, but their sum $\sum_{m=1}^{\check{m}} \mathbf{c}_{\mathbf{1c},m}$ is not. This is the case when $\mathbf{c}_{\mathbf{1c},m} \approx -\mathbf{c}_{\mathbf{1c},m}$. It is suggested by, [18], to orient each eigenvector by performing a scalar product for each eigenvector and a vector of

$$\frac{[1_1,\ldots,1_{\check{m}}]}{\sqrt{1_1^2+\cdots+1_{\check{m}}^2}}\,. \tag{2-124}$$

The sign of the eigenvector is reversed, when the result is negative. This process needed to be adapted, because an eignevector $\mathbf{c}_{\mathbf{1c},m}$ which is nearly orthogonal to the vector of equation (2-124) might be reversed, while its counterpart $\mathbf{c}_{\mathbf{2c},m}$ is not. Even though $\mathbf{c}_{\mathbf{1c},m} \approx \mathbf{c}_{\mathbf{2c},m}$. Instead a new vector

$$\mathbf{s} = \sum_{m=1}^{\check{m}} \mathbf{c}_{\mathbf{1c},m}\,, \tag{2-125}$$

was created. The new algorithm for changing the sign is

$$\frac{\mathbf{s}'\mathbf{c}_{\mathbf{1c},m}}{|\mathbf{s}||\mathbf{c}_{\mathbf{1c},m}|} = \begin{cases} < 0\,, \mathbf{c}_{\mathbf{1c},m} = -\mathbf{c}_{\mathbf{1c},m} \\ \geq 0\,, \mathbf{c}_{\mathbf{1c},m} = \mathbf{c}_{\mathbf{1c},m} \end{cases}, \qquad \forall m\,. \tag{2-126}$$

The same process also done for $\mathbf{c}_{\mathbf{2c},m}$ with the same vector $\mathbf{s}$. After the correction of the direction of the eigenvectors, the ADV $\mathbf{b}_{\mathbf{1c}}$ of the matrix $\mathbf{J}^*_{\mathbf{P},\mathbf{1c}}$ is calculated by,

$$\mathbf{b}_{\mathbf{1c}} = \sum_{m=1}^{\check{m}} \lambda_{\mathbf{1c},m}\mathbf{c}_{\mathbf{1c},m}\,. \tag{2-127}$$

For the second point cloud the ADV $\mathbf{b}_{\mathbf{2c}}$ is calculated in a similar fashion. Calculating the normed scalar product of the ADVs yields the cosine of the angle α between them as

$$\cos(\alpha) = \left| \frac{\mathbf{b}'_{\mathbf{1c}}\mathbf{b}_{\mathbf{2c}}}{|\mathbf{b}_{\mathbf{1c}}||\mathbf{b}_{\mathbf{2c}}|} \right|. \tag{2-128}$$

Two point clouds are seen as similar, when $\alpha < 45°$, [18].

The general aspects of multiobjective optimization have been now covered. The next section will cover the specifics of the multiobjective algorithm that was used in this thesis.

2-4 Multiobjective Optimization with spMODEx Algorithm

This section provides an overview of the Multiobjective Differential Evolution with Spherical Pruning X algorithm. In the first subsection the general working of the algorithm is explained. Subsection two explains the Differential Evolution search algorithm that is employed by Multiobjective Differential Evolution with Spherical Pruning X (spMODEx). The last subsection details the spherical pruning mechanism with which the archive is pruned, to achieve a good solution spread over the Pareto Front.

2-4-1 Multiobjective Algorithm spMODEx

The weighting matrices of the MPC controller as presented in subsection 2-2-3 strongly influence the solution of the optimal input sequence. In order that the controlled functions in an ideal way it needs to be tuned. A controller that is tuned poorly can lead to too high inputs, ultimately destabilizing the system. Finding appropriate factors for weighting matrices of the controller to make it behave in a desired way is the domain of controller tuning. Controller tuning can be stated as a multiobjective optimization problem. This optimization problem is subsequently solved by applying an EA. This subsection will give a summary of the EA, which used for the controller tuning.

The algorithm applied for the controller tuning is the spMODEx.[8] It is the continually updated version of the Multiobjective Differential Evolution with Spherical Pruning-II (spMODE-II)[9] algorithm, presented in, [16]. The basis of which was the Multiobjective Differential Evolution with Spherical Pruning (spMODE)[10] algorithm published by, [19]. It employs a version of the DE algorithm as an EA. This is combined with an archive which uses a pruning strategy called spherical pruning. The archive is used to continuously update the population of the DE algorithm to prevent stagnation and ensure a well spread of the PF. A detailed description of spMODEx and its application for controller tuning is found at [16], and [2].

The DE algorithm was first conceived by, [20], and will be examined in the next subsection. The initial population is found by random initialization of the decision variables. Additionally spMODEx provides the possibility to start with customized population. As a Selection mechanism spMODEx offers three different possibilities: Global Physical Programming, a Push–Strategy and Spherical Pruning.

[8] Available at: https://de.mathworks.com/matlabcentral/fileexchange/65145
[9] Availbale at: https://de.mathworks.com/matlabcentral/fileexchange/47035
[10] Availbale at: https://de.mathworks.com/matlabcentral/fileexchange/39215

Global Physical Programming allows to specify regions of interest, with which the solution of the MOP is guided. It was first conveived by [21]. The selection meachnism, as it is implemented in spMODEx, returns only one solution after optimization, and is thus not useful for the analyzation of a PF. The Push–Strategy employs a purely greedy heuristic, carrying only the best individuals from one generation to the next. However, the archive is not used. During preceding experiments, this strategy turned out to be inferior, when compared with the final selection mechanism, spherical pruning.

The spherical pruning mechanism is designed to achieve more pertinent solutions over the PF, [19]. Pareto optimal solutions found during the optimization are stored in an external archive. To prevent the agglomeration of many points in the same solution space, points are pruned from the archive. The points to remain are selected by normalizing the solutions in the archive on a spherical grid. With the archive divided into sectors, the points with the smallest length according to a norm are selected, to stay in the archive. Approximately half of the population of the DE algorithm is updated in each generation with solutions from the archive. As a stopping criteria, a maximum number of generation, or a maximum number of cost function evaluations can be used, [2], [16].

The follwing paragraphs explain one iteration of spMODEx. The description is not only based on the material of, [2], but also on close examination from the source code. This had to be done, because the creation of the sub–population is not explicitly covered in, [2]. Staying close to the graphical representation of an EA from figure 2-4, the spMODE algorithm was graphically summarized in figure 2-5.

During the random initialization test vectors, are created, evaluated via the cost-function and selected. The Pareto optimal solutions are stored in the archive $\mathbf{W}|_{G=0}$. A sub–population of parent vectors $\zeta^i|_{G=1}$ is created to be used in the DE process. The individuals in a generation range from $i \in \left\{1, \ldots, \check{i}\right\}$, where $\check{i}$ is the total number of individuals. The number of decision variables range from $j \in \left\{1, \ldots, \check{j}\right\}$, where $\check{j}$ is the total number of decision variables in the MOP. The generation counter is denoted by $|_G$, and is currently in the first generation $|_{G=1}$. The DE process creates a new set of test vectors $\mathbf{t}^i$ which are evaluated using the cost function $\mathbf{J}$. A child vector $\mathbf{t}^i$ is selected over its parent vector ζ^i according to Pareto Dominance (definition 2-3.1).

The external archive is update separately. The solutions in the archive $\mathbf{W}|_{G-1}$ are combined with the solutions from the current generation $\mathbf{t}^i$ to create a temporary archive $\widehat{\mathbf{W}}|_G$. The temporary archive is pruned according to the spherical pruning mechanism. Afterwards the Pareto Dominance selection is applied according to definition 2-3.1 to create the new archive $\mathbf{W}|_G$. If the maximum generation $|_{\check{G}}$ is reached, the spMODEx is stopped, and the archive $\mathbf{W}|_{\check{G}}$ is returned.

Else, the next iteration of spMODEx continues, by creating a new sub–population to serve as parents in the next generation $|_{G+1}$. The subpopulation is created by using half

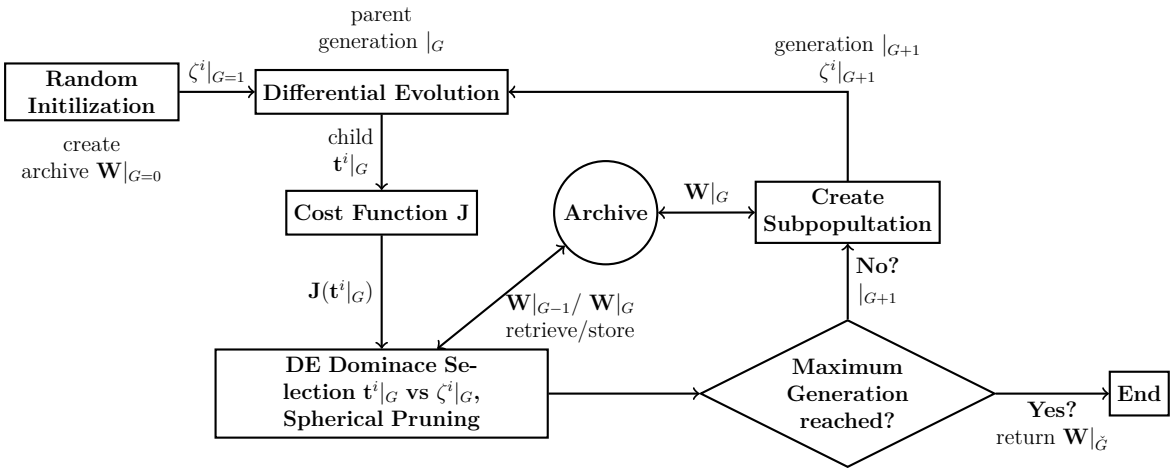

Figure 2-5: Graphical representation of spMODEx, based on the examination of the source code and, [2].

of the Pareto dominant individuals from the last iteration of the DE algorithm. The other half is consists of random individuals from the archive, plus the Anchor points from the archive. The Anchor points, are those solutions which exhibit the minimum value in one of the cost functions of $\mathbf{J} = [J_1(\zeta), \ldots, J_{\check{m}}(\zeta)]$.[11]

The next subsection covers in detail the creation of new individuals with DE. The pruning mechanism spherical pruning is discussed thereafter in subsection 2-4-3.

2-4-2 Evolutionary Algorithm: Differential Evolution

This subsection covers how the DE algorithm is employed in spMODEx. As in subsection 2-3-2, the upper index i stands for the individuals of the population, while j stands for the decision variables. For a detailed depiction on the state of the art of DE refer to, [22].

DE comprises of two different steps, the mutation and the crossover phase. The parent vectors are called target vectors, the children trial vectors. The mutation is done as follows. For the target vectors $\zeta^i|_G$ with $i \in \left\{1, \ldots, \check{i}\right\}$, where $\check{i}$ is the number of individuals in a population, containing each $j \in \left\{1, \ldots, \check{j}\right\}$ elements, where $\check{j}$ is the number of decision varibales, mutant vectors $\mathbf{v}^i|_G$ are generated at generation $|_G$ by

$$\mathbf{v}_j^i|_G = \zeta_j^{r1}|_G + F\left(\zeta_j^{r2}|_G - \zeta_j^{r3}|_G\right), \quad \forall j\,. \tag{2-129}$$

Where $r1 \neq r2 \neq r3 \neq i$ are randomly selected integers, and F is the weigthing of difference known as the scaling factor, [2].

[11] These are those solutions which contribute to the ideal point $\mathbf{J}^{\mathbf{ideal}}$ as stated in (2-115).

The crossover phase can be done in two different ways. In the binomial crossover, the calculation for each target vector $\zeta_j^i|_G$ and its mutant vector $\mathbf{v}_j^i|_G$, to form a trial vector $\mathbf{t}_j^i|_G = \left[t_1^i|_G, t_2^i|_G, \ldots, t_{\check{j}}^i|_G\right]$, is done by,

$$\mathbf{t}_j^i|_G = \begin{cases} v_j^i|_G & \text{if rand}(0,1) \leq C_r \\ \zeta_j^i|_G & \text{otherwise} \end{cases} \quad \forall j \ , \tag{2-130}$$

with the crossover probability as C_r between zero and one, and rand$(0,1)$ being a random number between zero and one, [2].

For separable problems such as $f(\mathbf{a}) = \sum_{\tilde{u}=1}^{5} f_{\tilde{u}}(a_{\tilde{u}})$, [22], the binomial recombination should be used in conjunction with a low C_r value. For non–separable problems a high C_r factor is advised. As an alternative for non–separable problems a second recombination method is suggested.

The lineal recombination is a non-rotationally invariant method of the crossover. The calculation of each target vector $\zeta^i|_G$ and its mutant vector $\mathbf{v}^i|_G$, to form a trial vector $\mathbf{t}_j^i|_G = \left[t_1^i|_G, t_2^i|_G, \ldots, t_{\check{j}}^i|_G\right]$, is done by,

$$\mathbf{t}_j^i|_G = \zeta_j^i|_G + \tilde{F}\left(\mathbf{v}_j^i|_G - \zeta_j^i|_G\right) \quad \forall j \, , \tag{2-131}$$

where $\tilde{F}$ is a second scaling factor. The recommended value is $\tilde{F} = 0.5\,(F+1)$, [23]. When in the rest of the thesis the term scaling factor is used, it is always referred to the factor F. A trial vector $\mathbf{t}^i$ (child) is selected over its target vector ζ^i (parent) if it is a Pareto optimal, [2].

The DE algorithm is now complete. The next section will focus on the spherical pruning mechanism.

2-4-3 Spherical Pruning Mechanism for Pertinent Solutions

This subsection covers the spherical pruning selection mechanism,used by spMODEx to achieve a good spread of solutions over the PF. It was first descibed in [19], and published in [2] which is the main reference of this subsection.

Let the archive $\mathbf{W}|_{G-1}$ store solutions as an approximation of the Pareto Front as

$$\mathbf{W}|_{G-1} = \left[\mathbf{K}_{\mathbf{P}}^* \quad \mathbf{J}_{\mathbf{P}}^*\right] \, , \tag{2-132}$$

with

$$\mathbf{K}_{\mathbf{P}}^* \in \mathbb{R}^{\check{g}\times\check{j}} \, , \tag{2-133}$$

$$\mathbf{J}_{\mathbf{P}}^* \in \mathbb{R}^{\check{g}\times\check{m}} \, , \tag{2-134}$$

where $\check{j}$ is the number of decision variables, $\check{g}$ is the number of individuals in the archive, and $\check{m}$ is the number of cost functions of the MOP statement from equation (2-108). The gth row of the decision variables in $\mathbf{K}_{\mathbf{P}}^{*}$ corresponds with gth row of the cost function values in $\mathbf{J}_{\mathbf{P}}^{*}$. One row contains the full description of one individual in the archive $\mathbf{W}|_{G-1}$ in generation $|_{G-1}$. With a new generation in the EA, a temporary archive $\widehat{\mathbf{W}}|_{G-1} = \left[\widehat{\mathbf{K}}_{\mathbf{P}}^{*} \quad \widehat{\mathbf{J}}_{\mathbf{P}}^{*}\right]$ is created, by adding solutions $\mathbf{J}(\mathbf{t}_j^i)$ with the corresponding trial vectors $\mathbf{t}_j^i$ to the archive $\mathbf{W}|_{G-1}$. Then the spherical pruning mechanism is applied followed by the Pareto Dominance selection as in definition 2-3.1 to create the new archive $\mathbf{W}|_G$.

The spherical pruning mechanism analyzes the archive $\widehat{\mathbf{W}}|_G$, using normalized spherical coordinates from a reference solution. The solution space of $\widehat{\mathbf{J}}_{\mathbf{P}}^{*}$ is covered by a spherical grid, and the pruning mechanism selects one solution from each sector, according to a norm. A reference solution $\mathbf{J}^{\mathbf{ref}}$, that dominates all other solutions is used. A simple approach is to choose $\mathbf{J}^{\mathbf{ref}}$ from the PF approximation by setting it equal to the ideal point[12] by

$$\mathbf{J}^{\mathbf{ref}} = \mathbf{J}^{\mathbf{ideal}}\,. \tag{2-135}$$

Spherical pruning is done by applying the following definitions.

Definition 2-4.1 (Normalized spherical coordinates, [2])**.** Given a solution ζ^i and $\mathbf{J}(\zeta^i)$, let

$$\mathbf{M}\left(\mathbf{J}(\zeta^i), \mathbf{J}^{\mathbf{ref}}\right) = [r, \beta] \tag{2-136}$$

be the normalized spherical coordinates from a refernece point $\mathbf{J}^{\mathbf{ref}}$
where $\beta = [\beta_1, \ldots, \beta_{\check{m}-1}]$ is the arc vector and $r = \| \mathbf{J}(\zeta^i) - \mathbf{J}^{\mathbf{ref}} \|_2$ is the Euclidean distance to the reference solution.

Definition 2-4.2 (Sight range, [2])**.** The sight range from the reference solution $\mathbf{J}^{\mathbf{ref}}$ to the Pareto Front approximation $\widehat{\mathbf{J}}_{\mathbf{P}}^{*}$ is bounded by $\beta^{\mathbf{U}}$ and $\beta^{\mathbf{U}}$:

$$\beta^{\mathbf{U}} = \left[\max \beta_1 \left(\mathbf{J}(\zeta^i)\right), \ldots, \max \beta_{\check{m}-1} \left(\mathbf{J}(\zeta^i)\right)\right] \forall \mathbf{J}(\zeta^i) \in \widehat{\mathbf{J}}_{\mathbf{P}}^{*}\,, \tag{2-137}$$

$$\beta^{\mathbf{L}} = \left[\min \beta_1 \left(\mathbf{J}(\zeta^i)\right), \ldots, \min \beta_{\check{m}-1} \left(\mathbf{J}(\zeta^i)\right)\right] \forall \mathbf{J}(\zeta^i) \in \widehat{\mathbf{J}}_{\mathbf{P}}^{*}\,. \tag{2-138}$$

If $\mathbf{J}^{\mathbf{ref}} = \mathbf{J}^{\mathbf{ideal}}$ then $\beta^{\mathbf{U}} = \left[\frac{\pi}{2}, \ldots, \frac{\pi}{2}\right]$, and $\beta^{\mathbf{L}} = [0, \ldots, 0]$.

Definition 2-4.3 (Spherical grid, [2])**.** Given a set of solutions in the objective space, the spherical grid on the $\check{m}$-dimensional space in arc increments $\beta^{\epsilon} = \left[\beta_1^{\epsilon}, \ldots, \beta_{\check{m}-1}^{\epsilon}\right]$ is defined as:

$$\Lambda^{\widehat{\mathbf{J}}_{\mathbf{P}}^{*}} = \left[\frac{\beta_1^{\mathbf{U}} - \beta_1^{\mathbf{L}}}{\beta_1^{\epsilon}}, \ldots, \frac{\beta_{\check{m}-1}^{\mathbf{U}} - \beta_{\check{m}-1}^{\mathbf{L}}}{\beta_{\check{m}-1}^{\epsilon}}\right]\,. \tag{2-139}$$

[12] See equation(2-115)

Definition 2-4.4 (Spherical sector, [2])**.** The normalized spherical sector of a solution ζ^i is defined as

$$\Lambda^{\epsilon}(\zeta^i) = \left[\left\lceil \frac{\beta_1 \left(\mathbf{J}(\zeta^i) \right)}{\Lambda_1^{\widehat{\mathbf{J}}_{\mathbf{P}}^*}} \right\rceil, \ldots, \left\lceil \frac{\beta_{\check{m}-1} \left(\mathbf{J}(\zeta^i) \right)}{\Lambda_{\check{m}-1}^{\widehat{\mathbf{J}}_{\mathbf{P}}^*}} \right\rceil \right] . \tag{2-140}$$

Definition 2-4.5 (Spherical pruning, [2])**.** Given two solutions ζ^1 and ζ^2 from a set, ζ^1 has preference in the spherial sector over ζ^2 if:

$$\left[\Lambda^{\epsilon}(\zeta^1) = \Lambda^{\epsilon}(\zeta^2) \right] \wedge \left[\parallel \mathbf{J}(\zeta^1) - \mathbf{J}^{\mathbf{ref}} \parallel_p < \parallel \mathbf{J}(\zeta^2) - \mathbf{J}^{\mathbf{ref}} \parallel_p \right] \tag{2-141}$$

where $\parallel \mathbf{J}(\zeta) - \mathbf{J}^{\mathbf{ref}} \parallel_p = \left(\sum_{m=1}^{\check{m}} |\mathbf{J}_m(\zeta) - \mathbf{J}_m^{\mathbf{ref}}|^p \right)^{\frac{1}{p}}$ is a suitable p-norm.

Only the solutions that have the preference in their spherical sector are kept. A graphical representation of the spherical pruning process can be found at [2]. In this thesis, the 2-norm (Euclidean norm) was used as a p-norm . The new archive $\mathbf{W}|_G$ is used as a source to update some part of the population of the DE process in the next generation. It is further the output of spMODEx to the optimization problem, when the final generation is reached.

All necessary theoretical basics for the thesis haven been discussed. The next section will cover the experiment design, and how spMODEx was integrated with the model predictive controller. An additional novel analyzation method for multidimensional data is introduced. Further, the reasoning behind the decision making process for the choice of appropriate set points (SPs) of the controller is laid out.

Chapter 3

Experiment Design

The following chapter covers the design of the two experiments executed in this thesis. The first three sections cover the general control and simulation strategy, the integration of the LSSSMPC controller into spMODEx, and the cost functions used by the spMODEx algorithm. The last two sections describe in detail the design two experiments.

3-1 General Control and Simulation Strategy

The aim of this section is to give a general overview of how the control of the state space model was done. The model predictive control (MPC) controller needs to have access to all states, inputs, and disturbances of the systems. It is assumed here, that the controller has this through measurement or an observer. As the distortions cannot be known ahead of time, an appropriate estimation strategy is needed. The measurement of disturbances from the last period serve as the prediction for the next period. Every upcoming period is updated with the disturbances of the last period. Simulations will therefore always be uncompensated in the first period, because no estimation of the disturbances does exist yet.

The control of the system was done using a periodic receding horizon strategy. This means, that the input is not computed in each time step, but is fed to the system for one period. The prediction horizon was twice of the receding horizons size. Prediction and control horizon were the same in each simulation, $\check{H}_p = \check{H}_u$.

Simulations were done for multiples of the base period. European electrical power systems are supplied with a base frequency of $f = 50\text{Hz}$. One base period therefore lasts for 20ms. The sampling of the system was done as multiples of the base frequency. Taking 100 samples per period means a sampling frequency of 5000Hz, or a sampling time of $t_s = 200\mu\text{s}$. Simulation time is measured in discrete steps $t = kt_s$. For a simulation, running at 100 samples per period, for 10 periods, the discrete sampling time ranges from $\{k \in \mathbb{N} | 1, \ldots, 1000\}$.

The differential equations of the circuit diagrams were derived in continuous time. The state space models where thus also in continuous time. They were discretized using the zero order hold, and the sampling time t_s, specified for each simulation. The control of the states was done via linear state signal shaping model predictive control (LSSSMPC). The states to which this strategy is applied are indicated in each simulation. The next section will specify how Multiobjective Differential Evolution with Spherical Pruning X (spMODEx) and the MPC controller were combined.

3-2 Controller Integration into spMODEx

This section show how the MPC controller was integrated with the spMODEx algorithm. It will be explained using the model of experiment one, which is specified in equations (3-17) to (3-18). A short introduction to the system is given first. Further, the nomenclature that was introduced in subsection 2-2-5 about LSSSMPC is used.

The model used in the first experiment specified in section 3-4 has a system matrix $\mathbf{A} \in \mathbb{R}^{7\times7}$. Simulation is done at 100 samples per period and $\check{H}_p = \check{H}_u = 200$,

covering two periods. The states of the system are controlled using the referenceless LSSSMPC strategy, for states $x_1 = i_{tl1}$ ($n_c = 1$) and state $x_2 = i_{tl2}$ ($n_c = 2$). The two states are the currents that flow on the two transmission lines of the system. They are highly distorted due to non–linear loads of the system. The rest of the states are uncontrolled. As a linear shape class, the sinusoidal shape class is applied, which was given in equation (2-91).

The last controlled state is $\check{n}_x = 2$, which yields two sub weighting matrices $\mathbf{S}_{\mathbf{Q},n_c}$. The matrices $\mathbf{S}_{\mathbf{Q},1}$ for i_{tl1}, and $\mathbf{S}_{\mathbf{Q},2}$ for i_{tl2} are of dimensions $\mathbb{R}^{394\times1400}$. To form the weighting matrix $\mathbf{S}_{\mathbf{Q}}$, the sub weighting matrices are multiplied by two factors f_{n_c} such that

$$f_1\,\mathbf{S}_{\mathbf{Q},1} + f_2\,\mathbf{S}_{\mathbf{Q},2} = \mathbf{S}_{\mathbf{Q}} \in \mathbb{R}^{394\times1400}\,. \tag{3-1}$$

The weighting of the control effort is done using an identity matrix for $\mathbf{R} \in \mathbb{R}^{200\times200}$. Computing the squared root of the diagonal entries yields a temporary weighting matrix $\mathbf{S}_{\mathbf{R},\mathbf{t}}$, which is the identity itself. Therefor $\mathbf{S}_{\mathbf{R},\mathbf{t}} = \mathbf{R}$. The matrix $\mathbf{S}_{\mathbf{R},\mathbf{t}}$ is multiplied by a third factor to attain the matrix $\mathbf{S}_{\mathbf{R}}$ shown by

$$f_R\,\mathbf{S}_{\mathbf{R},\mathbf{t}} = \mathbf{S}_{\mathbf{R}} \in \mathbb{R}^{200\times200}\,. \tag{3-2}$$

The order of magnitude of the numbers in $\mathbf{R}$ and $\mathbf{Q}$ range between 10^1 and 10^{16}. The range of the factors has to be equally big, to make a sufficient alteration during the weighting. The decision variables of spMODEx are always kept between an upper and lower bound during the solution process, b_U and b_L respectively. Thus, each factor f_1, f_2, and f_R can potentially be set as one decision variable of spMODEx algorithm, with $b_L = 10^{-9}$ and $b_U = 10^{20}$.

The decision variables of spMODEx are randomly uniformly distributed between the upper bound b_U and lower bound b_L in the initialization phase, by

$$\zeta_j^i = b_L + (b_U - b_L) \times \mathrm{rand}(0{,}1)\,, \qquad \forall j\,, \forall i\,, \tag{3-3}$$

where rand(0,1) is a random number between zero and one. The population contains individuals from $i \in \left\{1, \ldots, \check{i}\right\}$, and the number of decision variables ranges from $j \in \left\{1, \ldots, \check{j}\right\}$. Thus nearly 90% of the decision variables are initialized with numbers in the order of 10^{19}. When producing new individuals with Differential Evolution (DE)'s recombination and mutation phase, it is very unlikely to reach numbers lower orders of magnitude. To circumvent this, the bounds of decision variables were set between $b_L = -9$ and $b_U = 20$. They where then applied as the power of ten, shown in

$$f_{n_c} = 10^{\zeta_{n_c}}\,, \qquad f_R = 10^{\zeta_3}\,. \tag{3-4}$$

The solution of the optimal input sequence depends on the relationship between $\mathbf{Q}$ and $\mathbf{R}$, and not on the absolute values, as can be seen from the quadratic MPC cost function statement in equation (2-62). Two sets of factors, that are the same in their ratio, but different in their absolute values, would thus lead to the same input sequence. To avoid this one variable is fixed in space, without loss of generality. Every solution to the optimization problem thus becomes unique.

To cover the same solution range as with three factors, the bounds of the decision variables need to be adjusted. Factor f_R is fixed to $f_R = 1$. The new factors result as $\tilde{f}_{n_c} = \frac{f_{nc}}{f_R}$ for the $\mathbf{S}_{\mathbf{Q},n_c}$ matrices. In this thesis the bounds are the same for all factors: The new bounds are calculated by

$$\tilde{b}_U(\tilde{f}_{n_c}) = \frac{b_U(f_{n_c})}{b_L(f_R)} = \frac{10^{20}}{10^{-9}} = 10^{29}\,, \tag{3-5}$$

$$\tilde{b}_L(\tilde{f}_{n_c}) = \frac{b_L(f_{n_c})}{b_U(f_R)} = \frac{10^{-9}}{10^{20}} = 10^{-29}\,. \tag{3-6}$$

The weighting matrices for one individual i in the population of the DE algorithm is thus described by,

$$\mathbf{S}_\mathbf{Q}(\zeta^i) = \tilde{f}_1\,\mathbf{S}_{\mathbf{Q},1} + \tilde{f}_2\,\mathbf{S}_{\mathbf{Q},2}\,, \tag{3-7}$$

$$\mathbf{S}_\mathbf{Q}(\zeta^i) = 10^{\zeta_1^i}\,\mathbf{S}_{\mathbf{Q},1} + 10^{\zeta_2^i}\,\mathbf{S}_{\mathbf{Q},2}\,, \tag{3-8}$$

where $\left\{\zeta_1^i, \zeta_2^i \in \mathbb{R} | \tilde{b}_L, \tilde{b}_U\right\}$, and

$$\mathbf{S}_\mathbf{R}(\zeta^i) = f_R\,\mathbf{S}_{\mathbf{R},t}, \tag{3-9}$$

$$\tag{3-10}$$

where $f_R = 1$. The same principle is applied for more then three decision variables. Upper and lower bound are the same for all variables, while f_R is set to one. With the integration of the decision variables into the controller covered, the next section attends to the calculations of the cost functions used in the multiobjective algorithm.

3-3 Cost Functions used for spMODEx

The output of the multiobjective optimization process highly depends on the choice of the cost functions. It was observed in preliminary experiments that the usefulness of the Pareto Front (PF) also depends on the cost function formulation. Usefulness means that the controller ultimately identifies regions which will be of interest to the decision maker. If for example the total harmonic distortion (THD) on the transmission lines is used without considering the Apparent Control Power (ACP) controller inputs become very high. The sinusoidal condition is achieved by providing the system with a high magnitude sinusoidal current. In this case the distortions have a small net effect onto the system. This section will give a short overview about the cost functions used for spMODEx, and introduces the terminology used, when referring to measurements of system variables.

3-3-1 Total Harmonic Distortion

The total harmonic distortion was measured using the discrete fast Fourier transform function from MATLAB. The function takes a discrete time signal and returns the frequency analysis. For the THD calculation, only the harmonics multiples of the base frequency (50Hz) are of interest. The harmonics content of a signal is determined by equation (2-34). The highest number of harmonics consider, called the harmonic order, was $\check{h} = 50$ in all experiments. This is in line with the recommended practice according to, [8].

It is suggest by the same authors, that THD should be measured over several seconds. This was not done, because simulations lasted only several periods. This is seen as unproblematic as the simulations provide perfect measurements. In the following experiments, the period analyzed for its THD will be specified. When the pth period of a signal is analyzed , it will be written as

$$J_m(\zeta) = \mathrm{THD}(x_n,\ p)\,, \tag{3-11}$$

where $J_m(\zeta)$ is the mth cost function of the decision variables ζ. The signal from which the measurement is taken is given by x_n. It will be referenced by the name of the signal (for example i_{tl1} being the current over the transmission line 1).

3-3-2 Apparent Control Power

The power needed by the compensator, to compensate the THD is also used as a cost function. There are three possible powers which can be measured. The root mean

square (rms) of the active power, of the reactive power, or of the ACP. The ACP is the easiest to measure. Input current and the voltage level at the compensator are multiplied for each time step. To measure reactive or active power, the phase shift is also required.

The ACP was deemed to be the most relevant, as it reflects the total control effort. High input power should be punished, regardless of being active or reactive. The measurement unit of ACP can be watt (W), but also volt ampere (VA). The second form describes the fact, that not all of the apparent power provided is active. In this thesis the second variant (VA) is used. The measurement terminology is similar to that of the THD with

$$J_m(\zeta) = \mathrm{ACP}(p)\,, \tag{3-12}$$

where $J_m(\zeta)$ is the mth cost function of the decision variables ζ. The signals are not specified in the function as they do not change. They are the input current i_{CS}, and the voltage level at the compensation source v_{CS}. The rms value of the apparent power signal is taken. The voltage level at the compensation source was estimated. The voltage drop over the resistance at linear load 2 and the control line are derived by Ohm's law. The voltage drop over the inductances are calculated using a forward difference of one time step, with the currents over linear load 1 and the control line.

3-3-3 Reactive Power Factor

To calculated the reactive power factor on transmission line 1, the phase shift between the supply voltage, and the current on the line is needed. The phase shift between voltage and current is analyzed using a user generated MATLAB toolbox. The name of the toolbox is "Phase Difference Measurement with Matlab Implementation".[1] The toolbox uses the discrete fast Fourier transform and estimates the phase shift by maximum likelihood method, returning the phase shift in radian (rad). The phase shift φ is then used to calculate the reactive power factor by applying the sine function to the angle.

The reactive power factor is a measure for the efficiency of the power system. Reactive power cannot be converted into useful work. Yet it has to be supplied by the voltage source. The terminology used for indicating the measurement of the reactive power factor is

$$J_m(\zeta) = \mathrm{QPF}(x_{n_1}, x_{n_2}, p)\,, \tag{3-13}$$

where $J_m(\zeta)$ is the mth cost function of the decision variables ζ. The signals x_{n_1} and x_{n_2} specify the voltage and current, which are analyzed. For example the voltage from the

[1] Available at https://de.mathworks.com/matlabcentral/fileexchange/48025.

grid as V_s, and the current i_{tl1} on the first transmission line. The period analyzed is given by p.

3-3-4 Root Mean Square

The last cost function used with the spMODEx algorithm is the root mean square of a voltage or a current signal. The rms is calculated by squaring the signal, averaging all values, and then applying the square root, [7]. The rms of a signal as a cost function of the multiobjective algorithm will be indicated as

$$J_m(\zeta) = \mathrm{RMS}(x_n, p)\,, \tag{3-14}$$

where $J_m(\zeta)$ is the mth cost function of the decision variables ζ. The signals measured is given by x_n. The period analyzed is given by p.

All necessary measurement terminology has now been provided. The next section covers the design of experiment one.

3-4 Experiment 1: Assessing Reproducibility of spMODEx

The following sections details the design of the first experiment. In the first subsection, the circuit diagram and the state space model of the electrical distribution grid is derived. In the second subsection a new method for assessing the reproducibility of the Pareto front is introduced.

3-4-1 Electrical System: Circuit Diagram and State Space Representation

This subsection introduces the electrical circuit diagram, and its mathematical description by a system of ordinary differential equations, used in the first experiment.

To perform a multiobjective optimization a grid model is needed that is complex enough so that trade–offs between the controlled aspects can occur. Early models consisted of one voltage source, one overall transmission line, and a single bus with multiple linear and non–linear loads. The major control goal was the compensation of the THD on the transmission line. The earlier models were however too simple, because as soon as the transmission line was targeted by the MPC controller, the system was perfectly compensated. There were no great trade–offs that had to be adjust between linear loads and the transmission line.

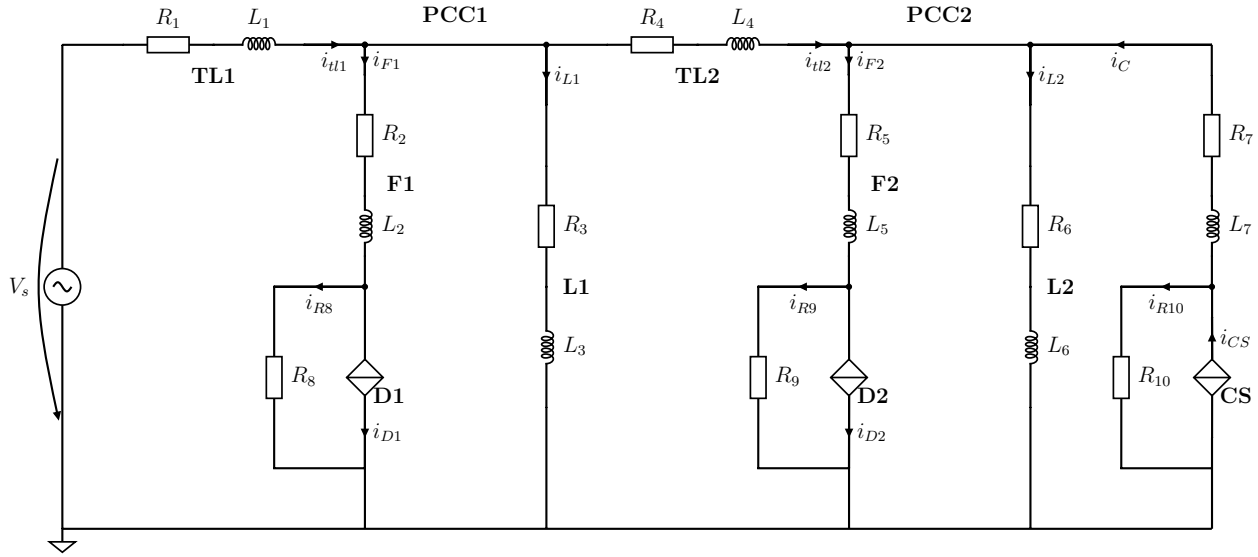

Figure 3-1: Circuit of the plant and controller model, experiment one.

For this reason the model shown in figure 3-1 was created. It consists of a voltage source V_s, that supplies the system with 230V at 50Hz. The first transmission line, transmission line 1 (TL1), is given by R_1 and L_1, and leads up to the point of common coupling 1 (PCC1). The second transmission line, transmission line 2 (TL2), is given by R_4 and L_4, and leads up to point of common coupling 2 (PCC2). The currents flowing on them are given by i_{tl1} and i_{tl2}, respectively.[2] Behind the TL1 the first feeder, feeder line 1 (F1), leads to the first non–linear distortion 1 (D1), linear load 1 (L1), and TL2 split off. They draw the current i_{F1}, i_{L1}, and i_{tl2}. The feeder current flows over R_2 and L_2 to the non–linear load D1, that draws the distortion current i_{D1}. A parallel resistance R_8 is next to the distortion. The current of L1 flows over R_3 and L_3. The nodes are described with Kirchhoffs current law as $i_{tl1} = i_{tl2} + i_{F1} + i_{L1}$, and $i_{F1} = i_{D1} + i_{R8}$.

After TL2 feeder line 2 (F2) leads to the second non–linear load distortion 2 (D2), linear load 2 (L2), and the compensation source (CS) are located. They draw the currents i_{F2} and i_{L2}. The compensation current i_C enters the same node. The second feeder current flows over R_5 and L_5, and splits into the current i_{R9} over the parallel resistance, and into the current i_{D1} which is drawn by D2. The load current of L2 flows over R_6 and L_6. The compensation current i_C flows over R_7 and L_7, and is provided by the CS, as the compensation source current i_{CS}. A small part of which follows as i_{R10} over the parallel resistance R_{10}. The second set of nodes is described by Kirchhoffs current law. At the node PCC2 by $i_{tl2} + i_C = i_{F2} + i_{L2}$, the node at D2 by $i_{F2} = i_{D2} + i_{R9}$, and the node at

[2] All currents and voltages are actually time dependent as in $i_{tl1}(t)$. The time variable t is not indicated for the whole thesis.

the CS by $i_{CS} = i_C + i_{R10}$. The voltages at PCC1, and PCC2 are given by the voltage drop over the linear loads.

The behavior of the voltage at resistances is given by Ohm's law, while the voltage behavior at inductive impedance was described in (2-5). The differential equations of the system are described, by walking through circuit branch. For example the branch containing F1 is described by

$$V_s = i_{tl1} R_1 + \frac{\mathrm{d}i_{tl1}}{\mathrm{d}t} L_1 + i_{F1} R_2 + \frac{\mathrm{d}i_{F1}}{\mathrm{d}t} L_2 + (i_{F1} - i_{D1})\, R_8 \,. \tag{3-15}$$

The equation is rearranged to

$$-\frac{\mathrm{d}i_{tl1}}{\mathrm{d}t} L_1 - \frac{\mathrm{d}i_{F1}}{\mathrm{d}t} L_2 = i_{tl1} R_1 + i_{F1} R_2 + (i_{F1} - i_{D1})\, R_8 - V_s \tag{3-16}$$

The electrical circuit is fully described by a set of seven ordinary differential equations.

$$\begin{bmatrix} 1 & -1 & -1 & 0 & -1 & 0 & 0 \\ 0 & 1 & 0 & -1 & 0 & -1 & 1 \\ -L_1 & 0 & 0 & 0 & -L_2 & 0 & 0 \\ -L_1 & 0 & -L_3 & 0 & 0 & 0 & 0 \\ -L_1 & -L_4 & 0 & 0 & 0 & -L_5 & 0 \\ -L_1 & -L_4 & 0 & -L_6 & 0 & 0 & 0 \\ 0 & 0 & 0 & -L_6 & 0 & 0 & -L_7 \end{bmatrix} \times \begin{bmatrix} \frac{\mathrm{d}i_{tl1}}{\mathrm{d}t} \\ \frac{\mathrm{d}i_{tl2}}{\mathrm{d}t} \\ \frac{\mathrm{d}i_{L1}}{\mathrm{d}t} \\ \frac{\mathrm{d}i_{L2}}{\mathrm{d}t} \\ \frac{\mathrm{d}i_{F1}}{\mathrm{d}t} \\ \frac{\mathrm{d}i_{F2}}{\mathrm{d}t} \\ \frac{\mathrm{d}i_{C}}{\mathrm{d}t} \end{bmatrix} \tag{3-17}$$

$$= \begin{bmatrix} 0 \\ 0 \\ i_{tl1} R_1 + i_{F1} R_2 + (i_{F1} - i_{D1}) R_8 - V_s \\ i_{tl1} R_1 + i_{L1} R_3 - V_s \\ i_{tl1} R_1 + i_{tl2} R_4 + i_{F2} R_5 + (i_{F2} - i_{D2}) R_9 - V_s \\ i_{tl1} R_1 + i_{tl2} R_4 + i_{L2} R_6 - V_s \\ i_C R_7 + i_{L2} R_6 - (i_{CS} - i_C) R_{10} \end{bmatrix} \tag{3-18}$$

The solution of the system of equations was done using MATLAB's Symbolic Math Toolbox. This yielded the analytical solution and was rearranged into the state space model with the matrices $\mathbf{A^C} \in \mathbb{R}^{7\times7}$, $\mathbf{B^C} \in \mathbb{R}^{7\times1}$, $\mathbf{B_d^C} \in \mathbb{R}^{7\times3}$, and $\mathbf{B_t^C}$ as the combination of the input and the distortion matrices. The discretisation method used was the zero

order hold. The state, input and distortion vectors are given by

$$\frac{\mathrm{d}\mathbf{x}}{\mathrm{d}t} = \begin{bmatrix} \frac{\mathrm{d}i_{tl1}}{\mathrm{d}t} \\ \frac{\mathrm{d}i_{tl2}}{\mathrm{d}t} \\ \frac{\mathrm{d}i_{L1}}{\mathrm{d}t} \\ \frac{\mathrm{d}i_{L2}}{\mathrm{d}t} \\ \frac{\mathrm{d}i_{F1}}{\mathrm{d}t} \\ \frac{\mathrm{d}i_{F2}}{\mathrm{d}t} \\ \frac{\mathrm{d}i_{C}}{\mathrm{d}t} \end{bmatrix}, \mathbf{x} = \begin{bmatrix} i_{tl1} \\ i_{tl2} \\ i_{L1} \\ i_{L2} \\ i_{F1} \\ i_{F2} \\ i_{C} \end{bmatrix}, \mathbf{u} = \begin{bmatrix} i_{CS} \end{bmatrix}, \mathbf{d} = \begin{bmatrix} i_{D1} \\ i_{D2} \\ V_s \end{bmatrix}. \tag{3-19}$$

The output matrix $\mathbf{C}^{\mathbf{C}} \in \mathbb{R}^{7\times 7}$ is an identity matrix. As no direct feed through exists, the matrix $\mathbf{D}^{\mathbf{C}} \in \mathbb{R}^{7\times 4}$ only contains zeros. The upper index bold $^{\mathbf{C}}$ means controller. This index is necessary because the model is reused in the second experiment, where it serves as the controller model only. In the first experiment controller and plant use the same model.

3-4-2 Activated Volume Method to Assess Reproducibility of the Pareto Front

This subsection introduces a novel method to assess the reproducibility of multidimensional point clouds and PFs. The idea for it was given by Prof. Dr.-Ing. Hans Schäfers of the Hamburg University of Applied Sciences.

It is unknown how well the spMODEx algorithm performs when used in conjunction with an LSSSMPC controller. The reproducibility assessment of an evolutionary algorithm (EA) is usually done by comparing its performance on a multiobjective function of which the PF is known. The PF of the LSSSMPC controller is however unknown. The connection with the tuning parameters of the controller is most likely non–linear. This is because the solution of the LSSSMPC cost function is non–linear, and additionally the cost functions used in spMODEx are non–linear measurements of the system outputs. It is therefore assumed that connection between the tuning parameters and the system behavior is non–linear itself.

To compare the PFs of multiple runs an adequate method is required that serves as a reverence for the individual runs. Due to the non–linearity of the multiobjective problem (MOP) solution simple regression is not possible. As a solution approach the activated volume method (AVM) was developed, to acquire the basis for a comparison. The fundamental idea of the AVM is to span volumes around the points of a PF. These activated volumes are then used as a basis for the comparison between individual solutions, instead of using the original points. The rest of this section will cover how these volumes are calculated.

Given a PF archive $\mathbf{W} \in \mathbb{R}^{\check{g}\times(\check{j}+\check{m})}$, where $\check{g}$ is the number of solutions, and the first$\check{j}$ columns contain the decision variables, and the next $\check{m}$ rows the values of the cost functions. The archive $\mathbf{W}$ is normalized between the lower threshold $\tilde{\mathbf{t}}^{\mathbf{L}}_m$, $m \in \{1,\dots,\check{m}\}$ and the upper threshold $\tilde{\mathbf{t}}^{\mathbf{U}}_m$, $m \in \{1,\dots,\check{m}\}$ by

$$\mathbf{W}^{\mathbf{N}}_{g,j} = \mathbf{W}_{g,j}\,, \quad \forall g\,, \forall j \tag{3-20}$$

$$\mathbf{W}^{\mathbf{N}}_{g,\check{j}+m} = \frac{\mathbf{W}_{g,\check{j}+m}}{\tilde{\mathbf{t}}^{\mathbf{U}}_m - \tilde{\mathbf{t}}^{\mathbf{L}}_m}\,, \quad \forall g\,, \forall m\,, \tag{3-21}$$

where $g \in \{1,\dots,\check{g}\}$, $j \in \left\{1,\dots,\check{j}\right\}$, and $m \in \{1,\dots,\check{m}\}$. The dimension of each objective cost function is now normalized between zero and one. This step makes the AVM computationally easier and more efficient, but encounters the danger of distorting a high number of solutions into a small space. To circumvent this, solutions of lesser interest can be pruned prior to the normalization process.

All solutions to the optimization problem are now within a hypercube, that is spanned between zero and one. The hypercube is divided into smaller hyperrectangles of $\check{m}$

dimensions and a fixed edge length for each dimension. The edge length will be referred to as the grid size. All hyperrectangles that contain a point of $\mathbf{W^N}$ are activated, and called activated volumes. The number of points in the activated volumes is counted as well. This whole process is achieved by the use of a Tensor.

Let the grid size of the mth normalized objective function be δ_m, were it is required that δ_m divides 1 as an even number. Then the Tensor $\mathbf{T}$ is in

$$\mathbf{T} \in \mathbb{N}^{\xi \times 2}\,, \tag{3-22}$$

with

$$\xi = \frac{1}{\delta_1} \times \cdots \times \frac{1}{\delta_{\check{m}}}\,. \tag{3-23}$$

Each hyperrectangle of the hypercube is now indexed by the dimension ξ. The Tensor is initialized with $\mathbf{T} = \mathbf{0}$. In the following a specific entry of the Tensor will be denoted as $\mathbf{T}[y_1, \ldots, y_{\check{m}}, x]$.[3] The coordinates of a hyperrectangle in $\mathbf{T}$ of a point g in $\mathbf{W^N}$ is given by $\varpi(g) = [y_1(g), \ldots, y_{\check{m}}(g)]$ and can be calculated by

$$y_m(g) = \left\lceil \frac{\mathbf{W}^{\mathbf{N}}_{g,\check{j}+m}}{\delta_m} \right\rceil, \quad \forall m\,. \tag{3-24}$$

The volumes in the tensor $\mathbf{T}$ are set to one for $x = 1$ by

$$\mathbf{T}\left[\varpi(g), 1\right] = 1 \quad \forall g \tag{3-25}$$

The number of points present in an activated volume are counted by applying

$$\mathbf{T}\left[\varpi(g), 2\right] = 1 + \mathbf{T}\left[\varpi(g), 2\right] \quad \forall g\,, \tag{3-26}$$

once only in an iterative process, where $g \in \{1, \ldots, \check{g}\}$. The tensor $\mathbf{T}$ is the representation of every volume that contains a point of $\mathbf{W}$, and the number of points located in each.

The tensor of one run of spMODEx is then compared with the tensor of an overall solution. This overall solution is created by combining the archives of many spMODEx optimization runs for the same system. Pareto dominance of all solution is ensured via the Pareto dominance criteria after definition 2-3.1. This prunes some solution, but from experience roughly 70 percent still remain. For the overall solution the AVM is applied as well, yielding the tensor $\mathbf{T}^*$.

[3] Please note, in this case, these are not outputs or states, but arbitrary counters. They are redeclared in this subsection only.

The number of volumes activated on average by an individual optimization run with $\mathbf{T}$ is compared to the number of volumes activated by the overall solution $\mathbf{T}^*$. The percentage covered on average, and the standard deviation are analyzed to allow an assessment of the reproducibility of the runs.

These results however depend on the chosen grid size. If the grid size is too big, every individual solution will cover a big proportion of $\mathbf{T}^*$. If the grid size is too small, with each volume barely enveloping a point, it becomes impossible for an individual run to cover more volumes than the maximum number of activated volumes it contains itself. To examine the impact of the grid size, several different sizes are used.

The next section will introduce the designs of electrical circuits for second experiment. The objective of the second experiment is to apply the multiobjective controller tuning to a complex controller plant system, and to develop a decision making strategy to identify the best controller set points in reasonable time.

3-5 Experiment 2: Controller Tuning and Decision Making Process

The goal of the second experiment is a to perform a controller tuning and develop a decision making strategy to find the best controller set points (SPs) in reasonable time. In order to make the process more realistic, controller and plant are operate in a mismatch. The optimal input sequence is computed by the controller for one period using the state space model that was presented in experiment one. The input is then handed over to the plant, which operates on a linear four mode switched system. After the simulation of one period the resulting currents of the distortions, and the initial states are handed back to the controller as the measurements of the plant, and the process repeats The controller plant model is then optimized by spMODEx.

This setup has two major advantages. The first is that the plant actually response to the system. The onset of the distortion currents is thus able to change with time, and can additionally draw more current, when the voltage is higher. The second is the mentioned controller plant mismatch. While a mismatch is undesirable in reality it is normally unavoidable, because only the most important system aspects are modeled. Either because the unmodeled aspects have a small net effect, or system is too complex to be fully modeled. This mismatch setup is therefore seen as beneficial to the overall research goal, and seen as a more real scenario. It therefore additionally tests how well the LSSSMPC controllers ability is to deal with a complex system.

The rest of this section is as follows. First an equivalent circuit for a rectifier is introduced. A rectifier is a device, that transforms AC into DC current, and draws a highly non–linear current. The rectifier is translated into two distinct linear state space models. Next the four modes of the plant model are derived. When the system is established, the control strategy is covered. The section concludes by examining the strategy that is employed for decision making process.

3-5-1 Linear Model of a Rectifier

A rectifier is used in this thesis to serve as a model for a non–linear load. A rectifier is a device that transforms alternating current (AC) to direct current (DC), [4]. A low power example is a laptop computer, where the transformation from 230V is done by the AC adapter in the power cord. The computer is then supplied by roughly 20V DC.

The conversion from AC to DC can be achieved, by altering how the load is connected to the voltage supply in every half period. For the positive half wave of the AC voltage, the load can be directly connected to the positive side of the load, while the ground side of the load is connected to ground of the supply. When the negative half wave arrives,

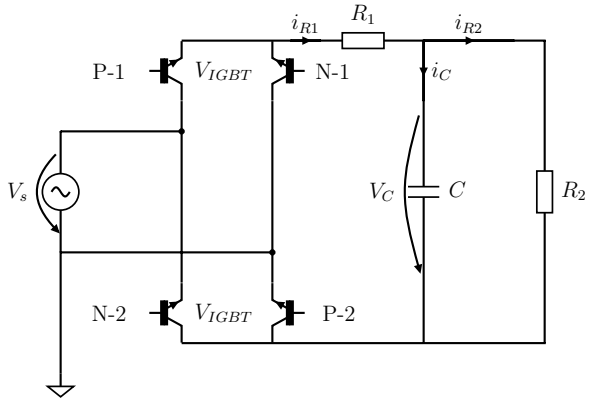

Figure 3-2: Model of a rectifier using four insulated-gate bipolar transistors.

the positive load side is connected to ground, while the negative side is connected to the now negative side of the supply,[4]. The alternating connection can be achieved passively through the use of diodes that allow one–directional current flow only.

An alternative is to use electronic switches, such as the insulated-gate bipolar transistor (IGBT). These electronic switches are made from semiconductors and have a wide range of application. They are found in ignition systems of engines, lightbulbs, energy storages, and in the displays of plasma TVs. Since IGBTs are made from semiconductors they experience a similar voltage drop like diodes, known as the saturation voltage. This drop is in the range of 1.5V to 3V per switch, [24].

In figure 3-2 an example of a rectifier circuit is given, [4]. An AC voltage source is connected via four IGBTs to a linear load R_2. Next to the load R_2 is a capacitor C. The capacitor serves as a buffer, to keep the voltage at a stable level. The internal resistance R_1 is usually not present in standard depictions of rectifiers. It was introduced for modeling purposes in the four mode switched system, which is why it is also shown here. When the IGBTs are in the off position, the circuit is solely supplied by the capacitor voltage V_C.

The switches only open, when the absolute value of the supply voltage V_s is higher than the voltage V_C, the voltage drop over the two insulated-gate bipolar transistor and the voltage drop over R_1 combined. That way it is ensured, that current only flows to the capacitor and not back into the grid. Referring to figure 3-2, the switches P-1 and P-2 open for the positive half wave. On the negative half wave N-1 and N-2 open, effectively connecting the positive side of the circuit to ground. Because the supply voltage is negative, this leads to a net positive voltage for the circuit. The AC voltage is converted to DC.

In reality IGBTs don't simply switch on and off, but have short transitioning phase between on– and off–state. Neglecting these intermediate states, the behavior of on–

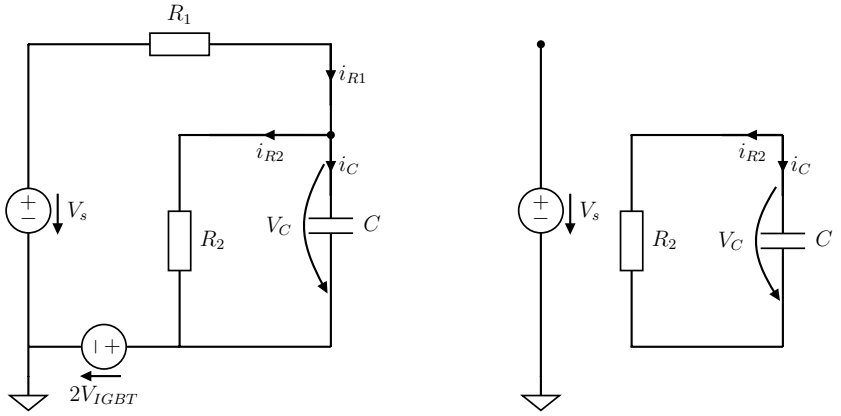

a) Equivalent circuit of the on–state. When $|V_s| > 2V_{IGBT} + V_C + V_{R1}$.

b) Equivalent circuit of the off–state. When $|V_s| < 2V_{IGBT} + V_C + V_{R1}$.

Figure 3-3: Substitute circuits for on–and off–state of a rectifier. A positive half wave of the supply voltage is assumed.

and off–states can each be described by two substitute circuits, shown in figure 3-3.

Figure 3-3 a) shows the equivalent circuit of the on–state of the IGBTs, for the positive half wave of the supply voltage V_s. The voltage source is connected via the resistor R_1 to the capacitor C and the load R_2. Located after load and capacitor is a second constant DC voltage source, that models the saturation voltage drop over the IGBTs. In the real circuit, two IGBTs are opened at the same time. Therefore the equivalent voltage is two times the saturation voltage of one switch as $2\,V_{IGBT}$. The on–state is described by four equations

$$V_s = i_{R1}R_1 + V_C + 2V_{IGBT}\,, \tag{3-27}$$

$$i_{R1} = i_{R2} + i_C\,, \tag{3-28}$$

$$V_C = i_{R2}R_2 \tag{3-29}$$

$$i_C = \frac{\mathrm{d}V_C}{\mathrm{d}t}\,. \tag{3-30}$$

The circuit can be summarized by a single differential equation as

$$\frac{\mathrm{d}V_C}{\mathrm{d}t} = -\frac{1}{R_1 C}\left(i_{R2}R_1 + V_C + 2V_{IGBT} - V_s\right)\,. \tag{3-31}$$

The equivalent circuit of the off–state of the IGBTs is shown in figure 3-3 b). The supply voltage is at open circuit, not supplying any further components. Next to it is the load circuit, where R_2 is supplied by the voltage V_C of the capacitor C. This is

described by equations

$$i_{R2} = i_C \,, \tag{3-32}$$

$$i_C = \frac{\mathrm{d}V_C}{\mathrm{d}t} \,, \tag{3-33}$$

$$V_C = i_{R2} R_2 \,. \tag{3-34}$$

The whole system is described in one differential equation given by

$$\frac{\mathrm{d}V_C}{\mathrm{d}t} = \frac{1}{R_2 C} V_C \,. \tag{3-35}$$

These two models can be used to describe the essential behavior of a rectifier for the positive half wave of the supply voltage. The negative half wave can be described by reversing the sign of the supply voltage for the negative half wave of the cycle. Alternatively the sign of the capacitor voltage V_C and the voltage drop $2V_{IGBT}$ can be reversed. The model in in figure3-3 a) is used when $|V_s| > 2V_{IGBT} + V_C + V_{R1}$. The model in figure 3-3 b) is used for $|V_s| < 2V_{IGBT} + V_C + V_{R1}$. Using only two models like this will produce an error in the moment where the actual switching occurs. It is assumed that the error is sufficiently small to be neglect because of the short switching time around 2µs or less, [24]. The next subsection will show how the substitute circuits are implemented in the original circuit model of figure 3-1.

3-5-2 Electrical System: Four Mode Switched System Circuit Diagram and State Space Model

To simulate the model from the first experiment (figure 3-1) with the substitute circuits shown in figure 3-3 the models are combined. As the equivalent circuit consist of two parts and the original circuit has two rectifiers, a total number of $2^2 = 4$ circuits is needed. The four system configurations are, both rectifiers disconnected, both rectifiers connected, only the first rectifier connected with the second disconnected, and vice versa. The configurations are also referred to as the modes of the system. During simulation, the modes are switched back and fourth, hence the name four mode switched system.

The first two modes are given in figure 3-4. Figure a) shows the mode where both rectifiers are connected, while figure b) shows both rectifiers disconnected. The rectifiers are marked D1 and D2, which stands for distortion 1 and 2. The compensation source CS is unchanged to the first circuit, and modeled by an ideal current source.

The general flow of currents in the model is not described again, as it was given in subsection 3-4-1. The nomenclature of the currents, resistors, and inductances stayed

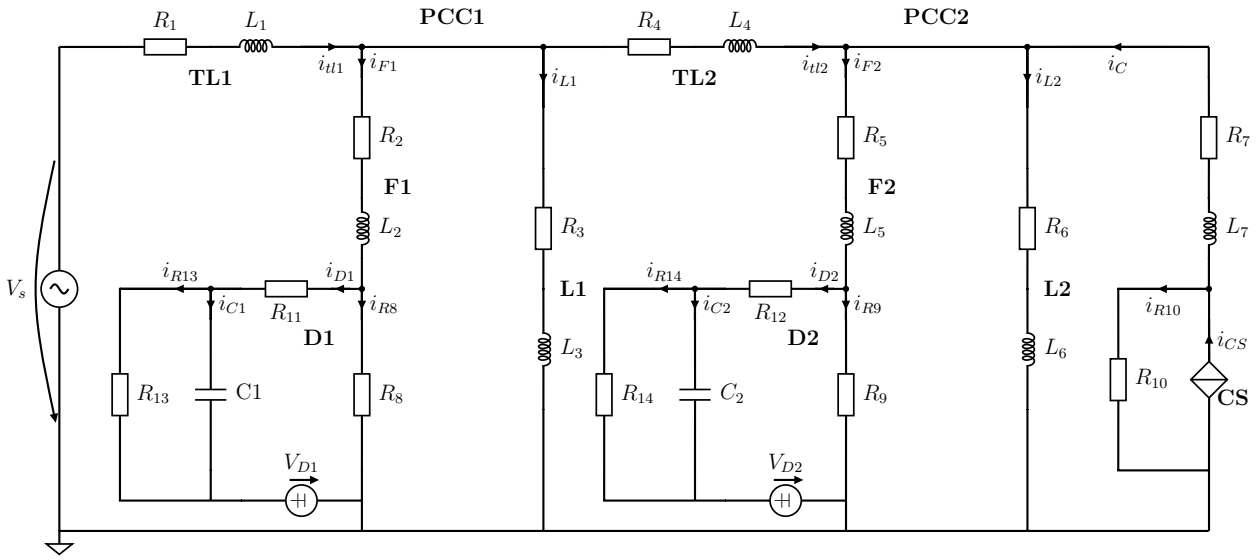

a) Both rectifiers connected to the grid.

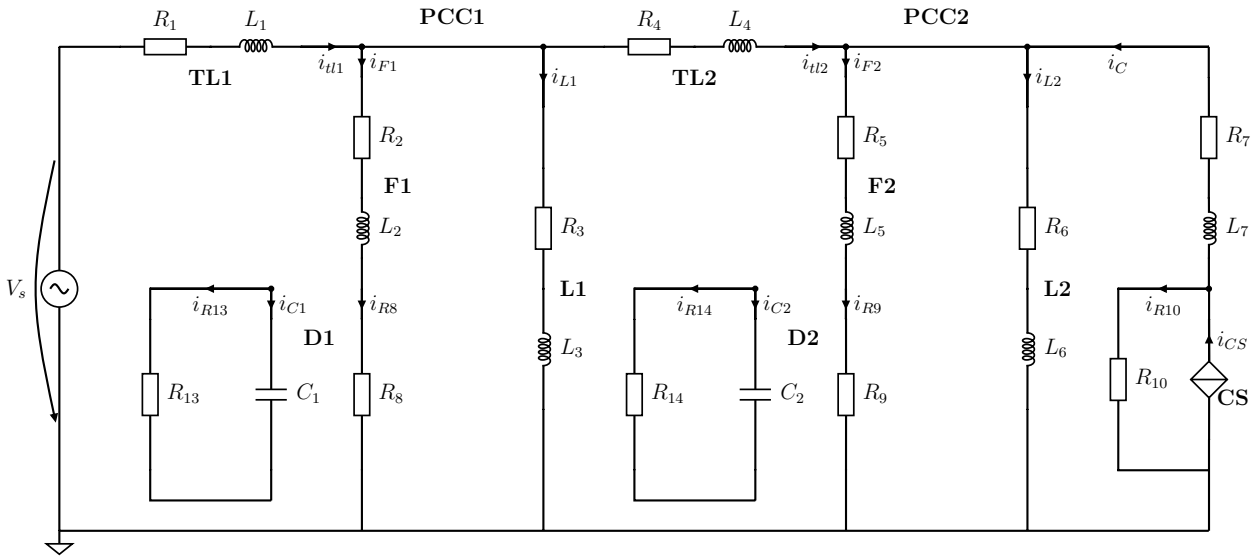

b) None of the rectifiers connected to the grid.

Figure 3-4: Equivalent circuit diagram of the four mode switched system plant model, modes one and two, experiment two.

the same as long as they are in the same location. The major changes happened around parallel resistances R_8, and R_9 of D1, and D2. The new main loads to the system are resistances R_{13}, and R_{14}. All the other components as, R_{11}, C_1, and V_{D1} for D1 and R_{12}, C_2, and V_{D2} are the components, that model the rectifier behavior into the circuit. As D1 and D2 follow the same structure, the new currents are described using D1 as an example only.

The voltage for the decision of whether the rectifier should be in the on– or off–state, is the voltage drop over the parallel resistance R_8. When the rectifier is disconnected from the grid, the current i_{R8} is equal to the feeder current that flows over R_2, and L_2. The voltage over the R_8 is thus given by $V_{R8} = i_{F1}R_8$. The behavior inside the disconnected rectifier follows the same structure as already shown in equation 3-35. The two differential equations describing the system behavior of the disconnected rectifier D1 in figure 3-4 b) is given by

$$V_s = i_{tl1}R_1 + \frac{\mathrm{d}i_{tl1}}{\mathrm{d}t}L_1 + i_{F1}R_2 + \frac{\mathrm{d}i_{F1}}{\mathrm{d}t}L_2 + i_{F1}R_8\,, \tag{3-36}$$

$$\frac{\mathrm{d}V_{C1}}{\mathrm{d}t} = \frac{1}{C_1R_{13}}V_{C1}\,. \tag{3-37}$$

The differential equations of D2 follow the same structure, only that the voltage behavior over TL2 has to be included as well.

The differential equations of the on–state of the rectifier need to consider the additional currents that are present in this model. The current on the feeder line, i_{F1}, splits into the two currents i_{D1}, and i_{R8}. The distortion current i_{D1} splits off into the current i_{C1} that charges the capacitor, and the current i_{R13} that supplies the load. Thus the system is described by

$$V_s = i_{tl1}R_1 + \frac{\mathrm{d}i_{tl1}}{\mathrm{d}t}L_1 + i_{F1}R_2 + \frac{\mathrm{d}i_{F1}}{\mathrm{d}t}L_2 + i_{D1}R_{11} + i_{R13}R_{13} + V_{D1}\,. \tag{3-38}$$

For the voltage at the capacitor the relationship $V_{C1} = V_{R13} = i_{R13}R_{13}$ exists. The distortion current is further accurately described by $i_{D1} = \frac{\mathrm{d}V_{C1}}{\mathrm{d}t}C_1 + \frac{1}{R_{13}}V_{C1}$. Thus, the differential equation can be rewritten as

$$\begin{aligned} V_s = i_{tl1}R_1 + \tfrac{\mathrm{d}i_{tl1}}{\mathrm{d}t}L_1 + i_{F1}R_2 + \tfrac{\mathrm{d}i_{F1}}{\mathrm{d}t}L_2 + \dots \\ \dots \tfrac{\mathrm{d}V_{C1}}{\mathrm{d}t}R_{11}C_1 + V_{C1}\left(\tfrac{R_{11}}{R_{13}} + 1\right) + V_{D1} \end{aligned}\,. \tag{3-39}$$

This differential equation fully describes the system behavior over the branch containing the capacitor. However, the branch containing the parallel resistance R_8 is not described by it. Therefore a second differential equation over F1 is necessary. The initial equation is given by

$$V_s = i_{tl1}R_1 + \frac{\mathrm{d}i_{tl1}}{\mathrm{d}t}L_1 + i_{F1}R_2 + \frac{\mathrm{d}i_{F1}}{\mathrm{d}t}L_2 + i_{R8}R_8\,. \tag{3-40}$$

The current over the parallel resistance is described by $i_{R8} = i_{F1} - i_{D1}$, and the distortion current is $i_{D1} = i_{C1} + i_{R13}$. Using the capacitor current voltage relationship, and that $i_{R13} = \frac{1}{R_13} V_{R13} = V_{C1}$, the second differential equation on the feeder branch becomes

$$V_s = i_{tl1} R_1 + \frac{\mathrm{d}i_{tl1}}{\mathrm{d}t} L_1 + i_{F1} R_2 + \frac{\mathrm{d}i_{F1}}{\mathrm{d}t} L_2 + i_{F1} R_8 - V_{C1} \frac{R_8}{R_{13}} \quad . \tag{3-41}$$

The differential equations relating to the second distortion D2 again follow, by considering the current flow over TL2. The modes of the system shown in figure 3-5 are simply a combination, of the modes shown in figure 3-4. Figure 3-5 a) shows the mode, where D1 is connected, while D2 is disconnected. figure 3-5 b) shows the opposite configuration.

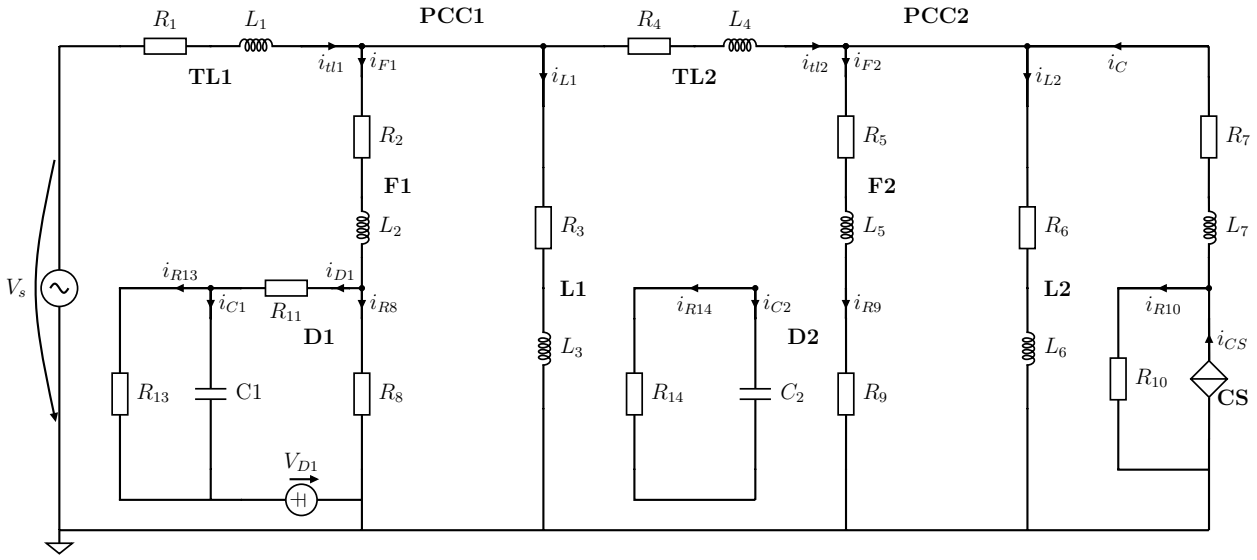

a) Rectifier D1 connected to the grid and D2 disconnected.

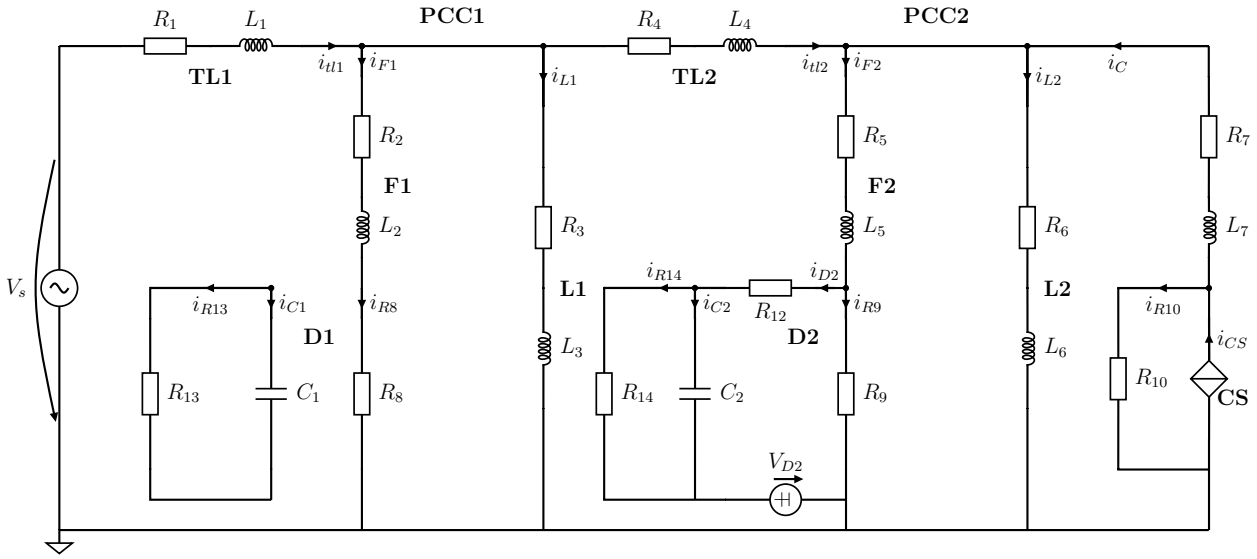

b) Rectifier D2 connected to the grid and D1 disconnected.

Figure 3-5: Equivalent circuit diagram of the four mode switched system plant model, modes three and four, experiment two.

The whole system can thus be described with a nine state model and four modes. The mode where *both* distortions are connected is described by

$$\begin{bmatrix} -L_1 & 0 & 0 & 0 & -L2 & 0 & 0 & -R_{11}C_1 & 0 \\ -L_1 & -L_4 & 0 & 0 & 0 & -L_5 & 0 & 0 & -R_{12}C_2 \\ 1 & -1 & -1 & 0 & -1 & 0 & 0 & 0 & 0 \\ 0 & 1 & 0 & -1 & 0 & -1 & 1 & 0 & 0 \\ -L_1 & 0 & -L_3 & 0 & 0 & 0 & 0 & 0 & 0 \\ -L_1 & -L_4 & 0 & -L_6 & 0 & 0 & 0 & 0 & 0 \\ 0 & 0 & 0 & -L_6 & 0 & 0 & -L_7 & 0 & 0 \\ -L_1 & 0 & 0 & 0 & -L_2 & 0 & 0 & R_8C_1 & 0 \\ -L_1 & -L_4 & 0 & 0 & 0 & -L_5 & 0 & 0 & R_9C_2 \end{bmatrix} \times \begin{bmatrix} \frac{\mathrm{d}i_{tl1}}{\mathrm{d}t} \\ \frac{\mathrm{d}i_{tl2}}{\mathrm{d}t} \\ \frac{\mathrm{d}i_{L1}}{\mathrm{d}t} \\ \frac{\mathrm{d}i_{L2}}{\mathrm{d}t} \\ \frac{\mathrm{d}i_{F1}}{\mathrm{d}t} \\ \frac{\mathrm{d}i_{F2}}{\mathrm{d}t} \\ \frac{\mathrm{d}i_{C}}{\mathrm{d}t} \\ \frac{\mathrm{d}V_{C1}}{\mathrm{d}t} \\ \frac{\mathrm{d}V_{C2}}{\mathrm{d}t} \end{bmatrix}, \quad (3\text{-}42)$$

$$= \begin{bmatrix} i_{tl1}R_1 + i_{F1}R_2 + V_{C1}\left(\frac{R_{11}}{R_{13}} + 1\right) + V_{D1} - V_s \\ i_{tl1}R_1 + i_{tl2}R_4 + i_{F2}R_5 + V_{C2}(\left(\frac{R_{12}}{R_{14}} + 1\right) + V_{D2} - V_s \\ 0 \\ 0 \\ i_{tl1}R_1 + i_{L1}R_3 - V_s \\ i_{tl1}R_1 + i_{tl2}R_4 + i_{L2}R_6 - V_s \\ i_C R_7 + i_{L2}R_6 - R_{10}\left(i_{CS} - i_C\right) \\ i_{tl1}R_1 + i_{F2}\left(R_2 + R_8\right) - V_{C1}\left(\frac{R_8}{R_{13}}\right) - V_s \\ i_{tl1}R_1 + i_{tl2}R_4 + i_{F2}\left(R_5 + R_9\right) - V_{C2}\left(\frac{R_9}{R_{14}}\right) - V_s \end{bmatrix}. \quad (3\text{-}43)$$

The discrete matrices of this model will be referred to by adding an upper index $^{\mathbf{B}}$ to them. They are $\mathbf{A^B}$, $\mathbf{B^B}$, $\mathbf{B^B_d}$, $\mathbf{B^B_t}$, $\mathbf{C^B}$. and $\mathbf{D^B}$.

For the case that *none* of the distortions are connected, the system becomes

$$\begin{bmatrix} -L_1 & 0 & 0 & 0 & -L_2 & 0 & 0 & 0 & 0 \\ -L_1 & -L_4 & 0 & 0 & 0 & -L_5 & 0 & 0 & 0 \\ 1 & -1 & -1 & 0 & -1 & 0 & 0 & 0 & 0 \\ 0 & 1 & 0 & -1 & 0 & -1 & 1 & 0 & 0 \\ -L_1 & 0 & -L_3 & 0 & 0 & 0 & 0 & 0 & 0 \\ -L_1 & -L_4 & 0 & -L_6 & 0 & 0 & 0 & 0 & 0 \\ 0 & 0 & 0 & -L_6 & 0 & 0 & -L_7 & 0 & 0 \\ 0 & 0 & 0 & 0 & 0 & 0 & 0 & 1 & 0 \\ 0 & 0 & 0 & 0 & 0 & 0 & 0 & 0 & 1 \end{bmatrix} \times \begin{bmatrix} \frac{\mathrm{d}i_{tl1}}{\mathrm{d}t} \\ \frac{\mathrm{d}i_{tl2}}{\mathrm{d}t} \\ \frac{\mathrm{d}i_{L1}}{\mathrm{d}t} \\ \frac{\mathrm{d}i_{L2}}{\mathrm{d}t} \\ \frac{\mathrm{d}i_{F1}}{\mathrm{d}t} \\ \frac{\mathrm{d}i_{F2}}{\mathrm{d}t} \\ \frac{\mathrm{d}i_{C}}{\mathrm{d}t} \\ \frac{\mathrm{d}V_{C1}}{\mathrm{d}t} \\ \frac{\mathrm{d}V_{C2}}{\mathrm{d}t} \end{bmatrix}, \tag{3-44}$$

$$= \begin{bmatrix} i_{tl1}R_1 + i_{F1}\left(R_2 + R_8\right) - V_s \\ i_{tl1}R_1 + i_{tl2}R_4 + i_{F2}\left(R_5 + R_9\right) - V_s \\ 0 \\ 0 \\ i_{tl1}R_1 + i_{L1}R_3 - V_s \\ i_{tl1}R_1 + i_{tl2}R_4 + i_{L2}R_6 - V_s \\ i_C R_7 + i_{L2}R_6 - R_{10}\left(i_{CS} - i_C\right) \\ V_{C1}\frac{-1}{R_{13}C_1} \\ V_{C2}\frac{-1}{R_{14}C_2} \end{bmatrix}. \tag{3-45}$$

The discrete matrices of the none connected mode are referred to by upper index **N**. They are $\mathbf{A^N}$, $\mathbf{B^N}$, $\mathbf{B_d^N}$,$\mathbf{B_t^N}$, $\mathbf{C^N}$. and $\mathbf{D^N}$.

The differential equations, describing the mode, where only distortion D1 with the capacitor C_1 is connected, is given by

$$\begin{bmatrix} -L_1 & 0 & 0 & 0 & -L_2 & 0 & 0 & -R_{11}C_1 & 0 \\ -L_1 & -L_4 & 0 & 0 & 0 & -L_5 & 0 & 0 & 0 \\ 1 & -1 & -1 & 0 & -1 & 0 & 0 & 0 & 0 \\ 0 & 1 & 0 & -1 & 0 & -1 & 1 & 0 & 0 \\ -L_1 & 0 & -L_3 & 0 & 0 & 0 & 0 & 0 & 0 \\ -L_1 & -L_4 & 0 & -L_6 & 0 & 0 & 0 & 0 & 0 \\ 0 & 0 & 0 & -L_6 & 0 & 0 & -L_7 & 0 & 0 \\ -L_1 & 0 & 0 & 0 & -L_2 & 0 & 0 & R_8C_1 & 0 \\ 0 & 0 & 0 & 0 & 0 & 0 & 0 & 0 & 1 \end{bmatrix} \times \begin{bmatrix} \frac{\mathrm{d}i_{tl1}}{\mathrm{d}t} \\ \frac{\mathrm{d}i_{tl2}}{\mathrm{d}t} \\ \frac{\mathrm{d}i_{L1}}{\mathrm{d}t} \\ \frac{\mathrm{d}i_{L2}}{\mathrm{d}t} \\ \frac{\mathrm{d}i_{F1}}{\mathrm{d}t} \\ \frac{\mathrm{d}i_{F2}}{\mathrm{d}t} \\ \frac{\mathrm{d}i_{C}}{\mathrm{d}t} \\ \frac{\mathrm{d}V_{C1}}{\mathrm{d}t} \\ \frac{\mathrm{d}V_{C2}}{\mathrm{d}t} \end{bmatrix}, \tag{3-46}$$

$$= \begin{bmatrix} i_{tl1}R_1 + i_{F1}R_2 + V_{C1}\left(\frac{R_{11}}{R_{13}} + 1\right) + V_{D1} - V_s \\ i_{tl1}R_1 + i_{tl2}R_4 + i_{F2}\left(R_5 + R_9\right) - V_s \\ 0 \\ 0 \\ i_{tl1}R_1 + i_{L1}R_3 - V_s \\ i_{tl1}R_1 + i_{tl2}R_4 + i_{L2}R_6 - V_s \\ i_C R_7 + i_{L2}R_6 - R_{10}\left(i_{CS} - i_C\right) \\ i_{tl1}R_1 + i_{F2}\left(R_2 + R_8\right) - V_{C1}\left(\frac{R_8}{R_{13}}\right) - V_s \\ V_{C2}\frac{-1}{R_{14}C_2} \end{bmatrix}. \tag{3-47}$$

The discrete matrices of the mode where D1 is connected, will be referred to by an upper index $^{\mathbf{C_1}}$, indicating the connected capacitor.
They are $\mathbf{A}^{\mathbf{C_1}}$, $\mathbf{B}^{\mathbf{C_1}}$, $\mathbf{B}_{\mathbf{d}}^{\mathbf{C_1}}$,$\mathbf{B}_{\mathbf{t}}^{\mathbf{C_1}}$, $\mathbf{C}^{\mathbf{C_1}}$, and $\mathbf{D}^{\mathbf{C_1}}$.

The final mode, where distortion only D2 with capacitor C_2 is described by

$$\begin{bmatrix} -L_1 & 0 & 0 & 0 & -L_2 & 0 & 0 & 0 & 0 \\ -L_1 & -L_4 & 0 & 0 & 0 & -L_5 & 0 & 0 & -R_{12}C_2 \\ 1 & -1 & -1 & 0 & -1 & 0 & 0 & 0 & 0 \\ 0 & 1 & 0 & -1 & 0 & -1 & 1 & 0 & 0 \\ -L_1 & 0 & -L_3 & 0 & 0 & 0 & 0 & 0 & 0 \\ -L_1 & -L_4 & 0 & -L_6 & 0 & 0 & 0 & 0 & 0 \\ 0 & 0 & 0 & -L_6 & 0 & 0 & -L_7 & 0 & 0 \\ 0 & 0 & 0 & 0 & 0 & 0 & 0 & 1 & 0 \\ -L_1 & -L_4 & 0 & 0 & 0 & -L_5 & 0 & 0 & R_9C_2 \end{bmatrix} \times \begin{bmatrix} \frac{\mathrm{d}i_{tl1}}{\mathrm{d}t} \\ \frac{\mathrm{d}i_{tl2}}{\mathrm{d}t} \\ \frac{\mathrm{d}i_{L1}}{\mathrm{d}t} \\ \frac{\mathrm{d}i_{L2}}{\mathrm{d}t} \\ \frac{\mathrm{d}i_{F1}}{\mathrm{d}t} \\ \frac{\mathrm{d}i_{F2}}{\mathrm{d}t} \\ \frac{\mathrm{d}i_{C}}{\mathrm{d}t} \\ \frac{\mathrm{d}V_{C1}}{\mathrm{d}t} \\ \frac{\mathrm{d}V_{C2}}{\mathrm{d}t} \end{bmatrix}, \quad (3\text{-}48)$$

$$= \begin{bmatrix} i_{tl1}R_1 + i_{F1}\left(R_2 + R_8\right) - V_s \\ i_{tl1}R_1 + i_{tl2}R_4 + i_{F2}R_5 + V_{C2}(\left(\frac{R_{12}}{R_{14}} + 1\right) + V_{D2} - V_s \\ 0 \\ 0 \\ i_{tl1}R_1 + i_{L1}R_3 - V_s \\ i_{tl1}R_1 + i_{tl2}R_4 + i_{L2}R_6 - V_s \\ i_C R_7 + i_{L2}R_6 - R_{10}\left(i_{CS} - i_C\right) \\ V_{C1}\frac{-1}{R_{13}C_1} \\ i_{tl1}R_1 + i_{tl2}R_4 + i_{F2}\left(R_5 + R_9\right) - V_{C2}\left(\frac{R_9}{R_{14}}\right) - V_s \end{bmatrix}. \quad (3\text{-}49)$$

The discrete matrices of the mode where D2 is connected, will be referred to by an upper index $^{\mathbf{C_2}}$, indicating the connected capacitor.
They are $\mathbf{A^{C_2}}$, $\mathbf{B^{C_2}}$, $\mathbf{B_d^{C_2}}$,$\mathbf{B_t^{C_2}}$, $\mathbf{C^{C_2}}$, and $\mathbf{D^{C_2}}$.

The solution of the systems of equations was done using MATLAB's Symbolic Math Toolbox. This yielded the analytical solution of the four modes and was translated into a state space model. The behavior of the individual modes was compared with simulations in LTspice from Linear Technologies, and achieved similar voltages and currents. The dimensions of the matrices of the four modes are described by $\mathbf{A} \in \mathbb{R}^{9\times9}$, $\mathbf{B} \in \mathbb{R}^{9\times1}$, $\mathbf{B_d} \in \mathbb{R}^{9\times3}$ and $\mathbf{B_t}$ as the combination of the input and distortion matrices.

$$\frac{\mathrm{d}\mathbf{x}}{\mathrm{d}t} = \begin{bmatrix} \frac{\mathrm{d}i_{tl1}}{\mathrm{d}t} \\ \frac{\mathrm{d}i_{tl2}}{\mathrm{d}t} \\ \frac{\mathrm{d}i_{L1}}{\mathrm{d}t} \\ \frac{\mathrm{d}i_{L2}}{\mathrm{d}t} \\ \frac{\mathrm{d}i_{F1}}{\mathrm{d}t} \\ \frac{\mathrm{d}i_{F2}}{\mathrm{d}t} \\ \frac{\mathrm{d}i_{C}}{\mathrm{d}t} \\ \frac{\mathrm{d}V_{C1}}{\mathrm{d}t} \\ \frac{\mathrm{d}V_{C2}}{\mathrm{d}t} \end{bmatrix}, \mathbf{x} = \begin{bmatrix} i_{tl1} \\ i_{tl2} \\ i_{L1} \\ i_{L2} \\ i_{F1} \\ i_{F2} \\ i_{C} \\ V_{C1} \\ V_{C2} \end{bmatrix}, \mathbf{u} = \begin{bmatrix} i_{CS} \end{bmatrix}, \mathbf{d} = \begin{bmatrix} V_s \\ V_{D1} \\ V_{D2} \end{bmatrix} \tag{3-50}$$

The output matrix $\mathbf{C} \in \mathbb{R}^{9\times9}$ is an identity matrix. As no direct feed through exist, the matrix $\mathbf{D} \in \mathbb{R}^{9\times4}$ contains only zeros.

Figure 3-6 shows the strategy how the switching between the modes is done. The voltage at the parallel resistance has to be equal or higher than the voltage at the capacitor, plus the voltage over the internal linear resistance, plus the saturation voltage of two IGBTs, to allow the opening of the IGBTs. Therefor voltages V_{D1} and V_{D2} are both two times the saturation voltage of a single IGBT. The exact switching conditions are given below each mode. Only one of the modes is active at any given time. The voltages at the parallel resistances in time step $k+1$ were estimated by subtracting from the source voltage V_s, the voltage drops over the serial resistances in the line, and the estimated voltage drop over the inductances. The voltage drop over the inductances is estimated by backward difference of the currents as $(i_k - i_{k+1})L$. The next subsection explains, how the models controlled by the MPC controller.

3-5-3 Control Strategy of the Four Mode Switched System

The control of the four mode switched system is achieved, by operating the MPC controller and the plant as a mismatched system. There is no mismatch in the parameters of resistances in inductances in each state space model. The plant is simulated by the

$\begin{array}{c\|c} \mathbf{A^B} & \mathbf{B_t^B} \\ \hline \mathbf{C^B} & \mathbf{D^B} \end{array}$ $\|V_{R8}\| \geq V_{C1} + V_{D1} + V_{R11}$ $\|V_{R9}\| \geq V_{C2} + V_{D2} + V_{R12}$	$\begin{array}{c\|c} \mathbf{A^{C_1}} & \mathbf{B_t^{C_1}} \\ \hline \mathbf{C^{C_1}} & \mathbf{D^{C_1}} \end{array}$ $\|V_{R8}\| \geq V_{C1} + V_{D1} + V_{R11}$ $\|V_{R9}\| < V_{C2} + V_{D2} + V_{R12}$
$\begin{array}{c\|c} \mathbf{A^{C_2}} & \mathbf{B_t^{C_2}} \\ \hline \mathbf{C^{C_2}} & \mathbf{D^{C_2}} \end{array}$ $\|V_{R8}\| < V_{C1} + V_{D1} + V_{R11}$ $\|V_{R9}\| \geq V_{C2} + V_{D2} + V_{R12}$	$\begin{array}{c\|c} \mathbf{A^N} & \mathbf{B_t^N} \\ \hline \mathbf{C^N} & \mathbf{D^N} \end{array}$ $\|V_{R8}\| < V_{C1} + V_{D1} + V_{R11}$ $\|V_{R9}\| < V_{C2} + V_{D2} + V_{R12}$

Figure 3-6: Switching strategy of the four modes. The matrices refer to the models that are the solutions to equations (3-42) to (3-49). At any time only one mode is active according to the conditions specified below each mode.

four mode switched system. To calculate the optimal input sequence for one period the controller utilizes the state space model that was given in subsection 3-4-1.

The whole input sequence is handed over to the plant, which simulates the system for one period. The estimation of the disturbance for the next period, is done by feeding the controller the disturbances of the last period. These are the supply voltage V_s, and the voltages V_{D1} and V_{D2}. To control the circuit, the MPC controller will have full freedom over all the states that can potentially be sinusoidal. These are the first four states, or i, i_{tl2}, i_{L1}, and i_{L2}. The multiobjective algorithm will thus have two additional decision variables. The cost functions of the optimization are specified in the results.

This concludes the subsection about the control of the four mode switched system. The next subsection covers the decision making strategy that was employed to choose the best controller set point, once the Pareto optimization is completed.

3-5-4 Decision Making Strategy post Multiobjective Optimization

This subsection details the decision making strategy, that is employed to find the best controller SP in a reasonable amount of time. The PF of the controller is attained as the outcome of the multiobjective optimization. The PF will most likely contain so many solutions, that a thorough analyzation of all solution is unfeasible. Additionally, some of the solutions will be in a region which is not useful from an engineering perspective. This are for example solutions, where the control effort to balance the system is way beyond the original power to supply the system in the first place.

Thus as a first step, the number of solutions is reduced to a region of interest. A region of interest is defined here as the region in where certain system boundaries are kept. Rules, regulation and physical limits can be used to do define this region, but should be applied with care.

As an example the application for a guideline on THD limit is given. In the German power grid the THD is limited to 8 % by the DIN EN 50160. As the recommendation for THD limits of IEEE is even lower, it was used in this thesis as a stronger restriction, [8]. For a system between 120V and 69kV, with a ratio of short–circuit to demand load current smaller than 20, a maximum THD of 5 % is permitted. Therefore all solutions were the current i_{tl1} on TL1 has a THD above 5 % is pruned from the PF. This could also be applied to the current on TL2 but is not useful for two reasons. Firstly, a major reason for THD restriction are the protection of generation and load equipment. As long as loads receive sinusoidal currents no problems should occur even if the current on TL2 is highly distorted. Secondly, to compensate the distortions on TL1 the CS might need to send non–linear currents over TL2.

The outcome of the pruning is a reduced PF, but will probably still contain too many points to analyze all in reasonable time. Therefor the solutions that achieve the lowest value in one of the cost functions are selected for further inspection. The points that displays the shortest normalized distance $\| \iota_g \|_2$ to the ideal point, from the unpruned and the pruned PF, according to level diagrams will be inspected as well. The selected SPs are analyzed for their stability at the end of 500 period simulation run, by analyzing the increase in the current on TL1. SPs with an increase greater then 10 % are discarded. The remaining stable set points are then analyzed fully, and the SP achieving the best overall behavior is chosen as the solution of the multiobjective controller tuning.

To summarize, the decision making process consists of:

- Prune original PF according to rules, regulations and system limits
- Select solutions where J_m is minimal of pruned PF for all m
- Select solutions where $\| \iota_g \|_2$ is minimal of pruned and unpruned PF

- Perform stability analysis after 500 periods with selected solutions. Discard solutions where current on TL1 increased by more than 10 %
- Indepth analysis of remaining SPs at the end of a 10 period simulation
- Chose best SP based on observations from the simulations

The ground work for the experiments has now been established. In the next chapter the simulation results and analysis are shown for the first experiment.

Chapter 4

Experiment 1: Assessing Reproducibility of spMODEx

This chapter presents the simulation results and analysis of reproducibility assessment of the Multiobjective Differential Evolution with Spherical Pruning X (spMODEx) algorithm. In the first sections, the simulation parameters are presented. Section two shows the result of the simulations, and section three presents the analysis.

4-1 Simulation Parameters, Control– and Tuning–Strategy

The continuous state space model of the electrical circuit shown in figure 3-1 was discretized using the zero order hold and a sampling time of $t_s = 200\mu s$. The state space model given by $\mathbf{A^C}$, $\mathbf{B_t^C}$, $\mathbf{C^C}$, and $\mathbf{D^C}$ is used by the plant, and by the controller for the calculation of the optimal input sequence.

The parameters of the resistances and inductances are shown in table 4-1. The indcutances are defined relative to their accompanying line resistances. This allows to directly set the reactive components of all circuit elements.

Table 4-1: The table shows the resistances and inductances used in the circuit diagram from figure 3-1. The inductances were defined relative to the resistances, where $w = 2\pi f = 2\,\pi\,50\text{Hz}$.

Name	**Parameter 1**	**Value**	**Parameter 2**	**Value**
Transmission line 1	R_1	0.20 Ω	L_1	$\frac{R_1 0.1}{w}\frac{\text{H}}{\Omega}$
Transmission line 2	R_4	0.05 Ω	L_4	$\frac{R_4 0.1}{w}\frac{\text{H}}{\Omega}$
Linear Load 1	R_3	5.00 Ω	L_3	$\frac{R_3 0.3}{w}\frac{\text{H}}{\Omega}$
Linear Load 2	R_6	5.00 Ω	L_6	$\frac{R_6 0.3}{w}\frac{\text{H}}{\Omega}$
Feeder 1	R_2	1.00 Ω	L_2	$\frac{R_2 0.2}{w}\frac{\text{H}}{\Omega}$
Parallel resistance **D1**	R_8	1.00 MΩ		
Feeder 2	R_5	1.00 Ω	L_5	$\frac{R_5 0.2}{w}\frac{\text{H}}{\Omega}$
Parallel resistance **D2**	R_9	1.00 MΩ		
Compensator line	R_7	1.00 Ω	L_7	$\frac{R_7 0.2}{w}\frac{\text{H}}{\Omega}$
Parallel resistance **CS**	R_{10}	1.00 MΩ		

The additional parameters for the simulation of the electrical circuit are given in 4-2. The ideal voltage sources V_s supplies an AC voltage of 230V at 50Hz. The distortion currents drawn by the distortions distortion 1 (D1) and distortion 2 (D2) are taken from the uncompensated four mode switched system presented in the next section. The initial states of the system were set to steady state behavior at the beginning of a voltage source period of the uncompensated four mode switched system. The prediction horizon $\check{H}_p$ and the control horizon $\check{H}_u$ were set to two periods. This means that $\check{H}_p = \check{H}_u = 200$, since the sampling time was 100 samples per period. The periodic receding horizon strategy is employed.

Table 4-2: General simulation parameters of the plant and controller model, experiment one.

Parameter	Magnitude	Description
f	50 Hz	Grid frequency
t_s	200 µs	Sampling time
Periods	10	Number of periods simulated
max V_s	$\sqrt{2}\,230$V	Supply voltage amplitude
$\check{H}_p$	500	Prediction horizon
$\check{H}_u$	500	Control horizon

The parameters of the spMODEx algorithm are shown in table 4-3. The recombination type of the Differential Evolution (DE) algorithm is lineal. This is because preliminary studies of the algorithm showed a higher number of solutions found with the lineal recombination, or when using binomial recombination with a high crossover factor. The crossover factor is not applicable in this experiment, because lineal recombination works without it. The maximum generation is 150. The number was intentionally kept low, to decrease the duration of one cycle of one Pareto optimization. The recommended number of individuals in the population of the search process is ten times the number of decision variables. It was chosen to be 30, because the algorithm influences three factors in front of the weighting matrices of the model predictive control (MPC) controller, even though only using two decision variables. The number of cost functions used was three. They are specified below. The number of the arc increments β^ϵ of the spherical pruning mechanism was set to 100.[1] Further setting information can be found in the table.

As cost functions of the multiobjective optimization the total harmonic distortion (THD) of the currents i_{tl1} and i_{tl2} was measured for the last period. Further the rms of the Apparent Control Power (ACP) for balancing the system was measured for the last period. The measurement of THD and ACP was covered in section 3-3. Thus, the three cost function of an individual i in the multiobjective optimization are $\mathbf{J}(\zeta^i) = [J_1(\zeta^i), J_2(\zeta^i), J_3(\zeta^i)]$ with,

$$J_1(\zeta^i) = \mathrm{THD}(i_{tl1}, 10)\,, \tag{4-1}$$
$$J_2(\zeta^i) = \mathrm{THD}(i_{tl2}, 10)\,, \tag{4-2}$$
$$J_3(\zeta^i) = \mathrm{ACP}(10)\,. \tag{4-3}$$

[1] They are specified under the name “Alpha” in the MATLAB code of spMODEx algorithm.

Table 4-3: Parameters of the spMODEx algorithm.

Parameter Description	**Value/Type**
Recombination type of DE algorithm	lineal
Maximum generation $\check{G}$	150
Number of cost functions $\check{m}$ in $\mathbf{J}(\zeta)$	3
Number of decision variables $\check{j}$ in ζ	2
Number of individual $\check{i}$ in search population	30
Total number of function evaluations	4530
Lower bound $\tilde{b}_L$ of decision variables ζ	-29
Upper bound $\tilde{b}_U$ of decision variables ζ	29
Spherical pruning strategy	enabled
Number of arcs β^{ϵ} in spherical grid	100
Norm applyed during spherical pruning	euclidean
Scaling factor F	0.1
Crossover Factor C_r	not applicable

The states were controlled using the linear state signal shaping model predictive control (LSSSMPC) control strategy. The first two states, i_{tl1}, and i_{tl2}, were targeted by the sinusoidal sub weighting matrices of the states $\mathbf{S_{Q,1}}$ and $\mathbf{S_{Q,2}}$. As the last controlled state is $n_x = 2$, they are both of dimensions $\mathbb{R}^{(394\times1400)}$. The sub weighting matrix $\mathbf{S_{R,t}}$ for the control input is $\in \mathbb{R}^{(200\times200)}$ and the identity matrix. The factor f_R for the input sub weighting matrix was $f_R = 1$. The relationship between decision variables and the factors f_1, f_2 is given by

$$f_1 = 10^{\zeta_1}\,, \quad f_2 = 10^{\zeta_2}\,. \tag{4-4}$$

For more details on the connection of the controller to the optimization algorithm refer to section 3-2.

4-2 Simulation Results

The simulation results are presented in three subsections. First the simulation of the uncontrolled system is shown. Next the results of the Pareto optimization is shown, and assessed for its reproducibility. The section finishes with the presentation of two different controlled simulations.

4-2-1 Uncontrolled System Simulation

To understand what is happening in the electrical circuit, the uncontrolled system is examined first. Figure 4-1 a) shows the behavior of the current on trasmission line 1 i_{tl1} (red dashed) and the current on transmission line 2 i_{tl2} (blue, solid), for the last four periods of the simulation. The root mean square (rms) of the current on transmission line 1 is 126.85A and has a THD of THD$(i_{tl1}, 10) = 19,71\%$. The rms value of the current reached on the second transmission line is at 62.90A with a distortion of THD$(i_{tl2}, 10) = 19,53\%$ in the last period.

For the same time frame, the supply voltage V_s (red, solid), the voltage V_{PCC1} at point of common coupling 1 (PCC1) (blue, solid, dots), and the voltage V_{PCC2} at point of common coupling 2 (PCC2) (green, dashed) are shown in figure 4-1 b). The rms voltage at PCC1 is 203.45V, and a distortion of THD$(V_{PCC1}, 10) = 4.32\%$ is measured. For PCC2 the rms voltage is 200.40V, with a distortion of THD$(V_{PCC2}, 10) = 4.51\%$. The supply voltage rms is at 230.00 and has a distortion of THD$(V_s, 10) = 1.89\%$

The currents over the linear loads are shown in figure 4-1 c). The current over linear load 1 (L1), i_{L1} (blue, solid), has an rms of 39.30A and has a harmonic content of THD$(i_{L1}, 10) = 2.17\%$. The current over linear load 2 (L2) is shown by i_{L2} (red, dashed) with a rms of $38,71$A and a harmonic content of THD$(i_{L2}, 10) = 2.34\%$.

The currents on the feeder lines, which are draw from the non–linear loads, are shown in figure 4-1 d). The current on feeder line 1 has a rms value of 27.09A and a distortion of THD$(i_{F1}, 10) = 54.06\%$. The current on the second feeder line has a rms of 26.58A with a distortion content of THD$(i_{F1}, 10) = 53.56\%$

A summary of all values, as well as the maximum value reached for each signal is given in table 4-4. Further the phase shift between the supply voltageV_s and the current on transmission line 1 i_{itl1} is measured with $-12.86°$. The phase shift between V_{PCC1} and i_{tl2} is $-11.59°$. The influence on the apparent power, active power, inductive reactive power, and the power factor can further be seen in table 4-5.

Table 4-4: Summary of current and voltages of the uncontrolled system.

Signal	**THD**$(-, 10)$	**Maximum**	**rms**
V_s	1.894 %	325.3 V	230.0 V
V_{PCC1}	4.322 %	281.6 V	203.4 V
V_{PCC2}	4.511 %	276.6 V	200.4 V
i_{tl1}	19.71 %	204.8 A	126.9 A
i_{tl1}	19.53 %	101.4 A	62.90 A
i_{L1}	2.170 %	54.61 A	39.30 A
i_{L2}	2.340 %	53.65 A	38,71 A
i_{F1}	54.06 %	49.53 A	27.09 A
i_{F2}	53.56 %	48.44 A	26.58 A

Table 4-5: Uncontrolled System. Apparent power **S**, active power **P**, inductive reactive power **Q** , Phase shift between voltage and current, and the power factor are shown, for transmission line 1 and 2.

Line	**S** [VA]	**P** [W]	**Q** [VA]	**Phase shift** [°]	**Power Factor**
TL 1	37032	36103	8243	-12.86	0.9749
TL 2	16108	15779	3236	-11.59	0.9796

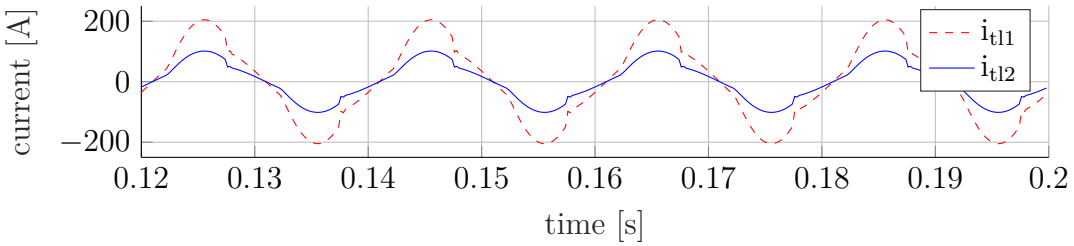

a) Currents on the transmission lines.

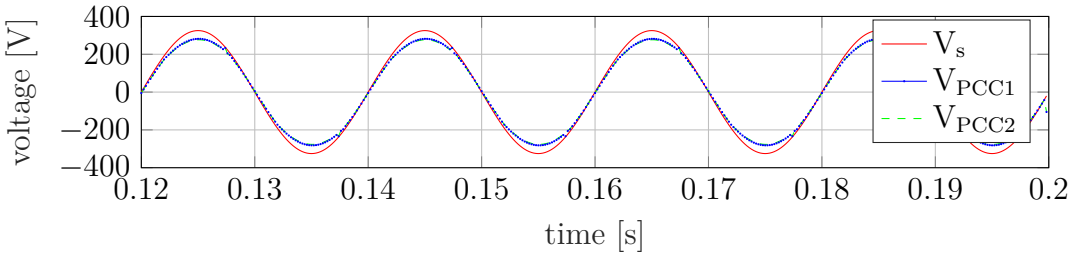

b) Supply voltage and voltages and the point of common couplings (PCCs).

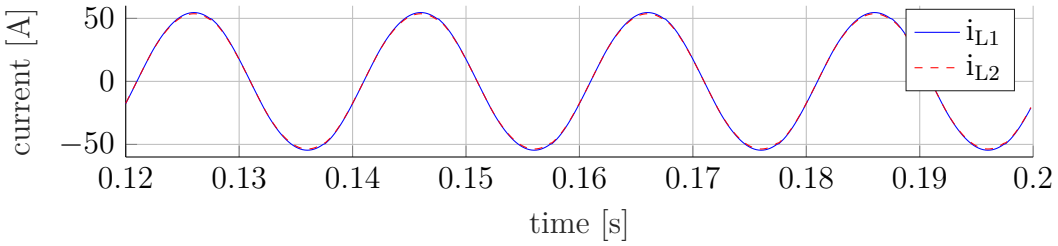

c) Currents over the linear loads.

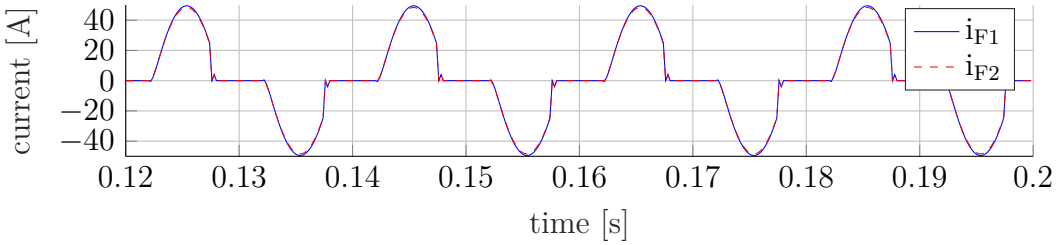

d) Currents over feeder line 1 and feeder line 2.

Figure 4-1: Uncontrolled system Simulation results, experiment one.

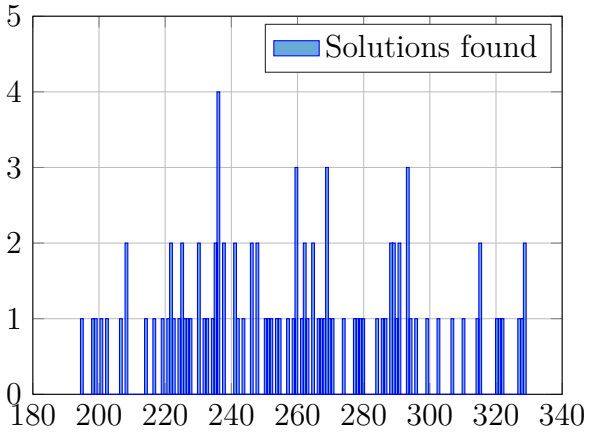

Figure 4-2: Number of Pareto optimal solutions found by one run of spMODEx. Total number of runs was 100.

4-2-2 Reproducibility of Pareto Optimization

The spMODEx algorithm was run for one hundred cycles on an "Intel i5-8250U" CPU, employing MATLAB Parallel Computing Toolbox. This yielded a total of one hundred Pareto Front (PF). The run time for one cycle of spMODEx was about 3 minutes and 16 seconds, with 4530 simulations per cycle. On average each run found 259,80 Pareto optimal solutions, with a standard deviation of 34.66 points, or 13.34 %. Figure 4-2 shows the histogram of the number of points. The highest amount of points found was 329, and was achieved two times. The minimum number was 195 and, which only occurred once. It was tested whether the number of solution found follows a normal distributed. This was done using the Chi-square variance test (MATLAB function "vartest()"), with a significance level of 5 %. The null hypothesis that the distribution follows normal distribution was not rejected.

In total, all runs combined found a total number of 25980 solutions to the Pareto Optimization problem. The archives from all runs were combined to an overall archive and subsequently pruned by the Pareto Dominance criteria. This new archive $\mathbf{W}^*$ is the overall or reference solution from all optimization runs. The total number of Pareto optimal solutions was reduced down to 20318. The share of Pareto optimal solutions per run from $\mathbf{W}^*$ is 78,21 %.

The overall solution can be seen in figure 4-3 in two perspectives. Due to display reasons every third point was pruned. This also pruned the maximum values achieved in ACP from the data set. The following discussions is based on the original data set.

The reference solution is a convex front, that varies between roughly three extreme points of maximum values in one of the costs and comparatively low values in the

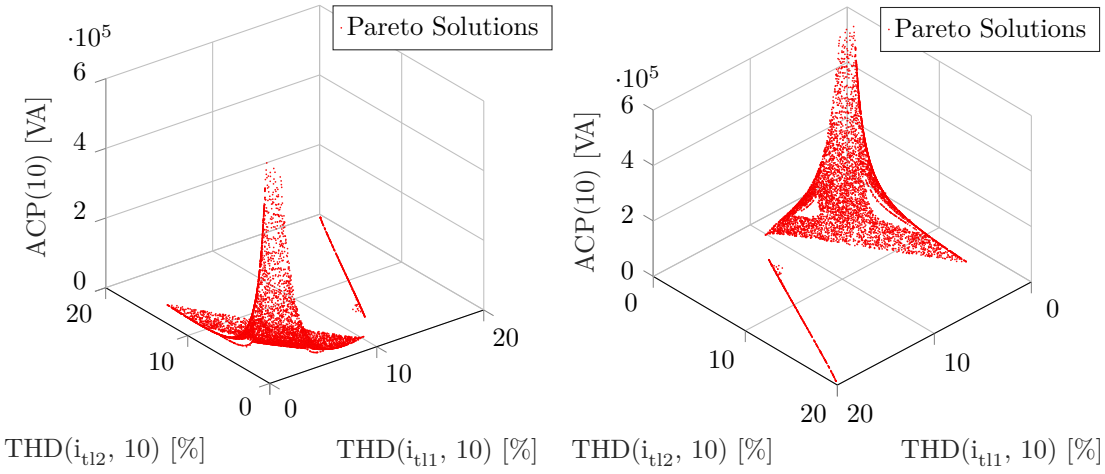

a) Perspective 1 **b)** Perspective 2

Figure 4-3: Overall Pareto Front Solution.

other. Behind the shell (Perspective 1) is a straight line. Solutions in the shell vary between roughly 10 % and 1 % THD for i_{tl1}, 1 % and 16 % for i_{tl2}, and between 2000 VA and 700000 VA for the ACP. The PF seems to bounded by curves of densely covered points, in the regions of decreasing THD in both costs, and increasing ACP. The bounds of the shell at low ACP are less populated (see Perspective 2).

Where the THD of i_{tl1} is above between roughly 19 % and 12 % the solutions are on the straight line. The ACP increases from 6×10^{-5} VA to about 2000 VA. The THD of i_{itl2} decreases from 19% to about 5%. After that follows a zone between 10 % and 12 %, where the no solutions for i_{tl1} were found, after which the convex zone of the PF follows.

Considering the location where i_{tl1} is at about 10 %, two major effects can be observed when its THD should be reduced. First, the THD of i_{tll} can be further reduced, by increasing the THD of i_{tl2} up to 16 %, which increases the ACP to about 3400 VA. The second way is to decrease the THD of i_{tl1} is by increasing the ACP up to 700000 VA. This will at the same time also decrease the THD of i_{tl2} down to 2 %. It can be observed, that solutions which have decreasing cost for both currents, lead to a stark increase in ACP. There are further regions in the convex shell, where no solutions were found.

The one hundred individual runs were analyzed according to the difference in their average direction vector from the ideal solution. All solutions achieved angles which were very close to zero. The average angle of the one hundred solutions is $1.0011 \times 10^{-4\circ}$ with a standard deviation of $1.3402 \times 10^{-4\circ}$ or 133.89 %.

Three individual solutions are shown in figure 4-6, in two perspectives. They display

Table 4-6: Varying grid sizes used in the AVM, and the corresponding sizes in the original PF solution space. The number of total volume elements in the normalized three dimensional space is shown in the last column.

Grid size $\delta_m\,, \forall m \in \{1,2,3\}$	δ_1 **in** J_1 [%]	δ_2 **in** J_2 [%]	δ_3 **in** J_3 [VA]	**Total Number of Volumes**
5×10^{-3}	0.1000	0.1000	3510.11	8000000
1×10^{-2}	0.2000	0.2000	7020.22	1000000
2×10^{-2}	0.4000	0.4000	14040.44	125000
4×10^{-2}	0.8000	0.8000	28080.88	15625
5×10^{-2}	1.0000	1.0000	35101.10	8000
1×10^{-1}	2.0000	2.0000	70202.20	1000

the runs with the highest number (329; red dots, green cross) and lowest number (195; blue stars) of points found. As the structure is similar to the reference solution, only the most important features are pointed out. The individual runs seem to cover the same convex shell, as the overall solution. However, the holes in the convex shell are filled up with points from all of the three runs. While the points of the run with 195 points, and one of the runs with 329 points (blue stars) cover the whole space, the other solution (green cross) does not cover solutions where the ACP is above roughly 340000 VA.

The 100 PFs were analyzed using the activated volume method (AVM) in comparison to the overall solution. A total of six different normalized grid sizes δ_m were analyzed. They were constant for every cost function and varied between 0.005 and 0.1. The total number of volumes in the solution space thus varied between 8×10^6 and 1000 volume elements, respectively. Table 4-6 shows the relative grid sizes of δ_m transformed to the original cost function space, and the total number of volumes.

The changing grid size has a moderate effect on the THD for cost function one an two, changing the absolute values by the order of one magnitude between 0.1 % and 2%. For cost function three, the absolute values lie at the low end at roughly 3500 VA and at the high end with 70000 VA, changing by two orders of magnitude.

The difference in how the grid size influences the approximation of the PF is shown in figure 4-5. There the centroid of each three dimensional volume element is plotted along side the overall solution, pruned to 5 % of original point content. Figure 4-5 a) contains the 7554 centroids, that resulted of applying the grid size of $\delta_m = 5 \times 10^{-3}\,, \forall m$. Figure 4-5 b) shows the 68 centroids, that resulted from applying the biggest grid size of $\delta_m = 1 \times 10^{-1}\,, \forall m$.

The centroids are displayed by diamonds in light blue color. The volume centroids in figure a) had to be shrunken down, as to not block the overall solution from appearing. The overall solution is given as red points. The side views of the PFs is displayed to

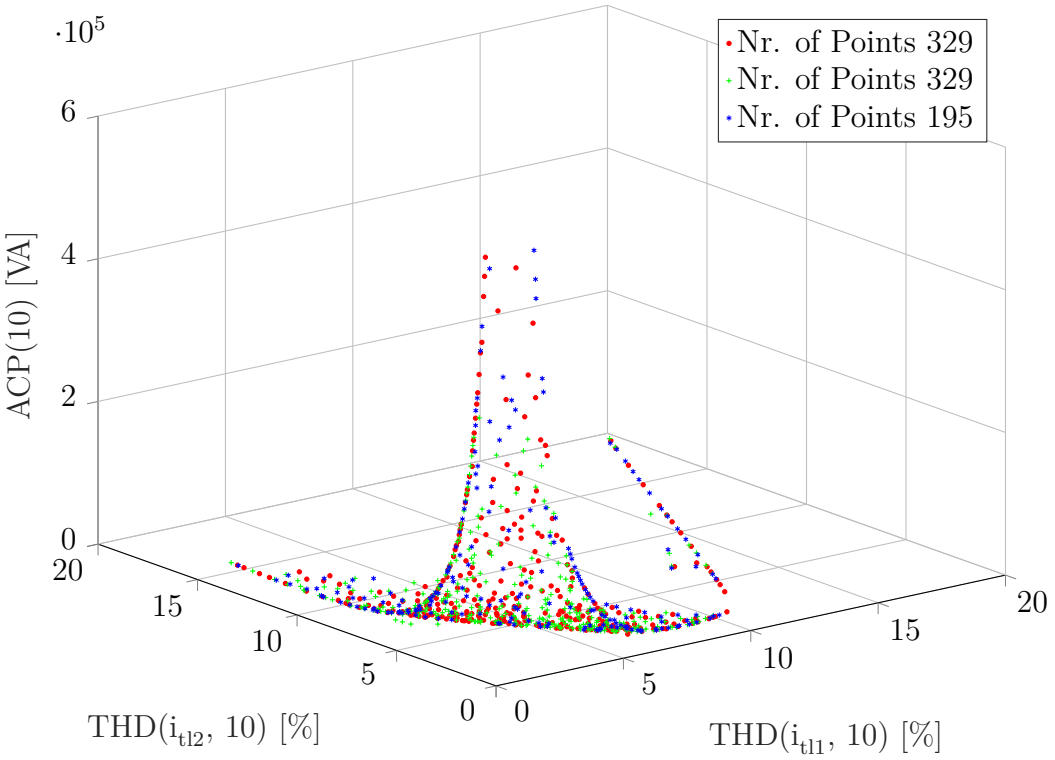

a) Perspective 1.

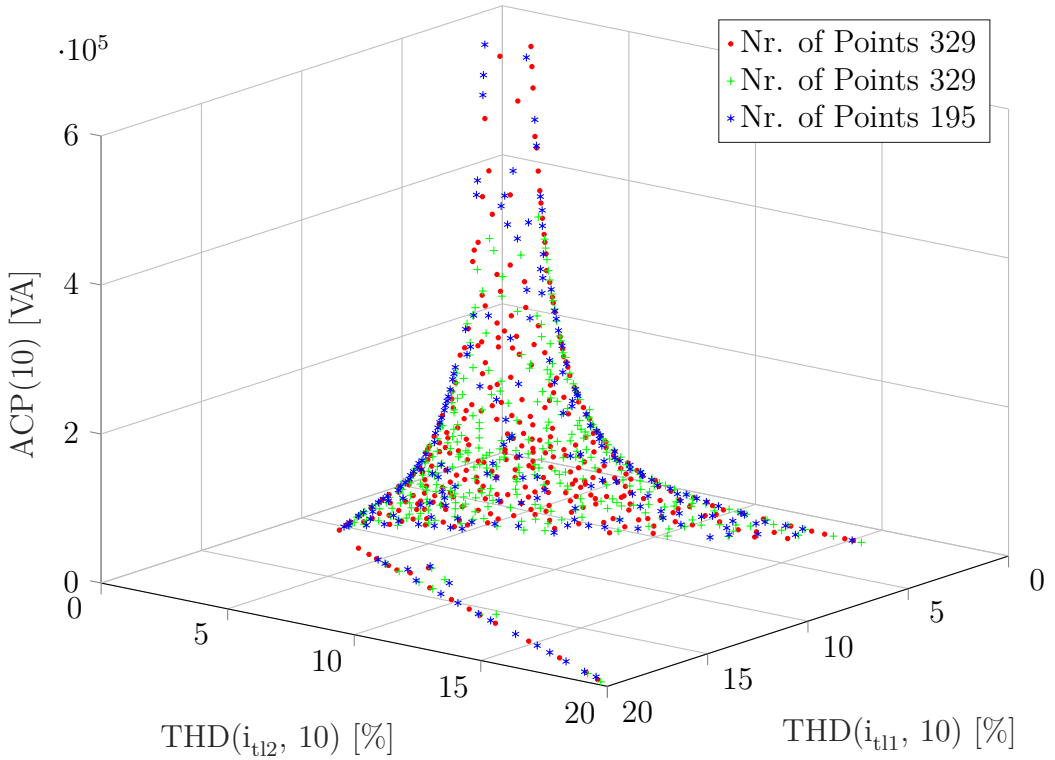

b) Perspective 2.

Figure 4-4: Individual solutions of the Pareto optimization.

show the proximity from the centroids to the reference solution. The centroids shown in figure a) are visually not distinguishable from the actual solution points. The volume centroids in figure b) are much further away from the original solution. The centroids in the lower part of the convex shell were aligned, to form a virtual line behind them. Points to the back are as far away as the distance to the next row of points.

In order to quantify the visual representation, the attained data of the volume centroids was analyzed in two ways. Firstly, the number of volumes activated by the overall solution was compared to the number of total volumes that exist in the normalized space. Secondly, the share of the volume centroids of the individual runs was compared to the number of volumes that are part of the volumes of the overall solution. This is shown in the four sub graphs of figure 4-6. The results of the overall solution are displayed in the left two figures, and the results of the averages from the 100 runs are shown on the right.

Sub figure a) shows the share of the numbers of volumes from the overall solution in the total solution space. At the smallest grid size, 0.0944% of the original space is activated. For the biggest grid size the coverage of the total number of volumes is at 6.800%. The actual number of volumes found by the overall solution is shown in c), and displays an inverse relationship to the share in the total number of volumes in the normalized space. Totaling at 7554 volumes for the smallest grid size, 258 volumes for $\delta_m \, , \forall m = 4 \times 10^{-2}$, and 68 volumes for the highest.

Sub figure b) shows the average of coverage of the individual runs from the volumes of the overall solution. At the smallest grid size, 2.881% of the overall solution is covered, with a standard deviation of 15.06 % , related to the mean.[2] At the biggest grid size, the coverage is at 80.15 % with a standard deviation of 5.169 %. With each increase in grid size from the smallest grid size to the relative grid size of 0.04, the share of covered space from the overall solution roughly doubles. The standard deviation decreases with every increase in grid size, being at 8.725% for the fourth size.

The average numbers of activated volumes from the overall solution are given in sub figure d). Staying fairly stable at around 220 correctly identified volumes of the overall solution with an accompanying standard deviation at around 30 volumes, for the first three grid sizes. The standard deviation, related to the mean[3], in sub figure b) and d) are the same. From smallest to highest grid size they are 15.06 %, 14.57 %, 13.09 %, 8.725 %, 6.862 %, and 5.167 %. At the fourth grid size from the left, a stark decrease in volumes is registered. Only 148.3 volumes were identified correctly. For the smallest grid size, 54.50 volumes are identified correctly.

[2]All standard deviations given in percent are related to the mean. Meaning, 15.06 % of 2.881 %, equaling 0.4338 %.

[3]This is because the relationship between the two figures is the division by the number of volumes activated from the overall solution.

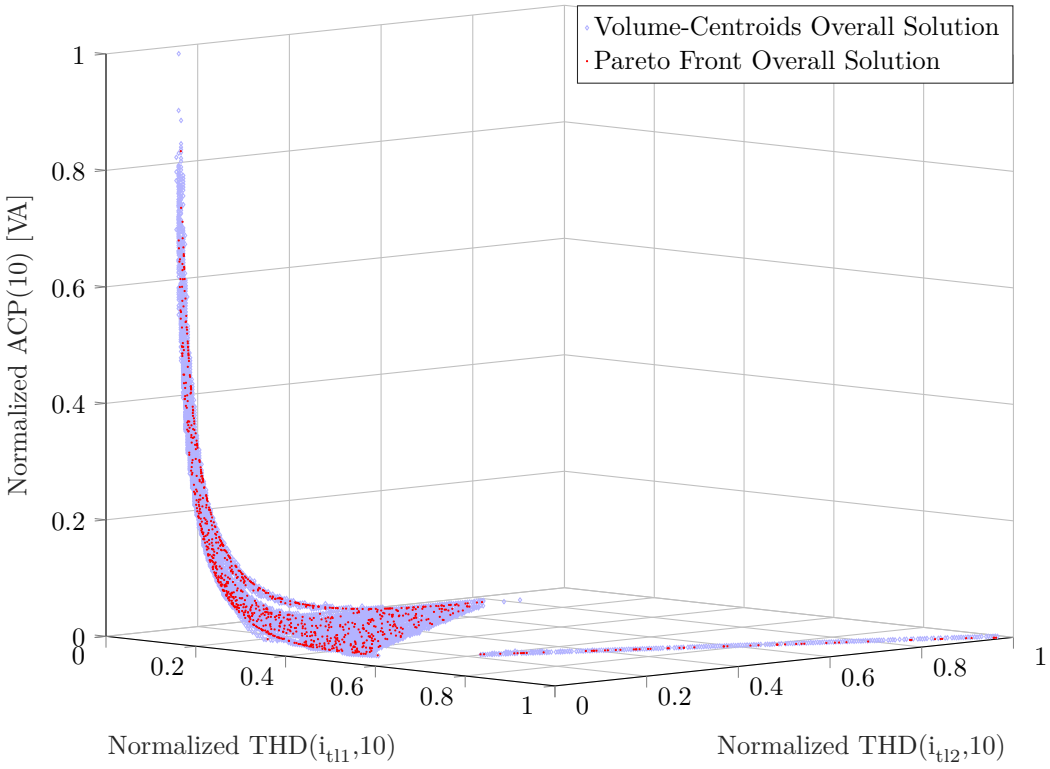

a) Smallest grid size, $\delta_m = 5 \times 10^{-3}\,, \forall m.$

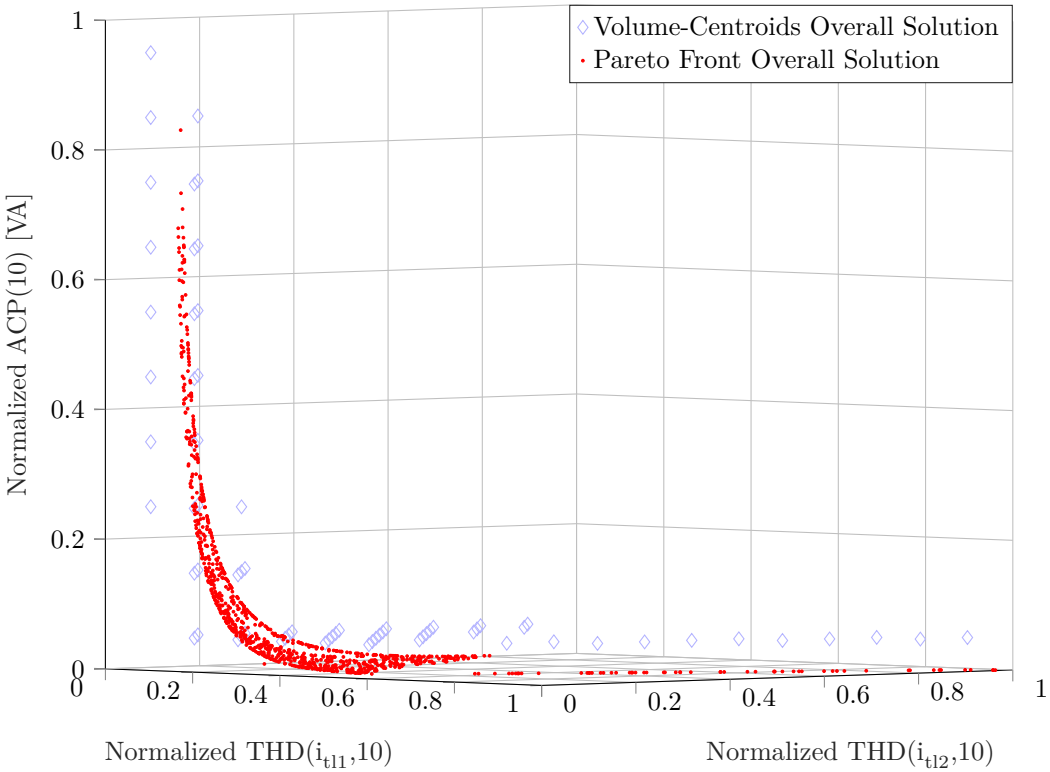

b) Largest grid size, $\delta_m = 1 \times 10^{-1}\,, \forall m.$

Figure 4-5: Overall Pareto Front Solution and centroids of the activated volumes according to AVM.

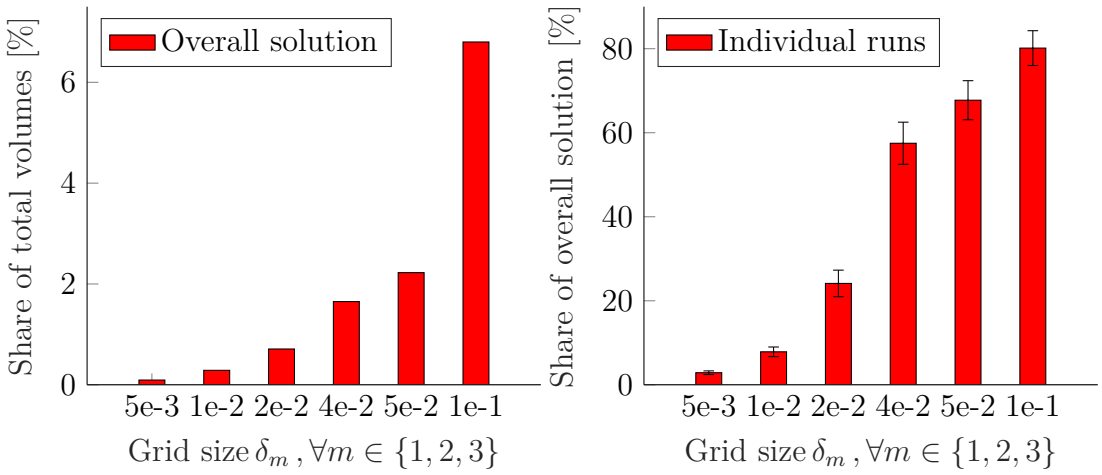

a) Share of overall solution volumes of the total number of volumes.

b) Mean of the share of correctly identified volumes of the overall solution by the individual runs.

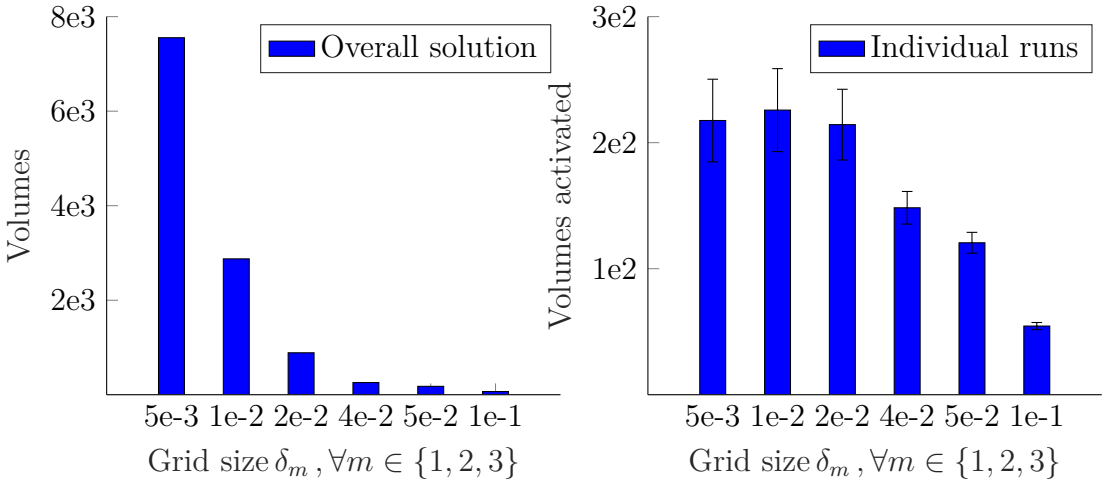

c) Number of volumes covered by the overall solution.

d) Mean of the number of correctly identified volumes of the overall solution by the individual runs.

Figure 4-6: Results of the activated volume method for varying grid sizes.

Table 4-7: The table shows two further aspects of the AVM, related to the grid sizes. The overall solution is denoted by $\mathbf{T}^*$. The 100 solutions from the individual runs are denoted by $\mathbf{T^{100}}$. The meaning of the rows is given below, specified by the first letter in the rows of the first colum. An additional small description is added to the rows, as a reminder.
A) Average of the number of points in an activated volume of $\mathbf{T}^*$.
B) Standard deviation of A).
C) Average of the average number of points in an activated volume from each of $\mathbf{T^{100}}$.
D) Mean of the standard deviation of the average number of points in an activated volume of $\mathbf{T^{100}}$.
E) Percentage of volumes that contain more than 10 points in $\mathbf{T}^*$.
F) Average number of falsely activated volumes by $\mathbf{T^{100}}$, that are not part of the activated volumes in $\mathbf{T}^*$.
G) Standard deviation of F)
H) Percentage of the number of falsely identified volumes of $\mathbf{T^{100}}$ related to the average number of volumes activated by $\mathbf{T^{100}}$.

Grid size δ_m	0.005	0.010	0.020	0.040	0.050	0.100
A) Avg. Nr. of Pts in $\mathbf{T}^*$	2.690	7.067	22.88	78.75	114.1	298.8
B) Std. of A) [%]	123.3	117.2	100.7	93.97	94.03	104.3
C) Avg. of Avg. Nr. of Pts in $\mathbf{T}^{100}$	1.002	1.014	1.124	1.672	2.096	4.664
D) Avg. Std. of C)[%]	2.127	11.12	32.54	63.14	71.58	87.91
E) Vol. with Pts> 10 in ($\mathbf{T}^*$) [%]	2.687	16.63	67.45	85.27	87.08	86.76
F) False Vol. $\mathbf{T^{100}} \notin \mathbf{T}^*$)	41.82	30.28	16.66	6.550	3.040	1.250
G) Std. of F) [%]	18.77	21.76	27.44	36.59	58.75	71.35
H) Share of F) ac. Vol. of $\mathbf{T^{100}}$ [%]	19,22	13.41	7.774	4,416	2.521	2.294

The last part that was analyzed from the results of the AVM is shown in table 4-7. The first part of the table shows the average number of points in the volumes of the overall solution $\mathbf{T}^*$, and the associated standard deviation. The same is shown for the average of the one hundred individual runs indicated by $\mathbf{T^{100}}$. [4] The general tendency is that, with increasing grid size, the average number of points in the volumes increases for the overall solution. The standard deviation is at around 120 % for the first two grid sizes. For the other grid sizes it stays constant at around 100 %. In the volumes of the individual runs, the number of points stays at around 1 for the first three grid sizes, and increases subsequently to 4.466 points per volume for the biggest grid. The standard deviation is increasing with every increase in grid size.

In the second part of the table, the first row shows the percentage of volumes in $\mathbf{T}^*$ that contain more than 10 points. The percentage is at 2.687 % for the smallest grid size and increase to 85.27 % for the fourth. The last three grid sizes have a similar percentage. The next row shows the on average falsely activated volumes of $\mathbf{T^{100}}$, when compared with $\mathbf{T}^*$. The standard deviation is given as well. As the grid size increases, the number of falsely identified volumes decreases. The standard deviation however increases. The share of the falsely identified volumes by the individual runs, when compared with the average number of volumes in the one hundred runs decreases from 19.22 % for the smallest grid size down to 2.294 % for the biggest. This conclude the results of the AVM. The next subsection shows two examples of the controlled system, using a Pareto optimal set point for the controller.

[4] Note that the standard deviation is not the ideal tool for assessing low numbers of points. The number of points cannot become negative!

Table 4-8: The decision variables and cost function values of the controlled systems, shown in figures 4-7 and 4-8.

Desgin	ζ_1	ζ_2	J_1 [%]	J_2 [%]	$\mathbf{J_3}$ [VA]
Set point 1	-4.90499792931779	-4.88661594094842	4.947	5.170	5999
Set point 2	-4.28966593740775	-4.51763888265821	1.484	1.917	330222

4-2-3 Controlled System Simulation

Two different set points were chosen from the PF from the overall solution and are displayed in figure 4-7 and figure 4-7. The set points were chosen heuristically by inspecting the cost function values from the overall solution. The values of the decision variables, and the cost of the three multiobjective optimization cost functions are shown in table 4-8

The first set point was chosen, because THD of the currents on the first and second transmission line, J_1 and J_2 are both at around 5 %, while the ACP is comparatively low with 5999 VA. The second set point was chosen, because both the THD on both transmission lines is very low, at $J_1 = 1.484\%$ and $J_2 = 1.917\%$, even tough the ACP is very high at $J_3 = 330222$ VA. The system behavior of the first set point is shown in figure 4-7, while the behavior of the second set point is shown in figure 4-8.

The general structure of the plots is the same as for the uncontrolled system that was shown in figure 4-1. The last four periods of the simulation are shown. The sub figures a) show the currents on the transmission lines, with i_{tl1} (red, dashed) and i_{tl2} (blue, solid) In addition, the negative control current $-i_{CS}$ (green, solid, dots) is also shown in the plot. The negative value is displayed, to align the control current with the flow on the transmission lines. That way, if the control current has the same sign as the transmission line currents, it acts as a load on the overall system.

Sub figures b) shows the supply voltage V_s (red, solid), the voltage at the point of common coupling 1, V_{PPC1} (blue, solid, dots), and the voltage at the point of common coupling 2, V_{PPC2} (green, dashed). The time development of the currents over linear load 1 i_{L1} (blue, solid), and linear load 2 i_{L2}, are shown in sub figures c). The currents on the feeder to the non–linear distortion 1 i_{F1} and the non–linear distortion 2 i_{F2} are shown in sub figures d).

The most noticeable difference in sub figures a) between the two set points is, that set point 2 achieves twice as much current on transmission line one than set point 1. The negative control current of set point 2 is very sinusoidal itself. The control current of set point 1 is highly non linear itself. In sub figures b) differences in the time development of the supply voltage in comparison to the points of common coupling can be noticed. Voltages V_{PCC1} and V_{PCC2} of set point 1 are basically in phase, which is why V_{PCC1}

Table 4-9: Summary of current and voltages of the controlled systems.

Design	Signal	THD$(-, 10)$	Maximum	rms
Set Point 1	V_s	1.894 %	325.3 V	230.0 V
	V_{PCC1}	3.840 %	279.1 V	198.7 V
	V_{PCC2}	3.849 %	273.7 V	194.5 V
	i_{tl1}	4.947 %	235.1 A	161.9 A
	i_{tl2}	5.170 %	163.1 A	105.7 A
	i_{L1}	1.726 %	54.00 A	38.38 A
	i_{L2}	1.732 %	52.93 A	37.58 A
	i_{F1}	54.05 %	49.53 A	27.10 A
	i_{F2}	53.55 %	48.44 A	26.58 A
	i_{CS}	27.07 %	118.2 A	65.66 A
Set Point 2	V_s	1.894%	325.3 V	230.0 V
	V_{PCC1}	4.062 %	262.2 V	186.0 V
	V_{PCC2}	4.063 %	257.4 V	181.8 V
	i_{tl1}	2.260 %	550.5 A	377.0 A
	i_{tl2}	1.716 %	526.6 A	345.1 A
	i_{L1}	1.995 %	50.69 A	35.94 A
	i_{L2}	2.053 %	49.78 A	35.12 A
	i_{F1}	54.04 %	49.53 A	27.10 A
	i_{F2}	53.54 %	48.45 A	26.59 A
	i_{CS}	5.114 %	511.3 A	325.7 A

is not really visible. They display only a slight delay behind V_s. This changes for set point 2, where both voltages of the points of common coupling are heavily delayed behind V_s. Also, V_{PPC2} is visible, lagging even further behind than V_{PCC1}.

In sub figure c) a slight delay of i_{L2} behind i_{L1} can be observed for set point 2. For set point 1 the behavior doesn't seem to have visually changed in comparison with the uncontrolled system. Differences in the currents on feeder line 1 and 2 in sub figure d) are not observed from the both plots.

A summary of the voltages and currents is given in 4-9. The most important observations will be pointed out. The voltage drop at the PCCs is about 12V higher at the second set point than in the first. The rms of the current on the transmission lines is considerably higher in the second set point than in the first. The current on the linear loads however decreased, when compared with set point 1, while the THD increased. The control current in the set point 1 has a relative high THD with 27 %, while the control current in set point 2 has a THD of 5.114 %. The currents on the feeder lines have changed less than 1 % between the two set points.

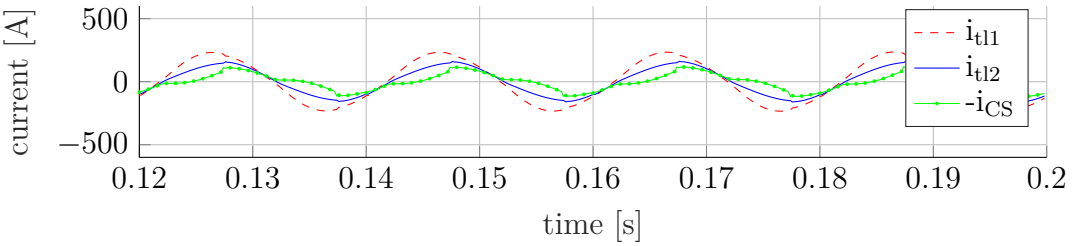

a) Currents on the transmission lines, and the negative control current.

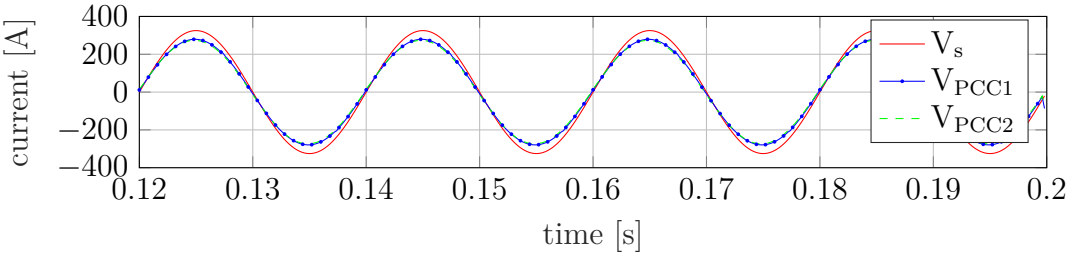

b) Supply voltage and voltages and the PCCs.

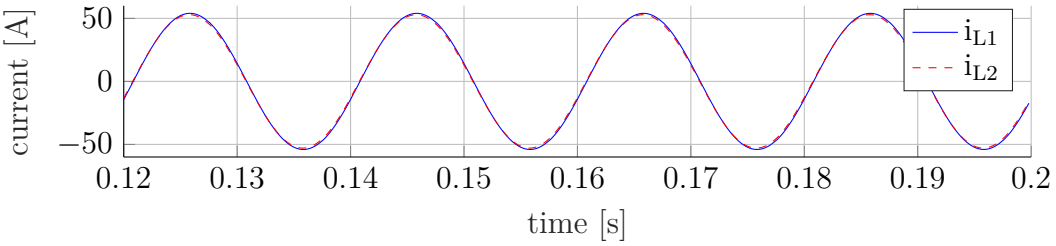

c) Currents over the linear loads.

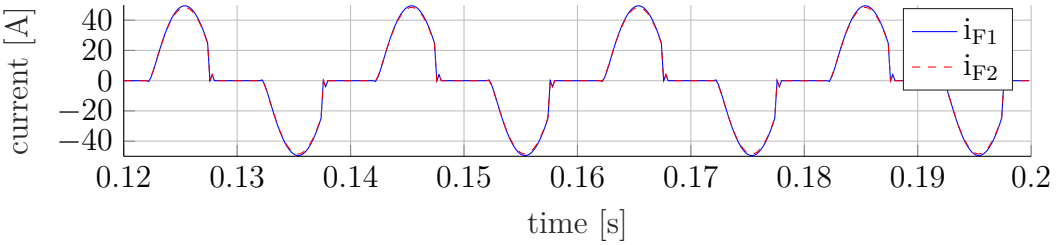

d) Currents over feeder line 1 and feeder line 2.

Figure 4-7: Controlled system Simulation results. Set point 1.

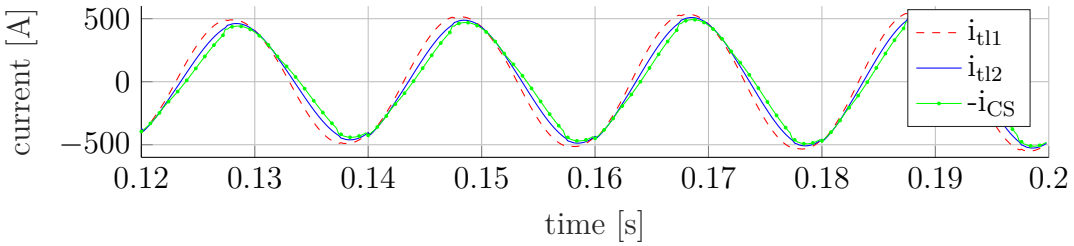

a) Currents on the transmission lines, and the negative control current.

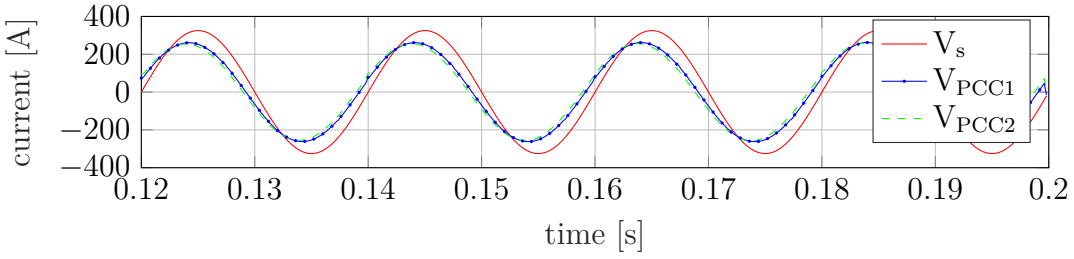

b) Supply voltage and voltages and the PCCs.

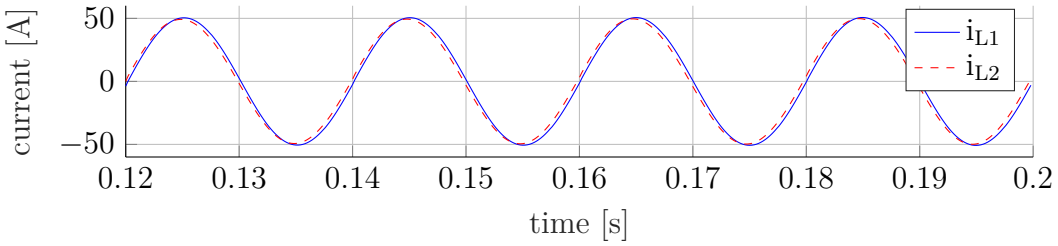

c) Currents over the linear loads.

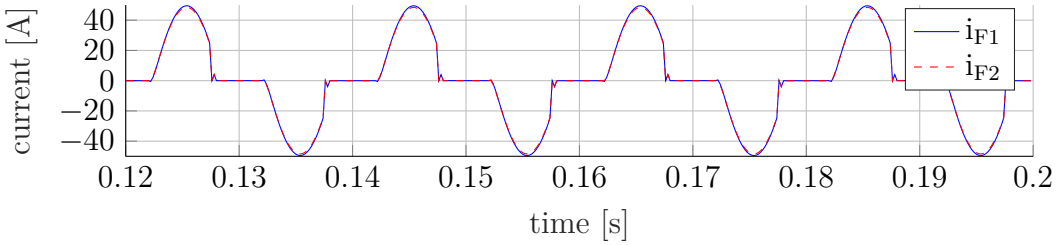

d) Currents over feeder line 1 and feeder line 2.

Figure 4-8: Controlled system Simulation results. Set point 2.

Table 4-10: Controlled System. Apparent power **S**, active power **P**, inductive reactive power **Q** , Phase shift between voltage and current, and the power factor are shown, for transmission line 1 and 2.

Design	**Line**	**S** [VA]	**P** [W]	**Q** [VA]	**Phase shift** [°]	**Power Factor**
Set Point 1	**TL 1**	42115	36118	21660	−30.95	0.8576
	TL 2	20726	14821	14488	−44.35	0.7151
Set Point 2	**TL 1**	81137	44967	67537	−56.34	0.5542
	TL 2	48395	8319	47675	−80.10	0.1719

For set point 1, the phase shift on transmission line 1 is at $-30.95°$ between the supply voltage V_s and the current i_{tl1}. Between V_{PCC1} and i_{tl2} the phase shift is at $-44.35°$. For set point 2 the phase shift on transmission line 1 is at $-56.34°$, and the phase shift on transmission line 2 is at $-80.10°$. The influence on the apparent power, active power, inductive reactive power, and the power factor can further be seen in table 4-10. Notice, that the power flowing on transmission line 1 for set point 2 is almost only inductive reactive power.

4-3 Analysis

This section covers the analysis of the reproducibility assessment in the first subsection, and the analysis of the displayed simulation results in the second.

4-3-1 Reproducibility Assessment

This subsection will cover the analysis of the reproducibility of the PF when using the spMODEx algorithm. The focus will not lie on the absolute usefulness of a given set point for the controller, found by spMODEx, but on whether or not the PF is found reliably.

The first result was given by the histogram shown in figure 4-2. The number of points seem to be normal distributed from looking at the graph. The Chi-square test could not discard the hypothesis at a significance level of 5 %. This was expected, since the search mechanism of DE is of statistical nature, using uniformly random variables to create new individuals. An average number of 259.80 points with a standard deviation of 13.34 % is considered as an acceptable result. Especially when considering, that the number of maximum generation used is with 150 fairly low.

Each point found by one of the individual runs has a chance of 78.21 % of being Pareto optimal, when compared to all solutions found. This can be interpreted as the success

rate of one cycle spMODEx being on average roughly 80 %. It is however not exactly the same, as the real PF is unknown. Therefore it is not known which of these points are truly Pareto optimal.

It seems from this perspective, that the algorithm is suited to find Pareto optimal MPC controller set points, even when convergence time is fairly low. The run time for one cycle of spMODEx was about 3 minutes and 16 seconds, which equals 4530 system simulations. 4500 from the search process itself and 30 from the initialization process. If one system solution would take for example one minute. The PF approximation could be achieved within 1.5 days. As the CPU used for simulation is from a conventional laptop, this seems quite reasonable.

The appearance of the PF is insofar unexpected, as it consists of a line and a convex shell with holes. It was thought, that the front was a convex shell, but holes and the line were not expected. It is however expected, that the maximum Pareto optimal value in the THD of the transmission line current is at about 19 %, as this is about the value of the uncontrolled system. Every value where both THDs are over 19 % while still requiring energy to control the system are worse than the uncontrolled case.

When comparing the three examples of the individual runs with the overall solution, a high degree of similarity is observed. This is confirmed in so far, that the comparison of the average direction vector found no noteworthy difference (about one ten thousands of a degree) in the angle of the eigenvectors of the point clouds. The little difference that is observed is thought to be negligible even while the standard deviation is high in percent. The absolute value is about as low as the difference itself.

An additional observation that can be made from the individual solutions in figure 4-6 is, that more points does not necessarily mean better spread. Even tough the individual solution displayed by green crosses has 329 points , the individual solution containing the least number of points with 195, covers more of the extreme parts of the PF. The holes that can be observed in the overall solution, are covered by the individual solution. Why the holes exist is not fully understood. The explanation for them is, that set points found in that region are generally outperformed by others. This is peculiar, especially when considering that the solution from the individual runs have points in those regions. It is interpreted, that there is an underlying system property, that hinders the controller to feasibly compensate the system in that region.

The results from the AVM need closer inspection and interpretation. First an interpretation of the grid size will be given, and the resulting implications will be discussed there after. The goal of the AVM is to built a pixelated image of the overall solution, an then compare it with the pixelated images of individual runs.

There are two essential pitfalls that need to be avoided. When the grid sizes or pixelation is chosen too high, the representation becomes meaningless. For example, choosing a

grid size of $\delta_m = 0.5\,, \forall m$, will yield only $(\frac{1}{0.5})^m$ volumes, or in this case 8. A difference from the individual solutions could not be observed. On the other hand, choosing a grid sizes so small, that it barely encapsulates one point, will make it impossible to activate this volume again by another point. An individual solution from the results could on average only cover as much as the success rate of being a Pareto optimal point of 78.21 % divided by one hundred runs, from the volumes overall solution. Making the whole endeavor obsolete.

There are two opposing requirements. The first is keeping the grid size big, to allow activation of the reference volumes by the individual solution when points are in close proximity. Secondly, keep the grid size small to prevent activation by individual solutions which are not in close proximity.

To proceed, an interpretation of the pixelation needs to be developed. The grid size can be understood as a percentage of coverage from the overall solution, granting an error in percent. A grid size in all cost of 0.0100, allows one percent of error in identifying the *real* solution. If an individual run activates 80 % of the reference solution at that gird size, it can be concluded, that it correctly found 80 % of the overall solution with an error of 1 %. This can also be translated back to the original solution space, which is shown in table 4-6. For the THD at a grid sizes of 1 %, the original space is pixelated at 0.2000 % intervals. The reproducibilty can be assessed when accepting a margin of error.

The degree of pixelation was examined by the data that is given in table 4-7, where the average number of points in an activated volume are shown. Even for the smallest grid size, more than two points are on average in any given volume of the reference solution. The number of points increases a hundred fold, to the largest grid size. The average number of points in the activated volumes of the one hundred runs stays quasi constant for the first three grid sizes. The increase in standard deviation is a tell, that the number of volumes that contain more then one point becomes more frequent.

If it is to be ensured that a volume contains at least a certain number of points, the standard deviation cannot be used to discriminate between a good or a bad grid size. This is because it is around 100 % for the overall solution. A 99 % confidence interval of 3 sigma always leads to a negative number of points. The percentage of volumes containing at least 10 points is a better measure. For the three biggest grid sizes, this percentage of volumes stays quasi constant at around 85 %. This indicates, that the volumes which contain a lower number of points do so, because they are less explored regions, and not due to the grid size.

Open to debate is, whether the criteria of more than 10 points is justified. The number was chosen heuristically, by trying different numbers. Future research needs to examine, which number a reasonable cutoff is. This could be done by increasing the number of points from 1 in increments of one, and investigate how the percentage of volumes that

contain more "x" points behaves for different grid sizes. Additionally, the coverage of randomly selected points from the overall solution can be investigated. This however goes beyond the scope of this thesis.

Assuming that a number of 10 points is reasonable, the grid size can be selected. The smallest grid size, where the fraction of volumes containing more points is still stable, should be selected. This is the grid size of 4×10^{-2}. The margin of coverage error is thus 4 %. Translated back to the original space, this means 0.8 % error in the THD and 28080 VA in the ACP.

To summarize, at this error the individual solutions span on average over 57.49 % with a standard deviation of 8.725 % of the overall solution, as an approximation for the real PF. The likelihood of each point being Pareto optimal is 78.21 %. Combined with the results from the comparison of the average direction vector (ADV), which found only minuscule differences in the angles of the point clouds, it is assumed that the spMODEx algorithm is a valuable tool for approximating the PFs of an MPC controller.

From practical perspective this can probably be seen as the lower spectrum of the coverage. When calculating the span of the individual solution, the whole space of the overall solution was used as a reference. The volumes which contain less then 10 points probably lie at the extreme points of the PF. They could therefore be excluded, when calculating the coverage of the PF, because the region which can reproduced with reasonable effort is smaller. Additionally, the region of the interest could be reduced further, because extreme points, being very good in some decision variables are usually very bad in others. For a system, where a cost needs to be balanced at a moderate amount, extreme values are usually not meaningful.

More research is however needed to study this. In that study the cut-off in the number of points contained by a volume which is disregarded should be settled first. Next the smallest possible grid sizes should be identified. Afterwards, the spread of the solutions can be analyzed, by varying the grid for only one cost function. This can give insight about in which direction the cost function coverage is influenced strongest. If enough information is gathered, the AVM could eventually be used to determine, whether or not the final solution of a PF is found. By final is meant, when the search algorithm ceases to find new solution. The AVM can thus also be applied stagnation detection method in evolutionary algorithms (EAs).

This concludes the analysis of the reproducibility assessment. The next subsection will analyze the simulation outcomes for the controlled and the uncontrolled system.

4-3-2 Analysis of the Simulation Results

This subsection will cover analysis of the simulation results, and their connection to multiobjective optimization. The results will be analyzed in terms of what can be learned

for subsequent use in the following experiment, to achieve a well posed multiobjective problem (MOP).

The Pareto optimization was not specifically designed to find useful controller set points. It was designed to create a high number of solutions in a short amount of time, while the meaning of the results is grounded in an electrical system. Therefore only two of the states were controlled, in addition to a relatively low sampling time. This allowed a very fast solution of the least square problem posed in 2-83 to produce a high number of Pareto optimal solution in a short amount of time. This does not necessarily mean, that the PFs are not useful. The information can be used to develop a better understanding of what needs to be paid attention to, when posing the next MOP.

The results of the simulation for the uncontrolled, and for the controlled system show, that the MPC controller is capable of compensating the harmonics in a complex electrical system. The controlled simulations, shown in figures 4-7 and 4-8 are in no way representative for all solutions in the PF, as they were chosen heuristically by inspecting the raw data.

They compensation is realized by the this first set point in figure 4-7, by adding an extra oscillating current on the transmission line. The additional current acts as a reactive load, increasing the reactive power on transmission line 1 from 8243 VA for the uncontrolled case to 21660 VA in the controlled. The active power only increases from 36103W by a mere 15W to 36188W. While this does lead to a drop in the power factor, and an increases in the phase shift, the strategy effectively works and compensates both transmission lines to around 5 % THD. The ACP of the controller is relatively low with 5999 VA.

The second set point solves the same problem, with the same strategy, just more extreme. With an exceptionally high control effort of 330222 VA, the THDs can be decreased to 1.484 % and 1,917 %. The active power flowing on transmission line 1 increases to 44967W, while reactive power reaches 67537 VA. The power factor drastically decreases to 0.5542 and is accompanied by an increase in the phase shift to $-56.34°$. The voltages at the PCCs lag behind (not measured) and currents to the linear loads actually decrease, due to the extra load of the controller. When voltage drops at the PCCs, linear loads will thus be supplied with less current. From a system perspective the price that is paid for the exceptionally low THD is too high. For the voltage source, because it is forced to supply high amounts of reactive power, which is not converted to useful work. For the controller, as it needs to expend high amounts of apparent power, which actually tops all loads in the system approximately 9 times, when compared with the uncontrolled case.

Several lessons can be extracted already. The first is, that more data is needed about the system, to discern between useful and not so useful set points. Since in this case individual simulation time is quite low, all set points could be resimulated and evaluated

by additional cost functions. This is however not always possible, when simulation time is high, or the calculation of a set point is the bottle neck, as it is the case for the MPC controller used here. Additional cost functions are needed, to measure meaningful system properties while the optimization process is running. From experience, new cost functions need to be introduced with care, as the controller will sometimes act unexpectedly, even tough it completely satisfies the cost function.

It has also become evident, that simply choosing set points by manual inspection is not ideal. A decision making process is necessary, to analyze the data and discriminate between good and bad set points. This strategy should not simply simply inspect the smallest cost function values. It should first prune solutions from the PF, that are not useful from an engineering perceptive. Engineering problems usually have to fulfill constraints which are given by nature or regulation. These limits and regulations are is what is meant by good or bad. The process could of course be readily implemented in the optimization process itself. This however runs into the danger of over–constraining the search process, preventing the algorithm from finding the best solutions. The decision making process should be done after a relative unconstrained search process.

Next, the controller is in general capable of controlling a complex system. In the examples shown, this is achieved by adding reactive load to the system. In the case of the second set point clearly an overcompensation occurred. The control effort was very high, while straining the system in terms of efficiency (power factor). In the example of this thesis, the controller is only supposed to compensate non–linear loads. To compensate a non–linear load, the compensator should provide a non–linear load itself. Therefor, to avoid over compensation, an additional cost function is created for the next experiment, that penalizes the reciprocal of the THD of the compensation source (CS)current. Low THD of the controller current will thus automatically lead to a high cost function value.

For the voltage supply, a high active power factor, and a low amount of reactive power is desirable. The phase shift between voltage V_s and the current i_{tl1} needs to be decreased. However, a negative phase shift is smaller then zero, and the phase shift alone is not enough. The absolute angle could be used, but the meaning is not so straight forward. A other option is, to use the reactive power factor which indicates. It is calculated, by applying the sine function to the phase shift, and taking the absolute value. This has the additional benefit of penalizing inductive reactive power, and capacitive reactive power at the same time.

The next observation from the results is, that it is unknown whether or not the controller is actually capable of supplying active power to the system. A design alternative is desirable, allowing the controller to provide better electrical power quality (PQ) services to the grid. If the controller is capable of supplying the distortions directly, their effects will ceases for the voltage source, decreasing the THD at the same time. An additional

cost function that minimizes the current on transmission line 1 will be introduced in the next experiment.

Recalling the PF from the overall solution shown in figure 4-3. The general shape of the front was expected. What was unexpected was the disjointed straight line, and the holes in the convex shell, combined with the sharp outlines of the PF. As the ACP is very low for the solution on the straight line, it is assumed that these solution result from set points, where the controller is highly constrained in the control effort. This hypothesis was partly confirmed by inspecting the raw data, as solution with a THD at that level mostly had low ACP. A further deeper analysis should be able to reconcile this observation, but was not made yet, as the immediate benefit was not obvious.

It was observed from the individual solutions, that the holes were indeed covered by points. They were however pruned, when compared with all other solutions. This is evidence, that the controller is capable of compensating in these regions. But given enough time, the search algorithm finds solutions that achieve the same compensation with less energy, which is in general good. This could indicate three things

The first is that the electrical system combined with the MPC controller is in incapable of reaching these regions in a Pareto optimal way. This is doubted in so far, as the MPC is unconstrained and should be capable of exploring most regions, regardless how close to reality the input current is. The second option is, that the search process would eventually find solutions, but didn't have enough time. This is discarded because solutions have been found before in that region. The overall solution most likely covers all what the controller in this configuration is capable.

The last option is, that the controller is constrained internally, and needs more freedom to fully explore the system. Up until now, only 2 of 7 possible states were used for the controller tuning, and five more are available. However, without changing the controller design, full freedom over all states should be avoided, because of the LSSSMPC strategy that is used. Every state, that the controller has access to in the MPC cost function will be penalized on the sinusoidability of the state. But the sinusoidal shape would be counterproductive for most of the states, but the currents flowing over the linear loads..

To test the hypothesis of the controller restriction, the experiment above should be repeated, in order to clarify whether or not the holes are still present in the PF when the controller has more freedom. This however has to be left for future research. The lesson for the second experiment is that the controller should be provided with as much freedom as possible. Thus the states i_{L1} and i_{L1} will be made available to the MPC cost function. The final lesson for the decision making is that tuning parameters, which compensate one of the cost functions exceptionally well are usually found at the outer extremes of the PF, and are probably unfeasible. This was partly expected, but the magnitude of this effect has now become clear. Set points found at such extremes should generally treated with care in the decision making process.

Chapter 5

Experiment 2: Controller Tuning and Decision Making Process

In this chapter the results and analysis of the controller tuning with the four mode switched system, and the decision making process are presented. Section one shows the simulation parameters of the model and the spMODEx algorithm. Section two presents the simulation results, while section three covers the analysis.

5-1 Simulation Parameters, Control– and Tuning–Strategy

The continuous state space models of the four mode switched system and the controller model were discretized using the zero order hold and a sampling time of $t_s = 80\mu s$. The state space models of the four mode switched system [1] were used to simulate the plant. The calculation of the optimal input sequence was done using the controller model[2] of the plant.

The parameters of the resistances and inductances did not change in between the first and the second experiment. The first set of parameters was already shown in 4-1, and will not be shown again. The remaining parameters are given in table 5-1. The capacitors were parametrized so that the voltage drop over half of one period of the grid frequency is a maximum of 1 % in the disconnected case.

Table 5-1: Resistances and capacitance that are additionally used in the four mode switched system. The remaining parameters are shown in table 4-1.

Name	**Parameter 1**	**Value**	**Parameter 2**	**Value**
Distortion 1	R_{13}	10 Ω	C_1	9.950×10^{-2} F
Line resistance **D1**	R_{11}	1.00 Ω		
Distortion 2	R_{14}	10 Ω	C_2	9.950×10^{-2} F
Line resistance **D2**	R_{12}	1.00 Ω		

The additional parameters for the simulation of the electrical circuit are given in table 5-2. The ideal voltage sources V_s supplies an AC voltage of 230V at 50Hz. The initial states of the system were set to steady state behavior at the beginning of a period of the voltage source from the uncompensated four mode switched system. The prediction horizon $\check{H}_p$ and the control horizon $\check{H}_u$ were set two periods. Therefor $\check{H}_p = \check{H}_u = 500$, since the sampling time is 250 samples per period. The periodic receding horizon strategy is employed. Calculating the optimal input sequence a new for each period.

The parameters of the spMODEx algorithm are shown in table 5-3. The recombination type of the Differential Evolution (DE) algorithm is set to binomial, with a crossover rate of 0.9. The high crossover rate induces a recombination behavior which is very similar to lineal recombination. At the same time some binomial recombination is

[1] Given by $\mathbf{A^B}$ $\mathbf{B_t^B}$, $\mathbf{C^B}$, $\mathbf{D^B}$; $\mathbf{A^N}$ $\mathbf{B_t^N}$, $\mathbf{C^N}$, $\mathbf{D^N}$; $\mathbf{A^{C1}}$ $\mathbf{B_t^{C1}}$, $\mathbf{C^{C1}}$, $\mathbf{D^{C2}}$; $\mathbf{A^{C2}}$ $\mathbf{B_t^{C2}}$, $\mathbf{C^{C2}}$, $\mathbf{D^{C2}}$.
[2] Given by $\mathbf{A^C}$ $\mathbf{B_t^C}$, $\mathbf{C^C}$, $\mathbf{D^C}$.

Table 5-2: General simulation parameters of the four mode switched system and the controller model.

Parameter	Magnitude	Description
f	50 Hz	Grid frequency
t_s	80 µs	Sampling time
Periods	10	Number of periods simulated
max V_s	$\sqrt{2}\,230$V	Supply voltage amplitude
$\check{H}_p$	500	Prediction horizon
$\check{H}_u$	500	Control horizon

possible, which allows more exploration in the decision variable space. The maximum generation is 170. With a population size of 60 individuals per generation a total of 10260 different controller set points are explored. The number of the arc increments β^ϵ of the spherical pruning mechanism was set to 100. The number of decision variables used in the spMODEx algorithm is four. The number of cost functions used is six.

The multiobjective cost functions used are the total harmonic distortion (THD) of the currents i_{tl1} and i_{tl2}, the rms of the Apparent Control Power (ACP) for balancing the systemfor the last period, the reciprocal of the THD of the compensation source (CS) current, the reactive power factor on transmission line 1, and the rms of the current on transmission line 1, all measured in the last period. For further details on the measurements of the cost functions see section 3-3.

In detail, the six cost functions with which an individual i during the multiobjective optimization is evaluated, are $\mathbf{J}(\zeta^i) = [J_1(\zeta^i), J_2(\zeta^i), J_3(\zeta^i), J_4(\zeta^i), J_5(\zeta^i), J_6(\zeta^i)]$ with,

$$J_1(\zeta^i) = \quad \mathrm{THD}(i_{tl1}, 10)\,, \tag{5-1}$$
$$J_2(\zeta^i) = \quad \mathrm{THD}(i_{tl2}, 10)\,, \tag{5-2}$$
$$J_3(\zeta^i) = \mathrm{ACP}(i_{CS}, v_{CS}, 10)\,, \tag{5-3}$$
$$J_4(\zeta^i) = \quad \frac{1}{\mathrm{THD}(i_{CS}, 10)}\,, \tag{5-4}$$
$$J_5(\zeta^i) = \mathrm{QPF}(v_s, i_{CS}, 10)\,, \tag{5-5}$$
$$J_6(\zeta^i) = \quad \mathrm{RMS}(i_{tl1}, 10)\,. \tag{5-6}$$

The states are controlled using the linear state signal shaping model predictive control (LSSSMPC) control strategy. The four states, i_{tl1}, i_{tl2}, i_{L1}, and i_{L2} are targeted by the

Table 5-3: Parameters of the spMODEx algorithm.

Parameter Description	**Value/Type**
Recombination type of DE algorithm	binomial
Maximum generation $\check{G}$	170
Number of cost functions $\check{m}$ in $\mathbf{J}(\zeta)$	6
Number of decision variables $\check{j}$ in ζ	4
Number of individual $\check{i}$ in search population	60
Total number of function evaluations	10260
Lower bound $\tilde{b}_L$ of decision variables ζ	-29
Upper bound $\tilde{b}_U$ of decision variables ζ	29
Spherical pruning strategy	enabled
Number of arcs β^{ϵ} in spherical grid	100
Norm applyed during spherical pruning	euclidean
Scaling factor F	0.1
Crossover Factor C_r	0.9

sinusoidal sub weighting matrices of the states $\mathbf{S_{Q,1}}$, $\mathbf{S_{Q,2}}$, $\mathbf{S_{Q,3}}$, and $\mathbf{S_{Q,4}}$. With the last controlled state as $n_x = 4$, the dimensions of the matrices follow as $\mathbb{R}^{(1988\times3500)}$. For the sub weighting matrix $\mathbf{S_{R,t}}$ of the control input the dimensions are $\in \mathbb{R}^{(500\times500)}$ as the identity matrix. The factor f_R for the input sub weighting matrix is $f_R = 1$. The relationship between decision variables and the factors f_1, f_2, f_3, and f_4 is given by

$$f_1 = 10^{\zeta_1}\,, f_2 = 10^{\zeta_2}\,, f_3 = 10^{\zeta_3}\,, f_4 = 10^{\zeta_4}\,. \tag{5-7}$$

For more details on the connection of the controller to the optimization algorithm refer to section 3-2.

5-2 Simulation Results

This section presents the simulation results of the second experiment. In the first subsection the decision making process is presented. In the second subsection an additionally identified controller set point is shown.

5-2-1 Decision Making Process

The multiobjective optimization was run on an "Intel i5-8250U" CPU, employing MATLAB Parallel Computing Toolbox. The spMODEx algorithm terminated after around 1 hour and 50 minutes, with a Pareto Front (PF) containing 476 solutions. The PF is visualized with the help of level diagrams and is shown in figure 5-1, in six sub figures. The THD of the currents on the transmission lines 1 and 2 are given in sub figures a) and b). The ACP is given in sub figure c), followed by the reciprocal of the THD of the CS current in d). The last two figures show the reactive power factor in e), and the root mean square (rms) current on the on transmission line 1 in f).

The minimal normalized euclidean distance is at $\| \iota \|_2 = 0.2056$, and the maximum at $\| \iota \|_2 = 1.489$. The maximal value that could have been achieved in the normalized distance is $\sqrt{\check{m}} = \sqrt{6} = 2.450$. There are some general observations, that can be made to a certain degree in every sub figure. The points tend to cluster in certain regions, where the cost function value on the x–axis stays more or less constant, while the normalized distance increases drastically. The regions itself tend to be at the lower end of the cost function values. A second observation is, that when cost function values increase fastest, normalized distance increase less. Many of the points seem to additionally be located on imaginary lines that function like barriers. They seem to prevent solutions to be found below or above them.

In sub figure a), the level diagram of the first cost function $J_1 = \mathrm{THD}(i_{tl1}, 10)$ is shown. The lowest THD is 0.6922 %, while the highest is at 18.75 %. Minimum and maximum value for $\| \iota \|_2$ both appear around 1-2 % THD. There is a more pronounced solution cluster around 2 % THD and $\| \iota \|_2 \approx 0.7$, from where three "lines" spread out. The first reduces $\| \iota \|_2$, without increasing THD. The second line increases somewhat in the THD, while the third increases the most. All lines lead up to the barrier line, in which THD increases strongly while $\| \iota \|_2$ does so moderately.

Sub figure b) shows the level diagram of cost function $J_2 = \mathrm{THD}(i_{tl2}, 10)$. The first observation is, that the cost function values are very compressed. This is because the maximum value is at $J_2 = 133.5\,\%$. The rest of the point cloud is in the range between 0.6838 % and 21.89 % in the THD. An additional figure is given in appendix figure A-1, that shows the cost function values without the extreme point. The figure shows that

the development is in so far different from the other cost functions, that an increasing cost in J_2 actually leads to a decrease in the normalized distance $\| \iota \|_2$.

Sub figures c) to f) follow a similar structure as sub figure a). In c) the ACP is given, with its minimum at $J_3 = 416.5\,\text{VA}$ and the maximum at $J_3 = 5.298 \times 10^6\,\text{VA}$. Note that the values mostly cluster around $0.2 \times 10^6\,\text{VA}$ or lower. The reciprocal of the THD of the CS current is shown in d) with its minimum at $J_4 = 1.229 \times 10^{-2}$ and the maximum at $J_4 = 148.7$. The reactive power factor is shown in e), with its minimum at $J_5 = 1981 \times 10^{-3}$ and its maximum at $J_5 = 0.9130$. The rms on transmission line 1 as the last cost function is given in f) with the minimum at $J_6 = 72.95\,\text{A}$ and the maximum current at $J_6 = 1.821 \times 10^3\,\text{A}$.

The original PF was pruned after the following criteria. Points that had a higher THD than $J_1 > \text{THD}(i_{tl1}, 10) = 5\,\%$ were deleted. This is in accordance to the guidelines

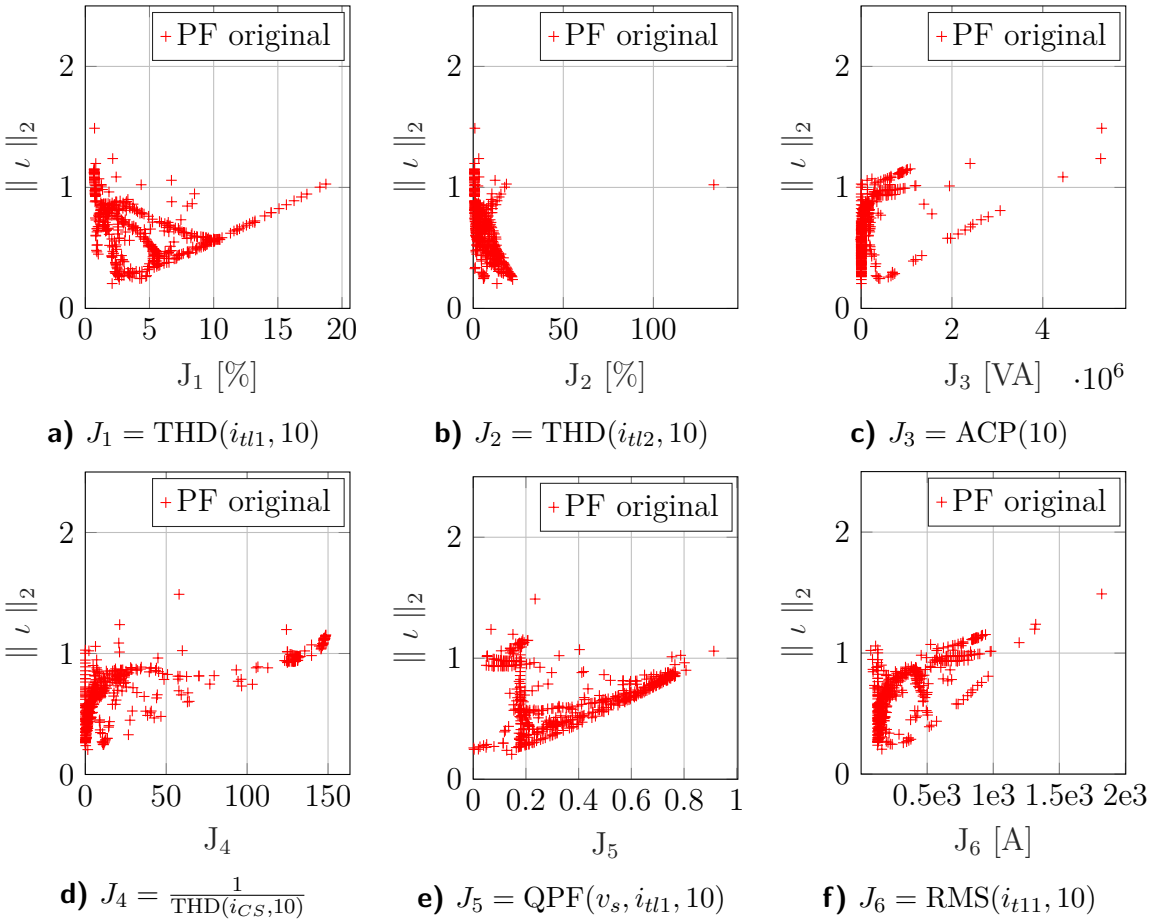

a) $J_1 = \text{THD}(i_{tl1}, 10)$ **b)** $J_2 = \text{THD}(i_{tl2}, 10)$ **c)** $J_3 = \text{ACP}(10)$

d) $J_4 = \frac{1}{\text{THD}(i_{CS}, 10)}$ **e)** $J_5 = \text{QPF}(v_s, i_{tl1}, 10)$ **f)** $J_6 = \text{RMS}(i_{t11}, 10)$

Figure 5-1: Level Diagrams of the unpruned Pareto Front after the multiobjective optimization.

on THD of currents published at, [8]. Solutions with that needed a ACP higher than $J_3 > \text{ACP}(10) = 8 \times 10^4\,\text{VA}$ were discarded as well. A solution should need at a maximum twice the amount of energy, that is already flowing in the system, which is still very high. For the control current the minimum value of 10 % THD was acceptable. Considering the reciprocal, this means all values above $J_4 > \frac{1}{\text{THD}(i_{CS}10)} = 10$ were deleted. The last bound was given for the rms current on transmission line 1. All values with a with $J_6 > \text{RMS}(i_{tl1}, 10) = 250\text{A}$ were discarded. This still allows a two fold increase in the rms of the current on transmission line 1 (TL1) when compared to the uncontrolled system.

This yielded the PF which is shown in the level diagrams of figure 5-2. A total number of 96 solutions remained after the pruning. The immediate difference that can be observed, that the spread over the y–axis changed. The minimum value for the normalized

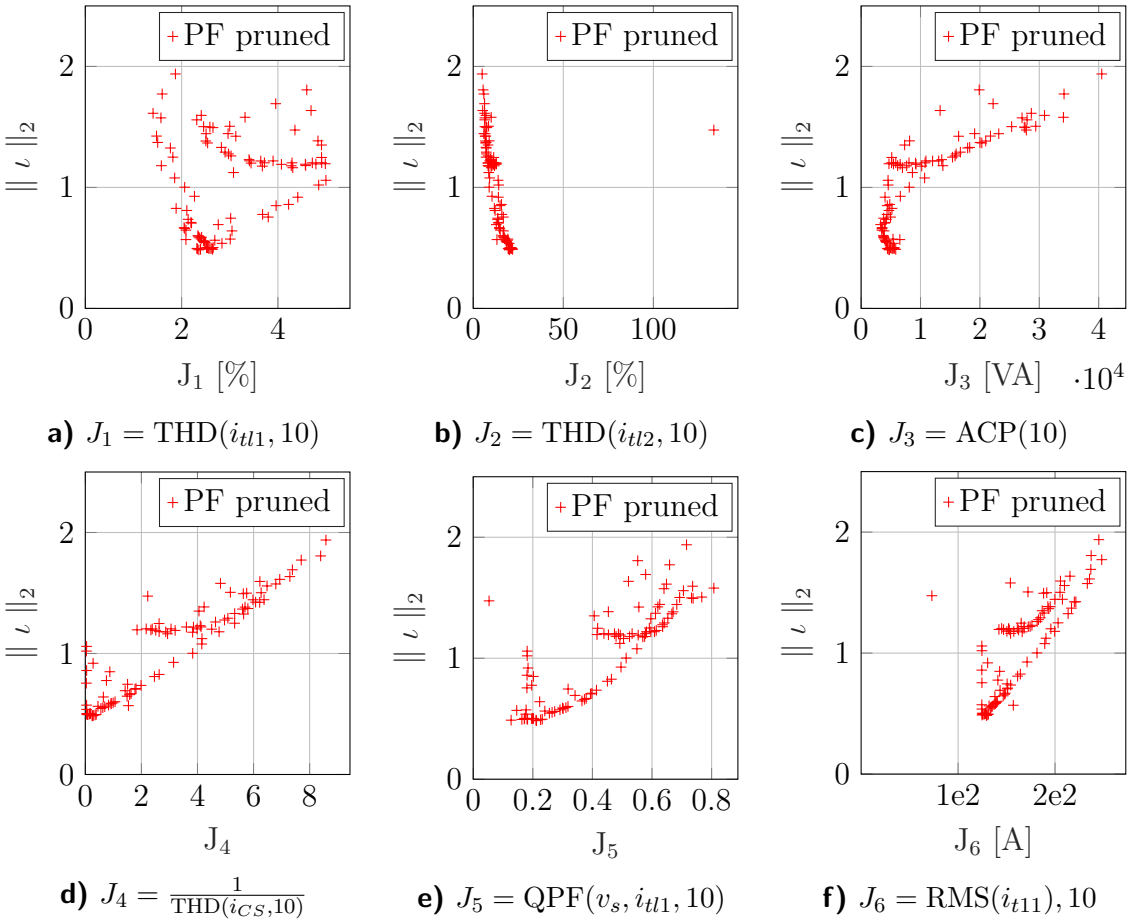

a) $J_1 = \text{THD}(i_{tl1}, 10)$ **b)** $J_2 = \text{THD}(i_{tl2}, 10)$ **c)** $J_3 = \text{ACP}(10)$

d) $J_4 = \frac{1}{\text{THD}(i_{CS},10)}$ **e)** $J_5 = \text{QPF}(v_s, i_{tl1}, 10)$ **f)** $J_6 = \text{RMS}(i_{t11}), 10$

Figure 5-2: Level Diagrams of the pruned Pareto Front after the multiobjective optimization.

distance increased to $\| \iota \|_2 = 0.4842$, and the maximum increased to $\| \iota \|_2 = 1.938$. The reason for this is the calculation method for $\| \iota_g \|_2$ of each individual, referring the individual value to the minimum and maximum value of the population.

The minimum and maximum values of the first cost function changed to $J_1 = 1.407\,\%$ and $J_1 = 4.997\,\%$, respectively, in a). For the THD on transmission line the minimum changed to $J_2 = 4.976\,\%$. The boundary of the cluster and the maximum are unchanged at $J_2 = 21.89\,\%$ and $J_2 = 133.5\,\%$, respectively, in b). For the ACP the minimum changed to $J_3 = 3.288 \times 10^3\,\mathrm{VA}$ and the maximum to $J_3 = 4.052 \times 10^4\,\mathrm{VA}$, in c). The new minimum and maximum values of the fourth cost function are given by $J_4 = 3.821 \times 10^{-2}$ and $J_4 = 8.580$, in d). For the reactive power factor minimum and maximum changed to $J_5 = 5.323 \times 10^{-2}$ and $J_6 = 0.8075$, in e). The minimal boundary of the rms current on transmission line 1 is unchanged at $J_6 = 72.95\,\mathrm{A}$, while the maximum reduced to $J_6 = 248.1\,\mathrm{A}$, in f).

The reduction in points did not fundamentally change general structure of the plots. However, the clustering at low cost function values is considerably reduced. The detailed plot without the extreme point of cost function J_2 shown in appendix A-1. The figure now clearly displays a decreasing relationship in $\| \iota_g \|_2$ when J_2 increases. This is the opposite behavior, to what is observed for the other cost functions.

Eight points are selected for the stability analysis. From the cost functions the set points that achieved the minimum value in J_m were chosen. Additionally, the set points with the lowest $\| \iota_g \|_2$ from the pruned PF, and from the original PF, as a reference, are chosen. They were simulated for 500 periods, equaling 10s worth of simulation time. The rms currents on transmission line 1 were compared. A set point is discarded, when

$$\frac{\mathrm{RMS}(i_{itl1}, 500)}{\mathrm{RMS}(i_{itl1}, 10)} > 1.1 \tag{5-8}$$

is true. Three set points remained. These are the set point achieving the lowest $\| \iota_g \|_2$ from the pruned PF, the set point with the lowest ACP (J_3), and the set point with the lowest reciprocal value of the THD of the control current J_4.

The three stable set points, and the uncontrolled system were simulated for ten periods, as was done during the multiobjective optimization. The decision variables of the stable set points set point 1 (SP1) to set point 3 (SP3) are shown in the annex in table A-1. The most important results are given in table 5-4. The table is split in three blocks. In the first two, the rms and THD measurement for the most important voltages and currents of the system are given. The third block shows the power measurements at TL1 and at the compensation source. A detailed description of abbreviations used in the following is detailed out over the table. As the uncontrolled and the controlled system generally exhibit a behavior similar to what was already shown in the first experiment,

the result presentation will only be focus on the most important features regarding the choice of the best set point.

The first important feature that, is that two new measurement variables are add, namely V_{C1}, and V_{C2}. These are the voltages that were introduced as new states to the four mode switched system, and are part of the source of the non–linear current demand on the system. In the uncontrolled case their rms voltages are at 180.8V and 177.8V, respectively. They are shown in the first block of the table, that shows the rms voltages and currents in the four different cases.

Looking at the first block of the table, where rms values are displayed, only small differences can be observed between the set points, partly even when compared with the uncontrolled system. The uncontrolled system actually fairs best, with regards to the rms of voltage at the point of common couplings (PCCs) and is on par for the currents to the linear loads i_{L1} and i_{L2}. The non–linear loads, fed by the currents over the feeder lines, i_{F1}, and i_{F2} achieve similar or higher currents in the controlled cases. The third set point, SP3, achieves overall the best results, having the highest currents to the loads, while achieving the lowest values for the currents on the transmission lines, even lower than in the uncontrolled case. The least amount of control current i_{CS} is needed. The set point set point 2 (SP2) displays generally the lowest values for the voltages at the PCC, and currents to linear and non–linear loads. The currents flowing on the transmission lines are however the highest, while requiring high amounts of CS current. Intermediate results are achieved by SP2 varying in voltages and currents in between the other set points.

Regarding the second block where the THD is given for currents and voltages the following can be observed. For the uncontrolled system, the THDs of the voltages at the PCCs and on the linear loads, are around 3 % or lower. However the transmission lines experience high THD with 18.84 % on current i_{tl1} and 18.68 % on current i_{tl2}. The lowest value of the THD for i_{tl1} is achieved by SP1 with 2.358 % and the highest by SP3 with 3.800 %. In all controlled cases the currents to the linear loads exhibit a THD below 0.9000 %. The voltages at the PCCs around 1.8 % THD, grouping at very similar values. The THD of the currents on the feeder lines are around 55 %, and of the compensation source i_{CS} between roughly 70 % and 2600 %.

The last block of the table shows the power that is flowing over transmission line 1, and the power that is provided by the compensation source. The uncontrolled system, and the controlled system display similar power on transmission line 1 around 36000 VA. SP3 achieves the overall lowest power with 35007 VA and the highest power factor of 0.9836 for the controlled cases. The highest amount of apparent power flows for SP2 with 38933 VA coupled with the overall lowest power factor 0.9398. The apparent power coming from the compensation is the lowest for SP2 with 3289 VA consisting mainly of reactive power, as is also reflected by the low power factor of 0.2090. The highest

Table 5-4: Summary of the Simulations of the different set points, as an outcome of the decision making, and the uncontrolled system is given. The uncontrolled system (UCS), set point 1 (SP1) where $\| \iota_g \|_2$ is minimal, set point 2 (SP2) where $J_3 = \text{ACP}(10)$ was minimal, and set point 3 (SP3) where J_4 as the reciprocal of the THD$(i_{CS}, 10)$ is minimal. All shown measurements were taken at the last period of the simulation (period $= 10$). The first block of rows shows the rms of current and voltages, and the next block the THD. In the last block the apparent power **S**, reactive power **Q**, and active power **P** are shown for transmission line 1 (TL1) and the compensation source (CS). The power factor is given by $\cos\varphi$, and the phase shift is given by φ.

Measurement	**Variable**	**UCS**	**SP1**	**SP2**	**SP3**
RMS of voltages [V]	V_s	230.0	230.0	230.0	230.0
	V_{PCC1}	204.6	203.6	201.7	204.5
	V_{PCC2}	201.5	200.3	197.9	201.5
	V_{C1}	180.8	181.0	180.2	181.2
	V_{C2}	177.8	178.1	177.1	178.4
RMS of currents [A]	i_{tl1}	126.6	129.5	143.3	124.6
	i_{tl2}	62.77	68.00	83.99	62.25
	i_{L1}	39.30	39.13	38.75	39.30
	i_{L2}	38.72	38.49	38.03	38.71
	i_{F1}	26.86	27.53	26.86	27.66
	i_{F2}	26.36	27.16	26.32	27.39
	i_{CS}	-	27.47	40.47	23.47
THD of Voltages [%]	V_s	0.7478	0.7478	0.7478	0.7478
	V_{PCC1}	2,793	1,701	1,659	1,751
	V_{PCC2}	3,082	1,827	1,718	1,816
THD of currents [%]	i_{tl1}	18,84	2,358	2,762	3,800
	i_{tl2}	18.68	20.06	12.79	16.74
	i_{L1}	1,707	0,7109	0,6781	0,6660
	i_{L2}	1,941	0,8366	0,7276	0,6870
	i_{F1}	52.34	55.35	55.40	55.30
	i_{F2}	51.93	56.59	56.50	55.70
	i_{CS}	-	393.4	70.38	2617
Location	**Variable**	**UCS**	**SP1**	**SP2**	**SP3**
TL 1	**S** [VA]	37126	35903	38933	35007
	Q [VA]	6667	7625	13305	6310
	P [W]	36523	35084	36589	34434
	$\cos(\varphi)$	0.9837	0.9772	0.9398	0.9836
	$\varphi[^\circ]$	-10.34	-12.26	-19.98	-10.38
CS	**S** [VA]	-	4718	3289	4958
	Q [VA]	-	1328	3216	1275
	P [W]	-	4527	687,3	4792
	$\cos(\varphi)$	-	0,9596	0,2090	0,9664
	φ [°]	-	163,7	102,1	165,1

apparent power is needed by set point SP3 with 4958 VA combined with a high power factor of 0.9664.

All things considered, set point SP3 was found to be the best choice of the three options, the reasoning can be found in the analysis part. In the following, the time development of the system is shown here for SP3, as the final result of the decision making. The simulation visualization for the uncontrolled system, as well as for SP1 and SP2 are not shown here. The can however be found in the appendix for completion.

Figure 5-3 follows the same structure, as the system simulations that were shown in experiment one. The last four periods of the ten period simulation time are shown. Sub figure a) shows the currents i_{tl1}, and i_{tl2} on the transmission lines, and the negative compensation source current $-i_{CS}$ provided by the compensation source. Sub figure b) shows the supply voltage V_s, and the voltages V_{PCC1}, and V_{PCC2} at the PCCs. Sub figure c) shows the linear load currents i_{L1}, and i_{L2}, while sub figure d) shows the non–linear currents that flow on the feeder lines i_{F1}, and i_{F2}, which are drawn from the non–linear loads. The last plot in sub figure d) is a new addition. Here the voltage levels V_{C1}, and V_{C2} over the capacitors is shown. The most important observations will be pointed out.

The negative CS current in sub figure a) follows at the beginning of the first displayed period a sinusoidal form. The sign of the current is in the same direction, as the currents on the transmission lines, being a load current of 34.73A maximum. With the onset of the non–linear loads, see d), the CS current decreases in magnitude and eventually reverses its sign, indicating a supply current, reaching it's maximum at 31.73 A. The current i_{tl1} displays a completely sinusoidal shape, while i_{tl2} becomes highly distorted and plateauing in the mean time. As the non–linear load current in d) decreases, so does the supplied CS current. The sudden decrease in non–linear load current is mirrored by $-i_{CS}$ with a sudden increase as a load current to 48.38 A. The sudden load change is reflected in the currents on the transmission lines, but can also be observed in the voltages V_{PCC1}, and V_{PCC2} in b). After this point, $-i_{CS}$ and the current on transmission line 2 (TL2), return to a sinusoidal form. The described behavior is reversed for the negative half of the period, and repeats itself in all periods.

The linear load currents display a perfect sinusoidal shape for all periods shown. It can however be observed, that the are lagging behind the voltages of V_{PCC1}, and V_{PCC2}. The voltages at the PCCs do not seem to be lagging behind the supply voltage V_s. Their magnitude is however considerably decreased, which is also reflected in the rms voltages shown in table 5-4. The voltages V_{C1}, and V_{C2} over the capacitors display a quasi constant voltage, oscillating around a mean value given in table 5-4. This is a typical behavior of an RC-circuit that is connected and disconnected from a supply source. The rms voltage of V_{C2} being clearly lower than V_{C1}.

Compared with the uncontrolled system shown in the appendix in figure A-3 the cur-

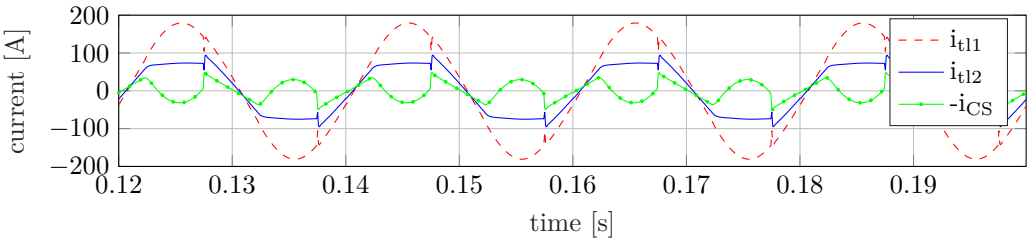

a) Currents on the transmission lines, and the negative control current.

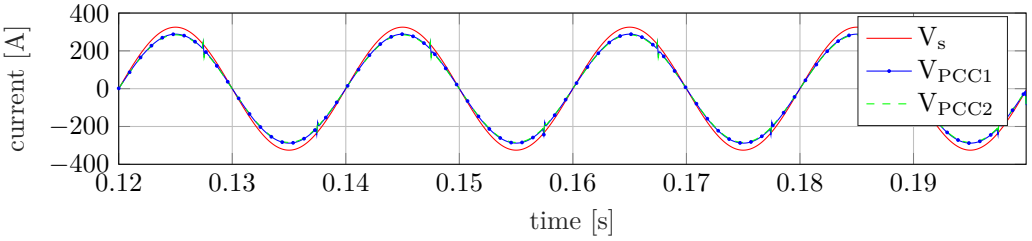

b) Supply voltage and voltages and the PCCs

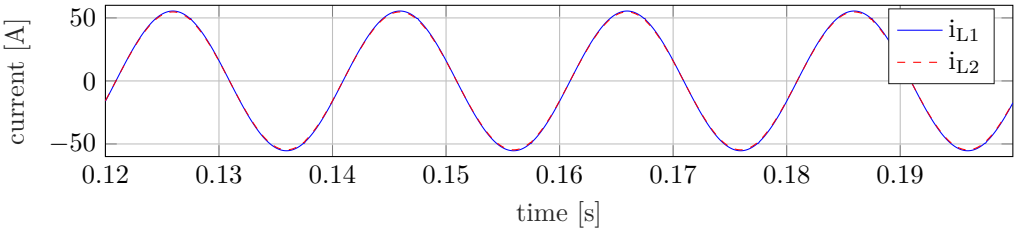

c) Currents over the linear loads.

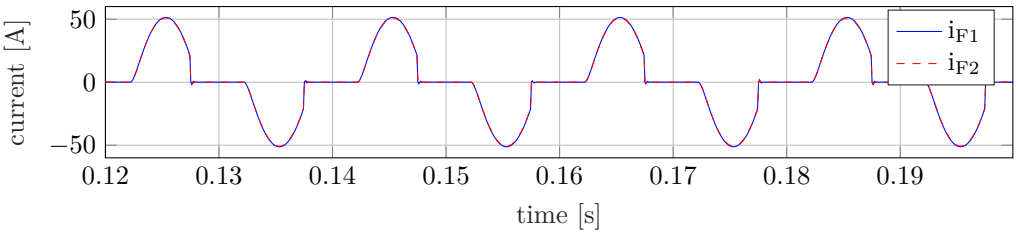

d) Currents over feeder line 1 and feeder line 2.

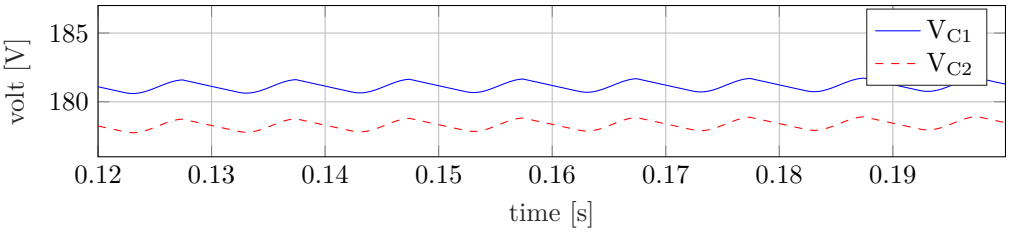

e) Voltages over the capacitors 1 and 2.

Figure 5-3: Controlled system Simulation results with set point 3 of the four mode switched system.

rent i_{tl1} displays a more sinusoidal form, while i_{tl2} is more distorted. Compared with SP1, shown in appendix figure A-4, the negative CS current $-i_{CS}$ is less extreme in its magnitudes, when only slightly. The set point SP2, shown in appendix figure A-5, provides only a minimal amount of negative CS current of opposite sign. This indicates higher load behavior/lower supply behavior.

5-2-2 Reanalyzing the Data

Of the eight set points, that were chosen for the stability analysis two were the same. Even though this set point (SP) did not proof to be stable after 500 periods, it is shown here, because it displays a different control strategy when compared to the other SPs. A constraint version of the model predictive control (MPC) controller should be capable of successfully utilizing this SP. A brief summary about the differences to SP3 is given below.

The summary of the simulation results of the additional stet point, set point extra (SPEx), is given in table 5-5. The decision variables of SPEx can be found in the annex in table A-1. The immediate difference is that the the apparent power supplied by the CS is considerably higher with 27821 VA, when compared to the other SPs. The current flowing on TL1 reduced to 72.95A, while the rms current on TL2 reduced to 18.30 A. The rms current of the CS increased to 71.8 A. Voltage levels at the PCCs increased by over 10 V, when compared to SP3. The power provided by the voltage supply decreased to 20551 VA. The power factor over TL1 improved to 0.9986, while the power factor of the CS is at 0.9494. Due to the higher voltage at the PCCs, current supplied to the linear loads and non–linear loads increased as well, when compared to SP3.

The SP is visualized in figure 5-4. The negative control current coincides with the currents of the distortions, acting mainly as a current supply. The minimum of $-i_{CS}$ reaches 128.1A in the first half period displayed. The voltages at the PCCs can be observed to be closer to the supply voltage in b). Also, the voltages over the capacitors V_{C1}, and V_{C2} show a still lasting increase in their magnitude.

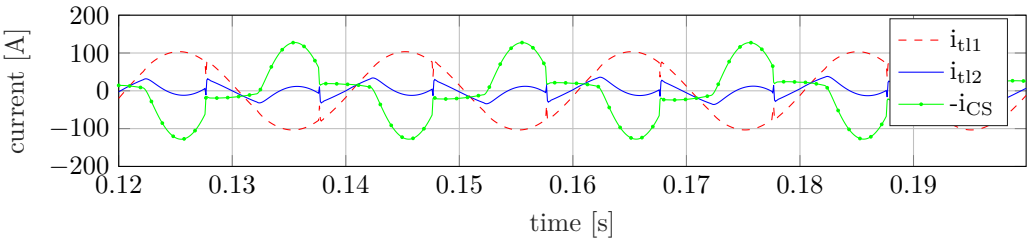

a) Currents on the transmission lines, and the negative control current.

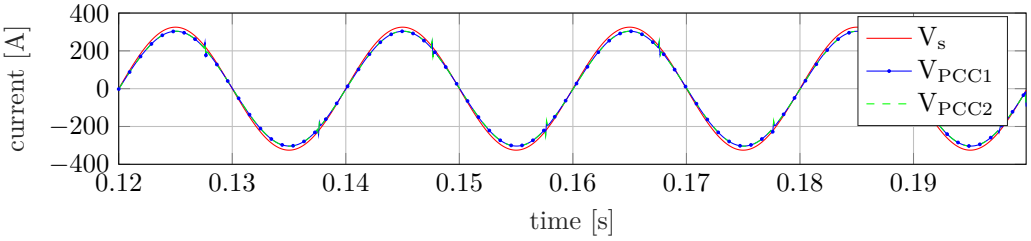

b) Supply voltage and voltages and the PCCs

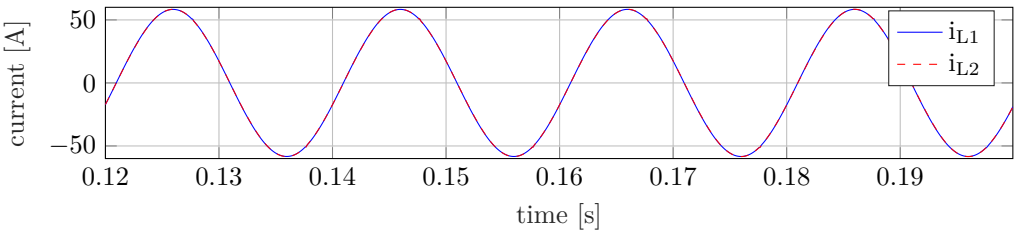

c) Currents over the linear loads.

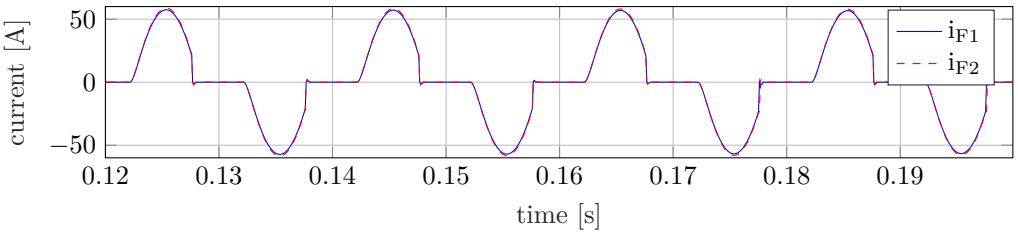

d) Currents over feeder line 1 and feeder line 2.

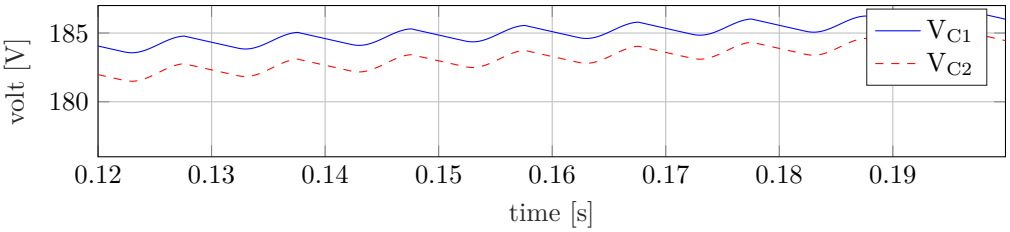

e) Voltages over the capacitors 1 and 2.

Figure 5-4: Controlled system Simulation results with set point 3 of the four mode switched system.

Table 5-5: Summary of the simulation results of the discarded set point SPEx.

Variable	RMS	THD [%]	Location	Variable	Value
V_s	230.0 V	0.7478	**TL1**	**S** [VA]	20551
V_{PCC1}	214.8 V	1.767		**Q** [VA]	1094
V_{PCC2}	214.5 V	1.886		**P** [W]	20522
V_{C1}	185.7 V	-		$\cos(\varphi)$	0.9986
V_{C1}	184.1 V	-		$\varphi[^\circ]$	-3.051
i_{tl1}	72.95 A	4.353	**CS**	**S** [VA]	27821
i_{tl2}	18.30 A	133.5		**Q** [VA]	8734
i_{L1}	41.27 A	0.6935		**P** [W]	26415
i_{L2}	41.22 A	0.8206		$\cos(\varphi)$	0.9494
i_{F1}	30.84 A	53.20		$\varphi[^\circ]$	-18.30
i_{F2}	31.47 A	52.99			
i_{CS}	71.68 A	44.93			

5-3 Analysis

The following analysis is split in three parts. The first subsection analyzes the level diagrams, followed by the discussion of the decision making process. The final subsection discusses the additional set point and its application for active power harmonics compensation.

5-3-1 Level Diagrams

The level diagrams contain information about the general working of the system, and the compensation. The difficulty in interpreting level diagrams is, that it is not clear, from which cost function an increase in the normalized distance originates, while a specifically regarded cost function changes it value. An additional problem arises from the controller it self. Since it is unconstrained, overcompensation of the system can easily occur. To extract information from the level diagrams, it is useful to first examine the overall structure, and then regard cost functions specifically from a plant and from a controller perspective.

An immediate observations is, that five of the six plots display a wedge like shape, where multiple solutions are found at very low normalized distances combined with low values in the considered cost on the x–axis. Only sub figure b) (best seen in appendix at figure A-1, and A-2) displays an inverse relationship, where comparatively high THDs actually lead to a decrease in the overall cost. This is an indication, that the sinusoidability of the current on TL2 is actually detrimental to the whole system,

with regards to overall cost. Additionally, the in depth analysis of the controlled system showed, that there is no evidence, that a bad THD on TL2 has a negative effect on the linear loads, or the THD on TL1. This indicates that the cost J_2 is not a good choice for the multiobjective optimization. Alternatives could have been the THD of the voltages at the PCCs, or the THD of the currents of the linear loads.

In order to eliminate most of the solutions, where an overcompensation of the MPC controller is present, the PF was pruned according to the limits specified in the results. The thresholds were kept comparatively high, to not accidentally eliminate valid design alternatives, because of the cross influence of the cost functions. Considering sub figure a) of the pruned level diagrams in figure 5-2, it can be seen from a system perspective, that exceptionally low values below 2 % in the THD of i_{tl1}, are only achieved with a considerable strain on the overall system. These strains can be, that the ACP needed by the CS is very high, but also, that the reactive power, or the rms of the current on TL1 is high. The origin of increase is unknown. However, considering that the normalized cost is calculated from all costs, it is impossible, that the highest values in the normalized distance result from an increase in only one of the cost functions. It can further be observed in a) that solutions above approximately 3 % THD are accompanied with increase in overall cost, which can be a sign of overcompensation by the unconstrained MPC controller.

This becomes more evident, when switching focus to sub figure c). A cluster of low normalized cost is found at around 5000 VA. The vertical increase in the normalized cost are most likely design alternatives of the controller, where the value of one cost function decreases somewhat, at the cost of most other cost functions of the system. However above 10000 VA the normalized cost and the ACP both increase at the same time. This is a sign, that the design alternatives of the controller lead to mostly overcompensation of the system. The normalized cost where that occurs is roughly at 1.4.

Regarding sub figure d), it can be observed, that solutions where the normalized cost rises above 1.4 are generally accompanied with values above approximately 5 in the reciprocal of the THD of i_{CS}. This indicates, that the controller tends to contribute a more and more sinusoidal signal to the system. As was pointed out, this is undesirable in so far, that the non–linear aspects of the distortions should be compensated by non–linear currents. As the CS current becomes more sinusoidal more reactive power is added to the system. Reactive power has to be provided by the voltage supply, but is not converted into useful work. Though reactive power is more tolerable than a high THD, it is also undesirable.

The increase of the normalized cost above 1.4 is observed to coincide somewhat with negative values for the reactive power factor shown in figure e). In power systems, a desirable value for the power factor is above $\cos(\varphi) = 0.90$. This power factor is the value where reactive current makes up 50 % of the active current provided. If the

power factor of a customer is below this threshold, usually additional payments have to be made, which regard the inductive reactive power that has to be provided by the grid[3]. For the reactive power factor, this means values above $\sin(\arccos(0.90)) = .4359$ are certainly undesirable. As can be seen in e) this coincides generally with a high normalized cost as well. Indicating a compensation style, that heavily increase reactive power in the system. This increase in reactive power is additionally reflected in f). The rms current on TL1 increases drastically with normalized cost above 1.4.

It can be concluded, when considering the combined level diagrams from c) to e), that most solutions in that high normalized cost range mainly lead to a THD compensation, which induce highly reactive load demands on the voltage supply. This is reflected in the high ACP, high reactive power factor and high current on TL1. A further indication is the high reciprocal of the THD of the CS current. There is one exception, which is the extreme point visible in b) with the highest THD on TL2 and lowest reactive power factor in sub figure e) and lowest current on TL1. This solution is actually the unstable point which was shown in figure 5-4 and will be discussed separately.

At this point, the examination of the level diagrams was stopped. To extract more information from the diagrams, more pruning needs to be applied to the individual cost functions and to the normalized cost. What was not examined were the level diagrams of the decision variables. The level diagram toolbox also allows to depict the relationship between the normalized cost, and the decision variables. It could be valuable to examine how the decision variables behave, and whether certain lines, that are visible in the cost functions reflect themselves in the decision variables. It is however thought, that this analysis would require considerably more time, which is why it was discarded from the scope of this thesis. The next part of the analysis covers the decision making process itself.

5-3-2 Decision Making Process

The original PF from the multiobjective optimization was reduced by a factor of about 0.2 from 476 to 96 solutions. The pruning mechanism applied disregarded solutions, which were above certain limits. This was done, to exclude solutions where the MPC controller clearly provides to much power to the system, either by being to sinusoidal in the input, having a too high ACP or leading to a stark increase in the currents on TL1. The only strong requirement is a THD of the current on TL1 below 5 %. The pruning was intentionally kept at relatively low requirements, as to not lose potentially valid solutions.

[3]An example for the prices of inductive reactive power can be found here [25]. These are prices published by the German grid provider “Netze Solingen GmbH”.

The next step was a stability analysis, with the six SPs that achieved the lowest value with respect to one cost function, and the lowest normalized cost of the original PF and the pruned PF. Only seven of the eight SPs were unique. Three stable solutions remained after the stability analysis. This shows two things

First of all, not all solutions which lead to a low cost function value are stable with the unconstrained LSSSMPC controller. This might maybe be circumvented with further cost functions in the multiobjective optimization. However it is not clear how these cost functions would influence the search process, as they could lead to an over restriction of spMODEx. The stability analysis required a lot more simulation time, and would have approximately doubled the time of the whole search process. This might not always be feasible.

The second thing is that the lowest normalized cost achieved by the original PF was actually unstable. This is an indication, that the pruning process was successful. To further study how useful the pruning process is, the lowest cost function value of the original PF should also be examined, and undergo a stability analysis, followed by an in depth analysis if proven to be stable. This is left as an open question for further study.

The three stable solutions were examined with an in depth analysis of the system. These were the points with the overall lowest normalized cost from the pruned PF (SP1), the solution with the lowest cost in the ACP (SP2), and the solution with the lowest value in the reciprocal of THD of i_{CS} (SP3). Two design general design alternatives can be observed.

The set points, SP1 and SP3 are similar in their effect on the system. They both compensate the system, by providing only some reactive power of about 1250 VA, and a bigger portion of active power around 4600 W. In both cases the apparent power that the voltage supply needs to transfer has decreased. For SP1 a decrease of 3.3 %, and for SP3 of 5.7 %, is observed. However the power factor on TL1 worsened for SP1, while it improves for SP3. The design alternative is given by SP2, which only requires low amount of active power from the CS, and provides almost exclusively reactive power to the system. This in turn forces the voltage supply to actually increase the current on TL1, which leads to an increase in the apparent power to 38933 VA. An increase of about 4.8 % in power demand.

For the choice a high level view is necessary. Considering that the compensation system is connected to a battery energy storage system (BESS), SP2 has two distinct disadvantages. The high reactive load component would require a continuous charging and discharging of the batteries. This will add a high strain on the BESS, as repeated charging and discharging generally leads to a higher rate of degradation in batteries. The second disadvantage is, that excesses amount of renewable energy, stored in the BESS basically goes unused. A similar compensation can also be achieved by an active

power filter, which compensates THD by taking active power from the gird, and re–injecting it at the appropriate points to compensate harmonics. As this device already exist, a advantage of the system proposed here would not be obvious. The advantage of the BESS is, that it can provide the compensation by using power that was generated before hand. Additionally, if compensation demand is present in the system, but BESS capacity is low, the controller could still use SP2 to bridge the gap, until the batteries are recharged.

This leaves SP1 and SP3 as the two remaining options. An examination of the overall system shows, that SP3 led to an overall better power supply in the whole system, while only needing 5.1 % more ACP then SP2. The rms voltage levels at the PCCs and currents to the linear loads are higher, then for SP1. This goes to the cost of a higher THD of the current on TL1, but is regarded as acceptable, as the level is still around 1.2 % lower then the allowed maximum of 5 %.

For these reasons SP3 is chosen as the final outcome of the decision making. The plot was shown in the result section of experiment one. The power supplying nature of SP3 can be observed, as the negative CS current becomes negative, when the non–linear load currents peak. SP3 still acts as a reactive load on the voltage supply. Drawing currents from the system, which coincide with the load current on TL1 at the beginning and end of every half period. The current on TL2 is highly distorted. This does however not lead to negative effects on the system, which makes sense. As long as the voltage levels at the PCCs are sinusoidal, the THD on TL2 itself is not of interest. This learning needs to be accounted in future research. Voltage levels at the capacitors of the distortions are also stable, and actually slightly higher, when compared to the uncontrolled system (UCS). All of this shows, that SP3 is not only capable of reducing THD, but also ensuring a better power supply for the overall system.

In conclusion, it can be said that the applied decision making process was successful, despite being fairly simple. Only a rough pruning of the initial solutions and a stability analysis were necessary, to reduce the total number of solutions to a manageable amount. The application of this strategy could be implemented fully automatic, up until the outcome of the stability analysis. The in depth analysis requires a better understanding of the problem at hand. Two distinct design alternatives in the compensation of the THD were identified. The choice of the correct set point need additional knowledge about the overall engineering problem.

A decision making process should never be applied blindly. The human assessment of the data should be involved. This is because valuable design alternatives overlooked, or design alternatives for future research might go unnoticed. This was the case with the last SP that was shown in section 5-2-2, and is briefly analyzed in the last subsection of the analysis.

5-3-3 Direct Active Power Supply of Non–Linear Distortions

As discussed in the analysis in the last subsection, a compensation strategy that mainly provides active power is desirable, because it takes advantage of the energy, that is stored in the BESS to compensate harmonics, instead of adding load demand to the system. A set point that achieves just that was found, when reanalyzing the eight/seven SPs that were the outcome after the pruning. The additional solution, named SPEx, did not prove to be stable. The problem observed (but not shown) was, that the CS increases its input with every period slightly, which finally leads to a compensation style, in which a sinusoidal load current is applied to compensate the system.

This issue could however be resolved in two ways. The first is to apply constrains to the MPC controller, which prevents the CS from applying higher and higher currents in each period. The second way is to repeat the multiobjective optimization, and start with an initial population that consist of multiple copies of the decision variables of SPEx. Combined with a low scaling factor of for example $F = 0.01$, the region around this set point could be explored further, hopefully leading to solutions with a similar control strategy.

The reason why this solution is so interesting is, that the non–linear currents are directly supplied by the CS, while only small amounts of reactive power is provided to the grid. This becomes evident, when looking at sub figure a) of figure 5-4, and also from examining table 5-5. The rms current of the CS is a bit more then twice the amount, of what is flowing on feeder line 1 (F1) and feeder line 2 (F2) to the non–linear distortions. It is somewhat higher, because the controller still adds some load behavior to the system. However it seems to satisfy all of the non–linear demand, which reduces the apparent power demand of the supply voltage to about 55 % of the uncontrolled system. The CS significantly increases the voltage level at the PCCs by more than 10 V, which in turn increases currents to the linear loads. The voltage drop at the PCCs is very high to begin with, due to a not ideal design of the resistance of TL1 (too big). It still shows, that the MPC controller is capable of supplying voltage stability as an additional electrical power quality (PQ) service and can drastically improve the power factor of the supply system.

Additionally, the power needed for this compensation would in reality probably be lower then what is shown here. This is because the non–linear loads as used here are an extreme case. Normally they would not be permitted to operate in a power system. The distortions would be required to have some form of compensation themselves, leading them to draw a current more sinusoidal, where the THD mostly results as a smaller jitter superimposed on the sin wave. This jitter is what would need be supplied by the CS, as opposed to the complete load current.

The finding presented can also be used as an additional lesson to the decision making process. Blindly following a set of rules might lead to a result, but will discard a lot of

valuable information along the way. The decision maker should always pay attention to what is discarded by the strategy itself, if an increase in knowledge is desired. This concludes the analysis of the second experiment with which the experimental part of this thesis is finished.

Chapter 6

Conclusion

In this chapter a conclusion of the results and analysis are given, and future research question are explored.

In this master thesis a controller tuning was implemented by multiobjective optimization, using the evolutionary algorithm Multiobjective Differential Evolution with Spherical Pruning X (spMODEx) for an unconstrained linear state signal shaping model predictive control (LSSSMPC) controller, to compensate total harmonic distortion (THD) in electrical distribution grids. Non–linear loads in electrical systems lead to what is known as THD. This thesis focused on two aspects in particular. The first aspect regarded the assessment of the reproducibility of the multiobjective optimization outcome, the Pareto Front (PF). The second aspect was the application of spMODEx to a realistic control scenario where plant and controller operated in mismatch. A decision making strategy was developed to chose an appropriate set point for the controller.

The assessment of the reproducibility of the PF was performed, to determine the trustworthiness of the algorithm when applied to a LSSSMPC controller. A grid model with two non–linear distortions, modeled by ideal current source, two linear loads, and two transmission lines was used as a basis for the simulations. The multiobjective algorithm used three cost functions in the evaluation of the solutions. A total number of 100 Pareto optimization was run with the system, which yielded an overall solution to compare the individual runs with.

It was shown, that a Pareto optimal solution from the individual runs had a likelihood of 78.21 % of still being Pareto optimal, when compared with the overall solution. The angle between the average direction vector (ADV)[1] of the individual solutions and the overall solution was determined to be on average $1.0011 \times 10^{-4\circ}$ with a standard deviation of 133.89 %. The low angle indicates that the solutions are practically identical. As a final assessment method, a novel method was introduced, the activated volume method (AVM).

The basic idea of the AVM is to encapsulate the points of the overall solutions with volumes in a normalized space, to attain a pixelated representation of the PF. The pixelated PF is then used to determine how many volumes of the representation are activated on average by an individual run. This depends on the grid size that is used for the pixelation. The grid size can be interpreted as an error margin with which an individual solution is allowed to deviate from the overall solution. For reasons given in the thesis, an error margin of 0.04, or 4 %, was found to be the best fit of the grid sizes tested. Under these condition an individual run covers on average 57.49 % with a standard deviation of 8.725 %, related to the mean, of the overall solution. This is possibly an underestimation, because extreme points of the overall solution were considered in the calculation as well. The extreme points however might not be part of the region of interest, as they usually display unacceptable values in one of the multiobjective cost functions.

[1] Sum of the eigenvectors scaled by the square of the singular values, acquired by means of singular value decomposition.

More research is needed, to gain a deeper understanding of the AVM and develop it further. The AVM could be useful, to assess performance of evolutionary algorithm (EA) in real world applications. The research should first focus on an in depth analysis of the appropriate grid size for the AVM. At a later development stage the AVM can be used in EAs, to automatically determine, when conversion of the solution has been reached. The overall outcome of the reproducibility assessment is that the spMODEx algorithm is indeed fit to be used with a LSSSMPC controller.

For the controller tuning application and decision making, the spMODEx algorithm was employed on an LSSSMPC controller operated in mismatch. The non linear distortions of the electrical system mentioned above were substituted by the linear state space representations of a rectifier. The electrical power system was thus simulated using a four mode switched system. A total number of six cost functions were used in the multiobjective optimization. The resulting PF was analyzed using level diagrams. To attain a stable set point for the controller, a decision making strategy was designed. In the first step, the number of solutions was reduced by pruning clearly unfeasible solutions, applying regulation and system knowledge. Next eight set points were chosen, of which three proved to be stable. The three set points were subjected to an in depth analysis of which one was finally chosen.

Multiple lessons could be derived. A relatively simple decision making process is capable of quickly identifying feasible and stable set points for the controller. The LSSSMPC controller is capable of compensating the harmonic distortions, by partly providing the non–linear distortions with active power, which has the advantage of supporting the grid provider with stored renewable energy, while simultaneously compensating THD, leading to an increase in the systems electrical power quality (PQ). Future research should examine, how many and what kind of cost functions can be used, to appropriately guide the multiobjective algorithm. As more cost functions lead to more information about the system, but can potentially prevent the multiobjective algorithm from fully exploring the complete solution space.

It was further shown, that the decision maker should critically assess the outcome of the decision making process, to prevent loss of valuable information. An additional controller set point was identified for future application, which was pruned during the decision making process. It was pruned because it was unstable after a longer simulation time. However, this set point was capable of directly providing the whole demand of the distortions for shorter simulations. Subsequently improving the overall supply of the system significantly, by positively influencing several PQ factors at once. Future research should focus on stabilizing the controller around this set point by utilizing more multiobjective optimization and by constraints, because of the benefits this operation mode can provides to the overall system.

Appendix A

Experiment 2 – Add on

A-1 Level Diagram of J_2 unpruned and pruned

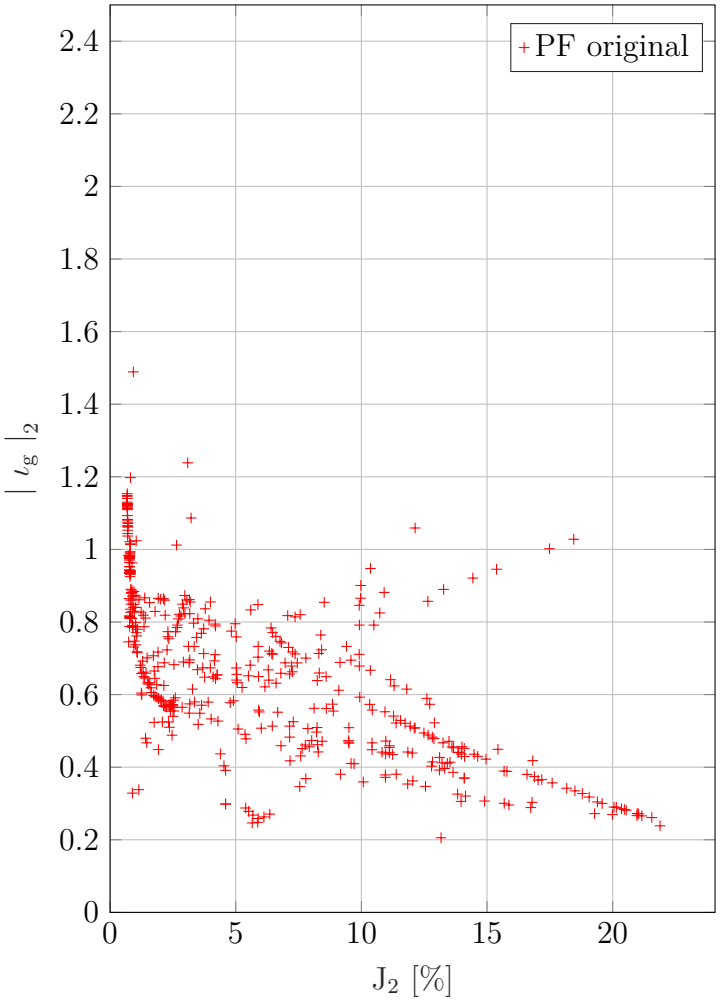

Figure A-1: Level Diagrams of the unpruned Pareto Front after the multiobjective optimization of the cost function $J_2 = \mathrm{THD}(i_{tl2}, 10)$ without the extreme point.

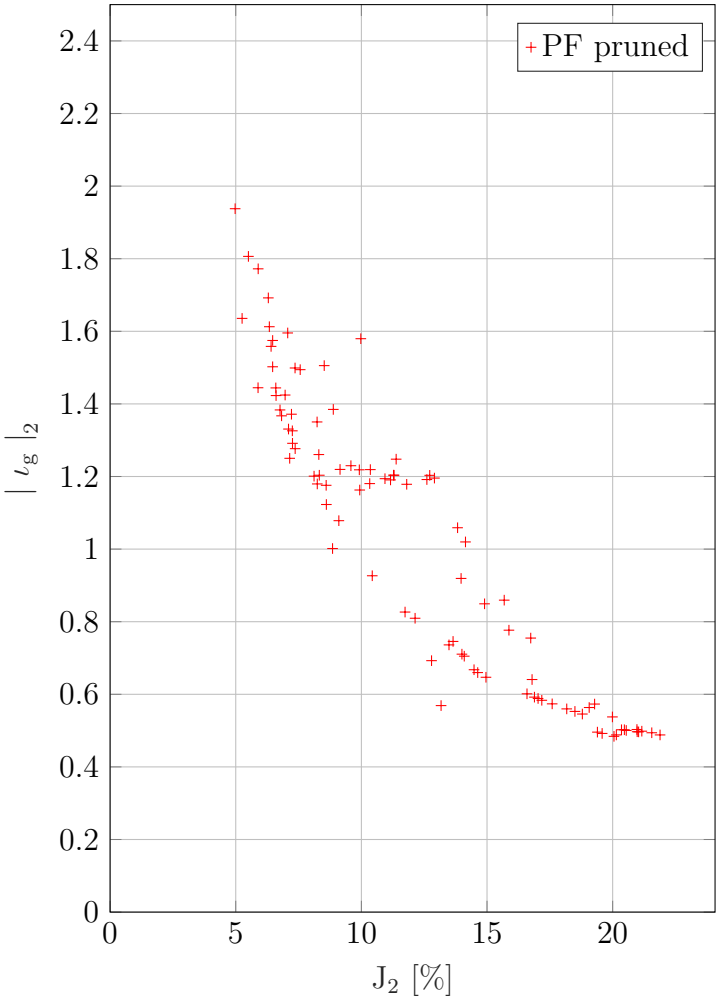

Figure A-2: Level Diagrams of the Pareto Front after the multiobjective optimization and pruning, showing the cost function $J_2 = \mathrm{THD}(i_{tl2}, 10)$ without the extreme point.

A-2 Simulation results - Uncontrolled System and Set Points

On the following pages, the voltages and currents of the simulation with the four mode switched system are shown for the uncontrolled system, as well as for set point 1 (SP1) and set point 2 (SP2).

Table A-1: Decision variables of the set points from experiment two.

	ζ_1	ζ_2	ζ_3	ζ_4
SP1	-2,03043034300876	-26,6716317734399	-19,8235694172961	-5,56442323516580
SP2	-5,09895770858944	-5,43232239871025	-25,3379281962735	-29
SP3	-6,58449170924069	-25,0816728948971	-6,23466067666424	-12,8653587638492
SPEx	24,3616845303662	11,4974183781967	-2,47249627408883	0,790605500734368

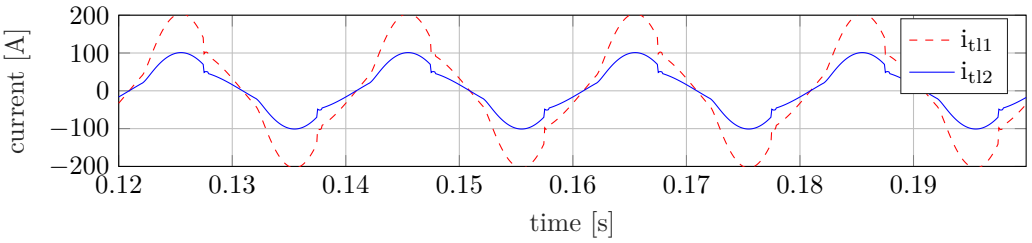

a) Currents on the transmission lines, and the negative control current.

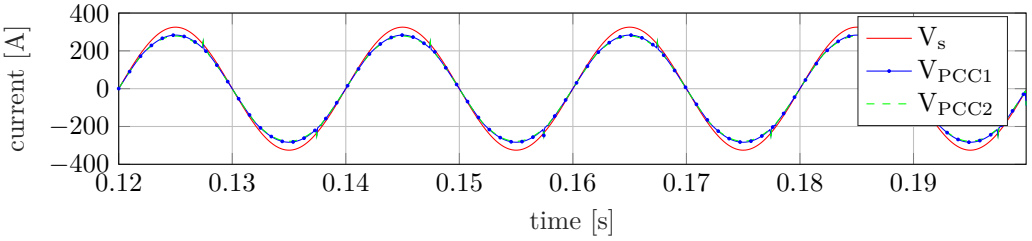

b) Supply voltage and voltages and the point of common couplings (PCCs)

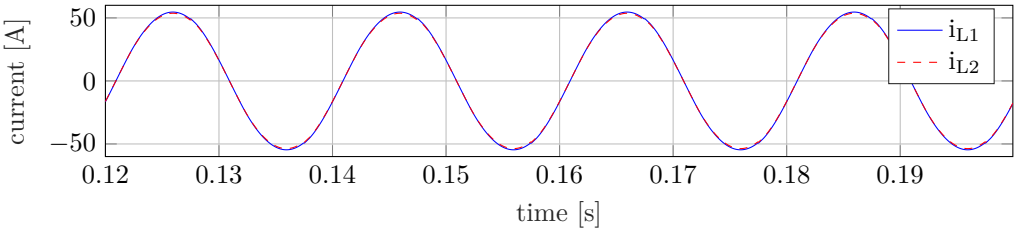

c) Currents over the linear loads.

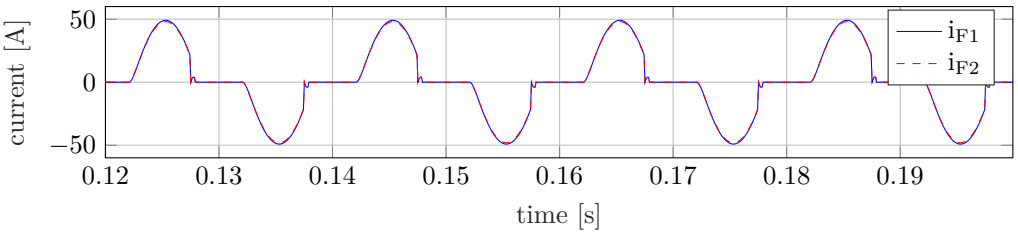

d) Currents over feeder line 1 and feeder line 2.

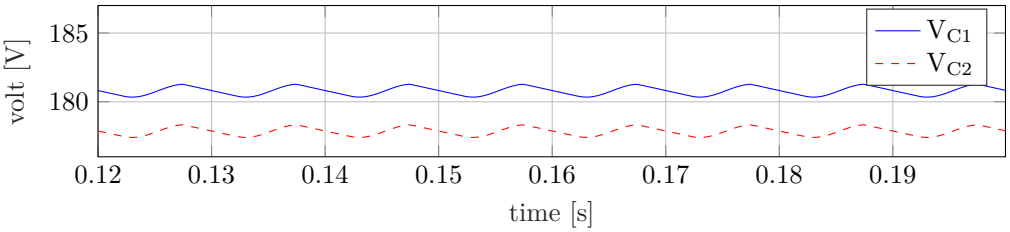

e) Voltages over the capacitors 1 and 2.

Figure A-3: Uncontrolled system Simulation of the four mode switched system.

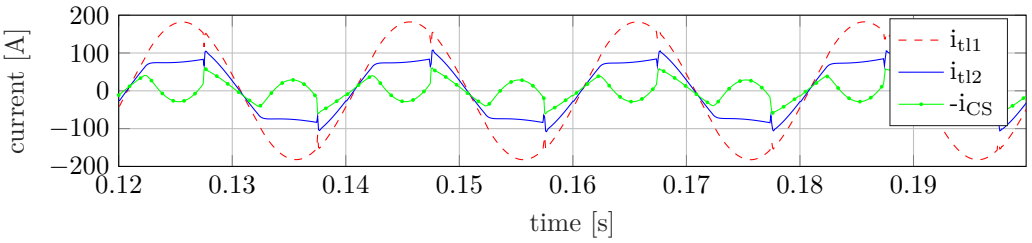

a) Currents on the transmission lines, and the negative control current.

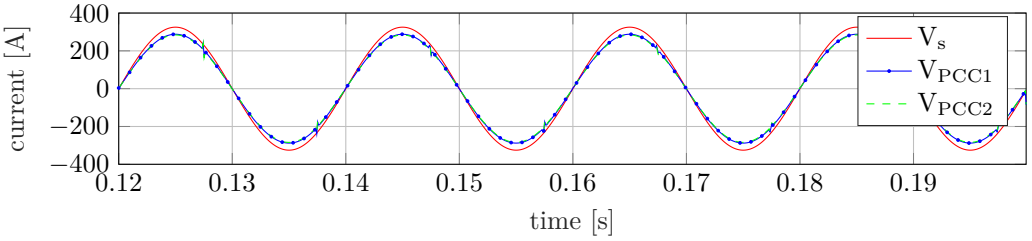

b) Supply voltage and voltages and the PCCs

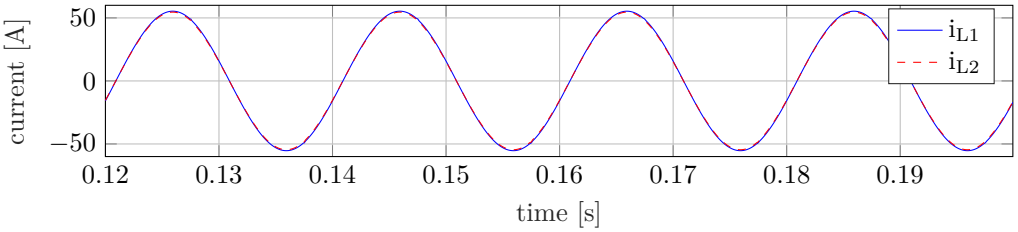

c) Currents over the linear loads.

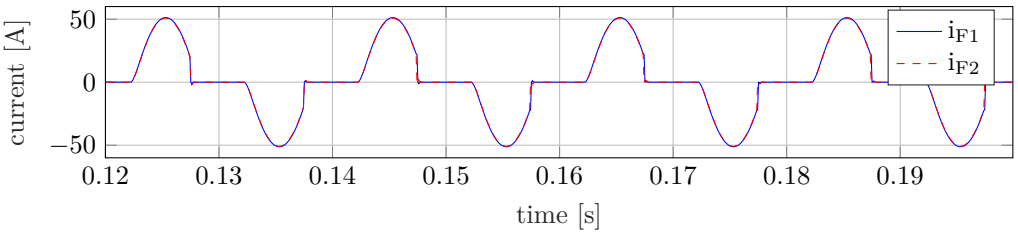

d) Currents over feeder line 1 and feeder line 2.

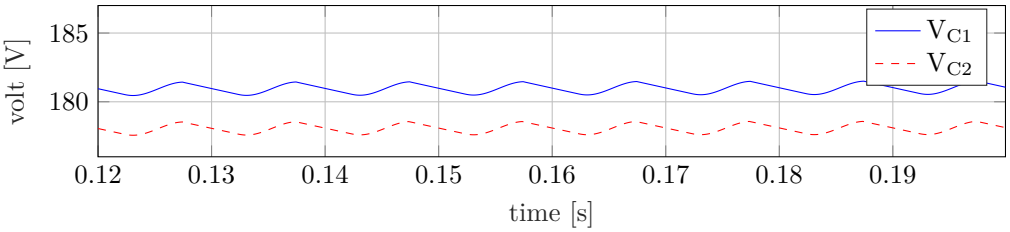

e) Voltages over the capacitors 1 and 2.

Figure A-4: Controlled system Simulation results with SP1 of the four mode switched system.

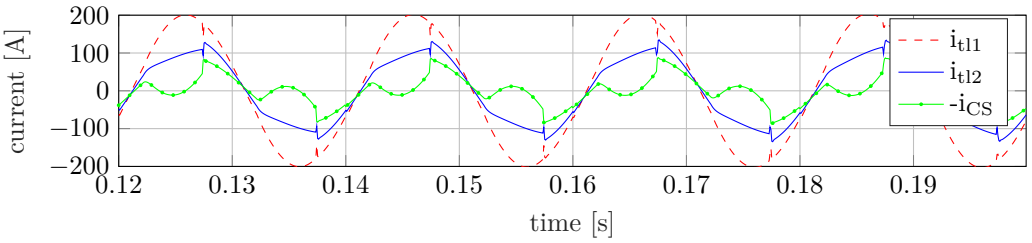

a) Currents on the transmission lines, and the negative control current.

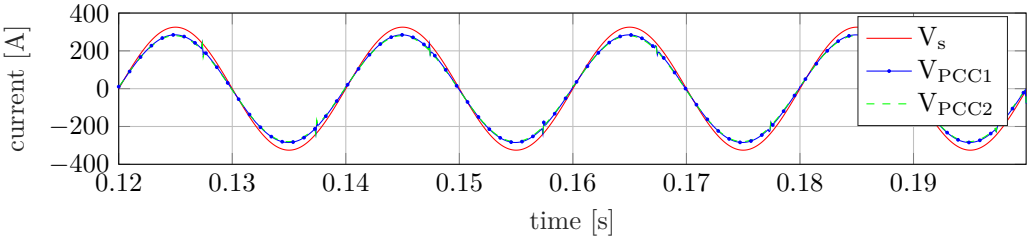

b) Supply voltage and voltages and the PCCs

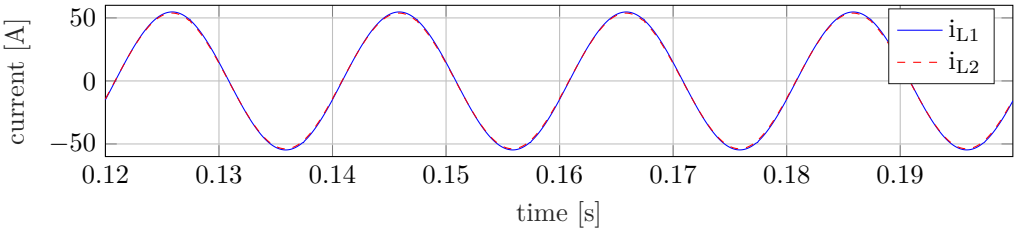

c) Currents over the linear loads.

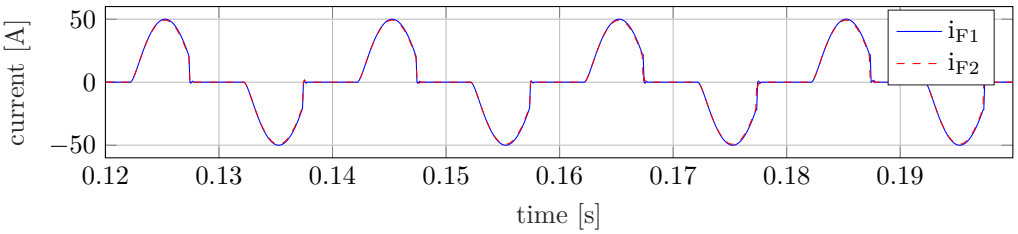

d) Currents over feeder line 1 and feeder line 2.

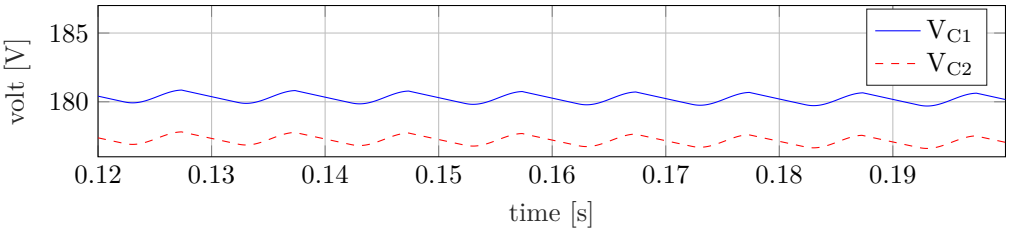

e) Voltages over the capacitors 1 and 2.

Figure A-5: Controlled system Simulation results with SP2 of the four mode switched system.

Bibliography

[1] K. Y. Lee and M. A. El-Sharkawi, *Modern Heuristic Optimization Techniques:Theory and Applications to Power Systems*. Hoboken, New Jersey, United States of America: Wiley-IEEE Press, 2008.

[2] G. R. Meza, X. B. Ferragud, J. S. Saez, and J. M. H. Durá, *Controller Tuning with Evolutionary Multiobjective Optimization: A Holistic Multiobjective Optimization Design Procedure*. Intelligent Systems, Control and Automation: Science and Engineering, Springer International Publishing, 2017.

[3] J. Capel and W. Beba, "NEW 4.0 Brosch\"ure (PDF) Englisch."

[4] B. Singh, A. Chandra, and K. Al-Haddad, eds., *Power Quality Problems and Mitigation Techniques*. Chichester, United Kingdom: John Wiley & Sons Ltd, Jan. 2015.

[5] J. M. Maciejowski, *Predictive Control: With Constraints*. Pearson Education, 2002.

[6] C. Cateriano Yáñez, G. Pangalos, and G. Lichtenberg, "An Approach to Linear State Signal Shaping by Quadratic Model Predictive Control," in *2018 European Control Conference (ECC)*, 2018, unpublished at the time.

[7] A. von Meier, *Electric Power Systems: A Conceptual Introduction* -. New Jersey, United States of America: Wiley-IEEE Press, 2006.

[8] "IEEE Recommended Practice and Requirements for Harmonic Control in Electric Power Systems," *IEEE Std 519-2014 (Revision of IEEE Std 519-1992)*, pp. 1–29, June 2014.

[9] E. F. Fuchs and M. A. S. Masoum, *Power Quality in Power Systems and Electrical Machines*. Amsterdam: Elsevier, 2015.

[10] D. Shmilovitz, "On the definition of total harmonic distortion and its effect on measurement interpretation," *IEEE Transactions on Power Delivery*, vol. 20, pp. 526–528, Jan. 2005.

[11] K. J. Åström and R. M. Murray, *Feedback Systems*. 2008.

[12] G. Lichtenberg, "Advanced Control Systems - Interactive Lecture.".

[13] K. J. Åström and B. Wittenmark, *Computer-Controlled Systems: Theory and Design, Third Edition*. Courier Corporation, June 2013.

[14] C. Cateriano Yáñez, *Model Predictive Ideal Harmonic and Reactive Power Compensation for Fixed Frequency in Distribution Grids*. Master Thesis, HAW Hamburg, Hamurg, Germany, Apr. 2017.

[15] L. I. Burke and J. P. Ignizio, "Neural networks and operations research: An overview," *Computers & Operations Research*, vol. 19, pp. 179–189, Apr. 1992.

[16] G. Reynoso Meza, *Controller Tuning by Means of Evolutionary Multiobjective Optimization: a Holistic Multiobjective Optimization Design Procedure*. Tesis doctoral, Editorial Universitat Politècnica de València, June 2014.

[17] X. Blasco, J. M. Herrero, J. Sanchis, and M. Martínez, "A new graphical visualization of n-dimensional Pareto front for decision-making in multiobjective optimization," *Information Sciences*, vol. 178, pp. 3908–3924, Oct. 2008.

[18] D. Jouan-Rimbaud, D. L. Massart, C. A. Saby, and C. Puel, "Determination of the representativity between two multidimensional data sets by a comparison of their structure," *Chemometrics and Intelligent Laboratory Systems*, vol. 40, pp. 129–144, June 1998.

[19] G. Reynoso-Meza, J. Sanchis, X. Blasco, and M. Martínez, "Design of Continuous Controllers Using a Multiobjective Differential Evolution Algorithm with Spherical Pruning," in *Applications of Evolutionary Computation* (C. Di Chio, S. Cagnoni, C. Cotta, M. Ebner, A. Ekárt, A. I. Esparcia-Alcazar, C.-K. Goh, J. J. Merelo, F. Neri, M. Preuß, J. Togelius, and G. N. Yannakakis, eds.), pp. 532–541, Springer Berlin Heidelberg, 2010.

[20] R. Storn and K. Price, "Differential Evolution – A Simple and Efficient Heuristic for global Optimization over Continuous Spaces," *Journal of Global Optimization*, vol. 11, pp. 341–359, Dec. 1997.

[21] A. Messac, “Physical programming - Effective optimization for computational design | AIAA Journal,” vol. Vol. 34, no. No. 1, pp. 149–158.

[22] S. Das and P. N. Suganthan, “Differential Evolution: A Survey of the State-of-the-Art,” *IEEE Transactions on Evolutionary Computation*, vol. 15, pp. 4–31, Feb. 2011.

[23] G. Reynoso-Meza, J. Sanchis, X. Blasco, and J. M. Herrero, “Hybrid DE algorithm with adaptive crossover operator for solving real-world numerical optimization problems,” in *2011 IEEE Congress of Evolutionary Computation (CEC)*, pp. 1551–1556, June 2011.

[24] B. J. Baliga, *The IGBT Device: Physics, Design and Applications of the Insulated Gate Bipolar Transistor*. William Andrew, Mar. 2015.

[25] “Entgelte Netznutzung Strom - SWS Netze Solingen GmbH.” http://www.netze-solingen.de/544.html.

Glossary

List of Acronyms

LTI linear time-invariant system

THD total harmonic distortion

rms root mean square

MPC model predictive control

LSSSMPC linear state signal shaping model predictive control

MOA multiobjective algorithm

MOP multiobjective problem

AOF aggregate objective function

GFCL generate first choose later

DM decision maker

EA evolutionary algorithm

spMODEx Multiobjective Differential Evolution with Spherical Pruning X

spMODE-II Multiobjective Differential Evolution with Spherical Pruning-II

spMODE Multiobjective Differential Evolution with Spherical Pruning

DE Differential Evolution

ADV	average direction vector
ACP	Apparent Control Power
APF	active power filter
AVM	activated volume method
IGBT	insulated-gate bipolar transistor
PCC1	point of common coupling 1
PCC2	point of common coupling 2
PQ	electrical power quality
PF	Pareto Front
PCC	point of common coupling
TL1	transmission line 1
TL2	transmission line 2
L1	linear load 1
L2	linear load 2
F1	feeder line 1
F2	feeder line 2
D1	distortion 1
D2	distortion 2
CS	compensation source
SP1	set point 1
SP2	set point 2
SP3	set point 3
UCS	uncontrolled system
SPEx	set point extra

SP	set point
DC	direct current
AC	alternating current
BESS	battery energy storage system

Index